



SAPIENZA
UNIVERSITÀ DI ROMA

Neural Network based Steering and Hardware in Loop Simulation of Variable Speed Control Moment Gyroscope

Dipartimento di Ingegneria Meccanica e Aerospaziale (DIMA)
Corso di Laurea Magistrale in Space and Astronautical Engineering (LM-20)

Candidate

Siddharth Nimbajirao Deore
ID number 1823670

Thesis Advisor

Prof. Fabio Santoni

Academic Year 2019-20

Thesis defended on 26th January 2021
in front of a Board of Examiners composed by:

Prof. Mauro Valorani (chairman)
Prof. Francesco Creta
Prof. Giuliano Coppotelli
Prof. Pasquale Tommasino
Prof. Nazzareno Pierdicca
Prof. Daniele Bianchi

Neural Network based Steering and Hardware in Loop Simulation of Variable Speed Control Moment Gyroscope

Master's thesis. Sapienza – University of Rome

© 2020 Siddharth Nimbajirao Deore. All rights reserved

This thesis has been typeset by L^AT_EX and the Sapthesis class.

Version: September 26, 2023

Website: <http://deore.in>

Author's email: deore.1823670@studenti.uniroma1.it

Dedicated to mother Usha and father N. Z. Deore

Abstract

Control Moment Gyroscope (CMG) an attitude control actuator, generates torques utilizing gyroscopic couple by tilting spin axis of high angular momentum wheels. Despite having significantly large torque compared to Reaction Wheels, they pose the problem of singularity. Significant efforts had been made to surmount singularity problem associated with CMG. Variable Speed Control Moment Gyroscope (VSCMG) can avoid singularities by changing flywheel speed to escape singular states. Various singularity avoidance techniques have been proposed such as Singularity Robust Pseudo inverse, and Local Gradient method both are computationally complex and requires fine tuning of weights in steering logic.

Neural Network based VSCMG attitude control is discussed in this thesis. Neural Networks can approximate any nonlinear function with high accuracy. Nonlinear Dynamics of generic VSCMG and Singularity Robust steering law is realized. Supervised Learning is used to pretrain a deep neural network with trajectories generated from Monte-Carlo simulation of SR-VSCMG steering law. Pre trained neural network is further trained using Proximal Policy Optimization a policy gradient method for Reinforcement Learning in which intelligent agent interacts with environment by taking action based on current state. For each action there is a reward associated based on pre-determined reward function, goal is to maximize the delayed reward. PPO utilizes multiple epochs of minibatch updates instead of one gradient update per sample, this is advantageous since network parameters does not change rapidly consequently complex nonlinear behavior of VSCMG steering is easily approximated. Performance of Neural Network based steering is compared with SR-VSCMG steering via numerical simulations. Results show that trained Neural Network based steering agent is found to be computationally less expensive and showed significant improvement in computation time over conventional control methods, moreover it is capable of escaping singularities and avoid singular states in large slew maneuver. In proximity of singularity, very high frequency jitters of gimbal angles clearly seen in SR-VSCMG steering law may compromise structural integrity of satellite, proposed technique is inverse free and does not subjected to such high frequency jitters hence clearly advantageous safeguarding structural integrity.

For performance verification of numerical simulations on physical system a low-cost testbed for hardware in loop simulation of Variable Speed Control Moment Gyroscope (VSCMG) is developed. Reconfigurable Attitude Control System test setup comprise of a platform with pyramid cluster of SGCMG units balancing on sharp tip with its center of mass kept close to point of contact to simulate complete rotational freedom in yaw, constrained roll and pitch while restricting translation motion. High bandwidth communication between customized developed ground station software and test bed on-board computers allows just in time updates of controller parameters, real-time visualization of sensor state and switching between various control schemes.

Keywords : VSCMG, Neural Network, Reinforcement Learning, Spacecraft Test Bench , Hardware in Loop Simulation

Acknowledgments

I would like to express deepest sense of gratitude to my thesis advisor Prof. Fabio Santoni for introducing me to complex challenging subject and encouraging me to develop experimental setup to gain practical insights satellite system to bridge gap between theoretical understanding and practical implementation. It was great privilege and honor to work and explore under his guidance.

Furthermore, I would like to thank my friend Graziano Ullucci for helping me in various stages to build the prototype and providing manufacturing support for various parts of the project. In addition a special thanks goes to Centro Saperi Co for permitting me to 3D print few parts amidst global pandemic restriction.

Finally, I am extremely grateful to my parents and sisters for their love and support throughout my academic trial.

Table of Contents

Abstract	iii
Acknowledgments	iv
List of Tables	viii
List of Figures	ix
List of Acronyms	xiv
Glossary	xv
Nomenclature	xviii
1 Introduction	1
1.1 Motivation	1
1.2 Literature Survey	2
1.3 Thesis Outline	5
2 Equation(s) of Motion	6
2.1 Frame of reference	6
2.1.1 Rotation Matrix	6
2.1.2 Euler Axis angle	7
2.1.3 Davenport chained rotations	7
2.1.4 Quaternions	8
2.2 Kinematics	10
2.3 Dynamics	12
2.3.1 System Representation	13
2.3.2 Control Moment Gyro Model	13
2.4 Spacecraft Attitude Dynamics	16
2.4.1 Reaction Wheel (RW)	18
2.4.2 Control Moment Gyroscope (CMG)	19
2.4.3 Variable Speed Control Moment Gyroscope (VSCMG)	20
3 Singularity	23

4 Controller Design	27
4.1 Lyapunov Stability Method	27
4.2 Model based Controller Design	28
4.2.1 The Lyapunov Candidate Function	29
4.2.2 Stability Analysis	30
4.3 Steering Law	32
4.3.1 Reaction Wheel Optimization	33
4.3.2 Acceleration-Based Gimbal Tracking	35
4.3.3 Velocity Based VSCMGs Steering Law	36
5 Numerical Simulations	39
5.1 A priory dimensions	39
5.2 RW based ACS	39
5.2.1 Rest to rest reorientation with RW only	40
5.2.2 Regulation maneuver with RW only ACS	42
5.3 CMG based ACS	43
5.3.1 Rest to rest reorientation with CMG only ACS	44
5.3.2 Body rate regulation with CMG only ACS	46
5.4 VSCMG based ACS	49
5.5 Body rate regulation with VSCMG	50
5.6 Trajectory tracking with VSCMG ACS	52
6 Neural Network based Learning Agent	55
6.1 Machine Learning	55
6.1.1 Supervised Learning	55
6.1.2 Unsupervised Learning	56
6.1.3 Reinforcement Learning	56
6.2 Policy Gradient Methods	59
6.2.1 Policy Gradient Theorem	59
6.2.2 Proximal Policy Optimization (PPO)	60
6.3 Neural Network	61
6.3.1 Multi Layer Perceptron policy	62
6.4 Neural Network based VSCMG steering Law	64
6.4.1 Reinforcement Learning Agent	64
6.4.2 Training Procedure	64
6.4.3 Observation Space	65
6.4.4 Action Space	65
6.4.5 Reward Function	65
6.5 Training	66
6.5.1 Test Results	67
6.6 Comparison of Neural Network and SR-VSCMG Steering Law	71
7 Mechanical Design	76
7.1 System Overview	76
7.2 Reaction Wheel Motor	77
7.3 Gimbal Motor	77
7.4 Slip Ring	77

7.5	SGCMG Assembly Design	78
7.5.1	Gimbal Motor Mount	78
7.5.2	Reaction Wheel Mount	79
7.6	Base Platform	79
8	Embedded System Architecture	84
8.1	Platform Master State Feedback System	84
8.1.1	Microcontroller	84
8.1.2	IMU	85
8.2	Close Loop SGCMG	85
8.3	Electrical Power System	87
8.4	Ground Control Station Server	89
8.4.1	Communication	90
9	Hardware in Loop Simulations	95
9.1	Free Motion (ACS off)	95
9.2	Open Loop Control	95
9.2.1	Open Loop CMG	95
9.3	Close Loop SR-VSCMG Control	97
10	Conclusion	101
	Bibliography	102

List of Tables

2.1	Explanation of individual terms in generalize equation of motion for satellite with generic number of VSCMG	19
5.1	Preliminary system configuration and dimensions	39
5.2	Initial and desired states with yaw error of 60 deg	40
5.3	Initial and desired states for attitude error $\phi = 30^\circ, \theta = 60^\circ, \psi = 90^\circ$	44
5.4	Initial and desired states for angular velocity error with CMG in singular configuration	46
5.5	MOLNIYA 1-86 Orbital details	52
6.1	Commonly used activation functions and their derivative	62
6.2	PPO Algorithm Hyper-parameter configuration	67
6.3	Initial and desired states for Attitude error tracking with Neural Network based VSCMG steering Law	68
6.4	Simulation parameters for regulation maneuver in order to cancel attitude error of 90° in yaw angle.	71
8.1	Telemetry packet from SGCMG to Server	91
8.2	Composition of Leftmost and rightmost byte of 16 bit word.	92
8.3	Command packet from Server to SGCMG MCU	92
8.4	Telemetry packet from Master MCU to Server	93

List of Figures

1.1	NanoAvionics (4RW0) integral four - reaction wheels redundant 3-axis control system	2
2.1	Representation of Rigid body rotation in space	12
2.2	Schematic illustration of Spacecraft with Momentum exchange device	13
2.3	Axis definition for generic Control Moment Gyroscope	14
2.4	VSCMG Pyramid Cluster initial orientation	21
3.1	Vector representation at singular gimbal state	24
3.2	Singular surface of control moment gyro in pyramid configuration with skew angle $\beta = 54.73^\circ$	26
4.1	VSCMG Spacecraft Attitude Control Architecture	27
5.1	Quaternions for RW only rest to rest maneuver	40
5.2	Euler angles for RW only rest to rest maneuver	40
5.3	Body rates for RW only rest to rest maneuver	41
5.4	RW velocity for RW only rest to rest maneuver	41
5.5	RW accelerations for RW only rest to rest maneuver	41
5.6	Quaternions for RW only station keeping maneuver	42
5.7	Euler angles for RW only station keeping maneuver	42
5.8	Body rates for RW only station keeping maneuver	43
5.9	RW velocity for RW only station keeping maneuver	43
5.10	RW accelerations for RW only station keeping maneuver	43
5.11	Quaternions for CMG only reorientation with attitude error $[\phi \theta \psi] = [30, 60, 90]^\circ$	44
5.12	Euler angles for CMG only reorientation with attitude error $[\phi \theta \psi] = [30, 60, 90]^\circ$	45
5.13	Body rates for CMG only reorientation with attitude error $[\phi \theta \psi] = [30, 60, 90]^\circ$	45
5.14	Gimbal angles for CMG only reorientation with attitude error $[\phi \theta \psi] = [30, 60, 90]^\circ$	45
5.15	Gimbal rates for CMG only reorientation with attitude error $[\phi \theta \psi] = [30, 60, 90]^\circ$	46
5.16	Gimbal rates for CMG only reorientation with attitude error $[\phi \theta \psi] = [30, 60, 90]^\circ$	46
5.17	Quaternions for station keeping with CMG only ACS	47

5.18	Body Rates for station keeping with CMG only ACS	48
5.19	Euler angles for station keeping with CMG only ACS	48
5.20	Gimbal angles for station keeping with CMG only ACS	48
5.21	Gimbal velocities for station keeping with CMG only ACS	49
5.22	Zoomed view of station keeping maneuver with CMG only ACS	49
5.23	Euler angles for station keeping with VSCMG in vicinity of singularity	50
5.24	Body rates for station keeping with VSCMG in vicinity of singularity	50
5.25	RW rates for station keeping with VSCMG in vicinity of singularity	51
5.26	RW accelerations for station keeping with VSCMG in vicinity of singularity	51
5.27	Gimbal angles for station keeping with VSCMG in vicinity of singularity	51
5.28	Gimbal velocities for station keeping with VSCMG in vicinity of singularity	52
5.29	Reference trajectory quaternions computed for MOLNIYA 1-86	53
5.30	Least square residuals of quaternions computed for MOLNIYA 1-86	53
5.31	Euler angles computed for MOLNIYA 1-86	53
5.32	Body rates for trajectory tracking maneuver	54
5.33	RW angular velocity for trajectory tracking maneuver	54
6.1	Machine Learning Classifications	56
6.2	The agent-environment interaction in interaction in a Markov Decision Process. [1]	57
6.3	Surrogate $J^{CLIP}(\theta)$ as function of probability ratio for positive (left) and negative (right) advantage, figure reconstructed from original paper. [2]	60
6.4	Components of individual Neuron.The activation function is denoted by f and applied on the weighted sum of inputs with added bias	61
6.5	Commonly used activation functions	62
6.6	Multi Layer Perceptron	63
6.7	Neural Network based VSCMG Spacecraft Steering and Control Architecture	64
6.8	Flowchart of actor critic based PPO learning model [3]	66
6.9	Averaged episode reward for 16000 episodes of PPO training	67
6.10	NN based steering: Required torques	68
6.11	NN based steering: Gimbal angles	69
6.12	NN based steering: RW velocities	69
6.13	NN based steering: Gimbal Velocities	70
6.14	NN based steering: RW Accerlations	70
6.15	VSCMG Model and expert agent Testing GUI	71
6.16	Attitude quaternions : (a) Neural Network based steering (b) SR-VSCMG steering	72
6.17	Body rates (rad/sec): (a) Neural Network based steering (b) SR-VSCMG steering	72
6.18	Reaction wheel angular velocity : (a) Neural Network based steering (b) SR-VSCMG steering	73
6.19	Gimbal Angle : (a) Neural Network based steering (b) SR-VSCMG steering	73

6.20	System approaches singular state as singularity measure tends to zero (a) CMG singularity; (b) Reaction Wheel singularity and (c) VSCMG singularity	74
6.21	CMG gimbal angles : (a) Neural Network based steering (b) SR- VSCMG steering	74
7.1	VSCMG Attitude Control System test bed Assembly	76
7.2	VSCMG Attitude Control System placed over tripod with sharp tip being only point of contact	77
7.3	Three phase, outrunner, Brushless DC Motor as reaction wheel . . .	78
7.4	Stepper motor [4]	79
7.5	6 channel Slip Ring	80
7.6	Gimbal Motor Mount	80
7.7	Reaction Wheel Motor Mount	81
7.8	assembled SGCMG unit	81
7.9	SGCMG assembly exploded view	82
7.10	Sharp tip mounting assembly employed to minimize rotational friction with 360 degree rotational freedom in yaw axis and ± 60 deg allowed rotation in roll and pitch axis	82
7.11	Complete VSCMG testbed Assembly Rendered view	83
8.1	IMU interface board customized for BNO055 and ESP32.	85
8.2	BNO055 Absolute orientation sensor consist of triaxial accelerometer, triaxial gyroscope and triaxial magnetometer with on-board 32bit MCU running sensor fusion algorithm	86
8.3	20 A Sensorless Electronic Speed Controller	86
8.4	Polulu DRV8825 stepper motor driver shield	87
8.5	AS5600 magnetic encoder with radially magnetized magnet of 5mm diameter	87
8.6	Schematic diagram of Close loop SGCMG electronics and wiring . .	88
8.7	Schematic diagram of 11.1V 5A Battery Management System with 18650 Li-Ion batteries in series	88
8.8	Rendered view of Case with three Li-Ion Batteries connected in series to make 3S Li-Ion battery pack	89
8.9	MP1584EN 3A DC to DC step down converter configured to convert 11.1V to 5.0V	89
8.10	Wiring schematic of complete VSCMG test bed Electrical Power System	90
8.11	Ground command and control server Graphical User Interface . . .	94
9.1	ACS off free motion of test bed upon disturbance	96
9.2	Free response of platform subjected to disturbance, Euler angles (deg)	96
9.3	Open loop maneuver results of CMG	97
9.4	Close loop maneuver using VSCMG steering law with only derivative feedback - Platform quaternions	97
9.5	Close loop maneuver using VSCMG steering law with only derivative feedback - Platform angular velocities (rad/sec)	98

9.6	Close loop maneuver using VSCMG steering law with only derivative feedback - Euler angles (deg)	98
9.7	Top view of custom-built VSCMG experimental test bed and tripod	99
9.8	Top view of custom-built VSCMG experimental test bed balancing on tripod	100
9.9	Side view of custom-built VSCMG experimental test bed balancing on tripod	100

List of Acronyms

ACS Attitude Control System. 2, 3, 44, 49, 89

BLDC Brushless DC. 77, 79

CMG Control Moment Gyroscope. 1, 44

CRC Cyclic Redundancy Check. 91, 92

DLL Dynamical Linked Library. 65

HEO Highly Elliptical Orbit. 52

IPACS Integrated Power Attitude Control System. 3, 4

LADEE Lunar Atmosphere and Dust Environment Explorer. 2

MCU Microcontroller Unit. 85, 87, 89, 90

MDP Markov Decision Processes. 56–58

ML Machine Learning. 66

MLP Multi Layer Perceptron. 62, 64

NN Neural Network. 101

ODE Ordinary Differential Equation. 65

PCB Printed Circuit Board. 85

RL Reinforcement Learning. 29

RW Reaction Wheel. 2

RW Reaction Wheel. 2, 4, 44

SCL Serial Clock. 85

SDA Serial Data. 85

- SGCMG** Single Gimble Control Moment Gyroscope. 76, 78, 87
- SR-VSCMG** Singularity-Robust VSCMG Steering Law. 71, 72
- SVD** Singular Value Decomposition. 34, 37
- UDP** User Datagram Protocol. 90
- VSCMG** Variable Speed Control Moment Gyroscope. 1, 5, 49, 89

Glossary

Action The mechanism by which the agent transitions between states of the environment.. 56

Advantage A measure of how much is a certain action a good or bad decision given a certain state. 58

Agent The entity (robot) that uses a policy to maximize expected return gained from transitioning between states of the environment.. 57

Environment System dynamical model that agent can interact with.The environment changes as the Agent performs actions; every such change is considered a state-transition.. 57

Episode Finite sequence of state action pair till predefined terminal time-steps. 58

Policy An agent's probabilistic mapping from states to actions.. 57

Reward The numerical result of taking an action in a state, as defined by the environment.. 56

State The parameter values that describe the current configuration of the environment.. 57

Value A function which describes or approximates the expected discounted return from each state under a particular policy.. 58

Nomenclature

Spacecraft Attitude Dynamics

\mathcal{F}_i	Inertial reference frame
\mathcal{F}_b	Body fixed reference frame
\mathcal{F}_g	Gimbal Reference frame
R	Rotation matrix
q	Quaternion
q_i	Components of Quaternion $i \in \{0, 1, 2, 3\}$
ϕ	Roll
ψ	Yaw
θ	Pitch
q_v	vector component of quaternion
qd	Desired attitude quaternion
qe	Attitude error quaternion
ω	Angular velocity vector
\mathcal{T}	Kinetic Energy
\mathcal{H}	Angular momentum
\mathcal{H}_P	Angular momentum of platform
\mathcal{H}_{CMG}	Angular momentum of CMG system
\mathcal{H}_W	Angular momentum of Reaction wheel
\mathcal{H}_u	Angular momentum component along singular direction
τ_e	Environmental Torques
τ_d	Disturbance Torques
u	Control Torque

J_p	Platform inertia tensor
J_W	Reaction Wheel inertia
J_G	Gimbal inertia
J_{CMG}	CMG inertia tensor; wheel and gimbal combined
$\hat{\mathbf{g}}$	Gimbal Axis
$\hat{\mathbf{s}}$	Spin Axis
$\hat{\mathbf{t}}$	Transverse Axis
Ω	Reaction Wheel angular velocity
δ	Gimbal angle
β	VSCMG pyramid skew angle

AI based Learning Agent

$s \in \mathcal{S}$	States
$a \in \mathcal{A}$	Actions
$r \in \mathcal{R}$	Rewards
γ	Discount factor $0 < \gamma \leq 1$
G_t	Discounted future reward
$P(s', r s, a)$	Transition probability of getting to the next state s' from the current state s with action a and reward r
$\pi_\theta(\cdot)$	Policy corresponding to parameter θ
$\pi_\theta(a s)$	Stochastic policy (agent behavior strategy). Probability of taking action a in state s given parameter vector θ
$\mu(s)$	Deterministic policy; Either π or μ is learned through reinforcement learning algorithm
$V_w(\cdot)$	Value function parameterized by w
$V(s)$	State-value function measures the expected return of state
$V^\pi(s)$	The value of state s with policy π is followed
$Q_w(\cdot)$	Action value function parameterized by w
$Q(s, a)$	Action-value function evaluates the expected return of a pair of state and action (s, a)
$Q^\pi(s, a)$	the value of (state, action) pair with policy π is followed

$A(s, a)$	Advantage function $A(s, a) = Q(s, a) - V(s)$
$J(\theta)$	Objective function
$d^\pi(s)$	stationary distribution of Markov chain for π_θ
$L(\theta)$	Policy Loss
$r(\theta)$	Probability ratio of new policy over old policy
$\nabla \pi_\theta(a s)$	column vector of partial derivatives of $\pi_\theta(a s)$ with respect to θ
$\nabla J(\theta)$	column vector of partial derivatives of $J(\theta)$ with respect to θ

Chapter 1

Introduction

1.1 Motivation

Singularity Avoidance Control of VSCMG

Evident presence of singularities in Control Moment Gyroscope (CMG) and escaping them by adding an extra degree of freedom by using Variable Speed Control Moment Gyroscope (VSCMG) to escape singular states is highly complex and nonlinear multi-input multi-output problem making it suitable choice to be evaluated on machine learning models. Moreover, a sub-optimal neural network approximation of nonlinear optimum function requires much less computing resources and memory storage than optimum guidance law[5]. Although machine learning based models are widely used in everyday applications ranging from image processing, weather prediction to Alpha Go being the first computer program to defeat human player in game of Go, [6] their use in mission-critical task is limited. This thesis is to evaluate the performance of Neural Network based control model.

The Test Bench

It is difficult to evaluate the performance of the control law on real hardware and always been challenging to carry out hardware in the loop simulation of the attitude control system on the ground. Implementing complete 360 degrees of angular freedom of three body axes observed in orbit is indispensably difficult to attain inside ground-based laboratory. There has been a wide variety of technological solutions proposed and implemented since the beginning of the space age. Compromising with a reduced degree of freedom a platform balancing on sharp pin with its center of mass kept closer to pivot is chosen to keep the cost of the entire test setup as low as possible. Accessibility of 3D printing technology provides leverage for rapid prototyping of complex geometries. Goal behind hardware setup design is to provide an educational platform for preliminary evaluation and hardware in loop simulation of spacecraft attitude control system.

*“It doesn’t matter how beautiful your theory is, it doesn’t matter how smart you are.
If it doesn’t agree with experiment, it’s wrong.”*

- Richard P. Feynman

1.2 Literature Survey

Attitude Control System (ACS) being the primary subsystem of any spacecraft mission, based on the mission requirements a spacecraft must perform slew maneuvers for precise retargeting and maintaining desired state in presence of external disturbances. Important components of attitude determination and Control System are estimating the state of spacecraft using observations from sensors, actuators to provide required control torque towards reaching desired state and control algorithm to evaluate best inputs for actuators. Various types of actuators used in space missions each having its advantages and drawbacks over others. Typical examples are thrusters, magneto torquers, reaction wheels and control moment gyroscopes. Depending on mission requirements there are possible passive ways to maintain attitude of spacecrafts incorporating spin stabilization, solar sail, and gravity gradient.



Figure 1.1. NanoAvionics (4RW0) integral four - reaction wheels redundant 3-axis control system

Large spacecraft typically used in human spaceflight missions requires large and fast attitude maneuvers, this large demand torque requirement is generally achieved using reaction thrusters. Spacecrafts such as Apollo, Soyuz reentry vehicle used thruster-based ACS. Most recently SpaceX Dragon capsule is equipped with 16 DRACO thrusters [7] for orbit and attitude adjustment capable of producing 400N thrust each.[8] Although being capable of producing large amount of control torques, mission life is limited by finite amount of fuel moreover exhaust fumes may have adverse effects on payload.

For long duration missions having no possible means of refueling and high pointing accuracy requirements such as Hubble, Kepler Telescopes or optical communication demonstrator like Lunar Atmosphere and Dust Environment Explorer (LADEE), Momentum Exchange devices such as Reaction Wheel (RW) or Reaction Wheel (RW) are employed. Perhaps only difference is RWs are at rest at the beginning of mission, whereas MWs are spinning at maximum speed giving gyroscopic stiffness to spacecraft. Reaction Wheels are used for ACS. Reaction Wheel is a momentum storage device consist of high inertia flywheel attached to an electric brush-less

motor with its spin axis kept constant and aligned with spacecraft body. Torque is produced around axis of rotation by changing spin speed of flywheel, since total angular momentum of spacecraft must be conserved, spacecraft counter rotates proportionally to inertia ratio of body and reaction wheel. Very small and precise torques are produced by accelerating flywheels. Satellites are equipped with at least three reaction wheels are required to have complete attitude control capability some use four reaction wheels configuration for redundancy in case of failure as shown in Figure 1.1. Excess energy produced by solar panels during exposure to sun can be stored in RW by means of momentum hence also known as mechanical batteries. Momentum Wheels can be used for both attitude control and mechanical batteries by incorporating Integrated Power Attitude Control System (IPACS). [9]

Apart from being very quick and precise internal torque production capabilities Reaction Wheels are limited by maximum angular momentum storage capacity and undergoes saturation. Inability to counteract disturbances on reaching maximum speed is major drawback and thus Reaction wheels must be used with other external torque-based actuators for de-saturation. For large satellites, thruster-based ACS is used for denaturation whereas small satellites often equipped with Magneto Torquers. Current passed through coil of electromagnet attached to spacecraft which creates magnetic dipole. Produced torque is vector product of ambient magnetic flux density vector and magnetic dipole of electromagnet.

Spinning mass has inherent tendency to maintain its axis of rotation. If spin axis is tilted a torque is observed transverse to spin and tilt axis this phenomenon is known as gyroscopic couple. A Control Moment Gyroscope is momentum exchange device consist of a flywheel and one or two motorized gimbals to tilt its spin axis. Flywheel spinning at high angular velocity, hence having high angular momentum. Large "torque amplification" caused by gyroscopic effect produced due to changing orientation of flywheel spin axis is vector cross product of angular momentum of flywheel and velocity of gimbal axis rotation.[10] CMGs are more power efficient than MWs since maintaining wheel spin requires small amount of power. CMGs are classified in two main categories based on number of degrees of freedom of RW spin axis. Single Gimble Control Moment Gyroscope (SGCMG) has one motorized gimble whereas Double Gimble Control Moment Gyroscope (DGCMG) incorporates two gimbals to tilt spin axis of flywheel. SGCMGs are more power efficient than DGCMG since to produce same amount of torque DGCMG requires more electric power. DGCMGs are heavier, requires complex electromechanical components to drive three nested motors. Only advantage of DGCMG is when momentum storage is primary requirement. As size of reaction wheel increased the complexity of DGCMG and its support mechanism keeps increasing due to extra gimbal and it becomes no longer feasible. It is also important to avoid alinement of two axis to prevent gimble lock.[11]

One of the earliest research related to use of control moment gyroscope as secondary actuator for gravity gradient stabilize satellite dates to 1964, CMG can act as both actuator and gyro sensor to sense vehicle rates.[12] Liska proposed torque amplification of several hundred to one by incorporating two independent DGCMGs for 0.01arc sec pointing accuracy with coning type gimble suspension for gimbal synchronization.[13] NASA's Marshall Space Flight Center developed manned space station Skylab launched in 1976 was first spacecraft to use CMG for ACS.[14]

Software-determined attitude determination to provide general maneuvering ability achieved by making shift from analog controller to fully digital processing system. [15] First test of USSR CMG also referred as gyrodyne by Russian cosmonauts' dates to 1974 onboard Salut-3, and standard ACS component for Salut 6 and later missions. Configuration of six SGCMG were used in USSR Mir spacecraft. [16] Largest DGCMG ever used are installed on International Space Station (ISS) can produce torque up to 258Nm and acts as stations primary attitude control, thrusters are backup for large attitude maneuvers.[17]

Although CMGs can produce large torque amplification they come with inherent problem of singularity. Phenomenon of inability to provide torque in certain direction based on orientation of flywheel spin axis. Singularity problem can be avoided by adding capability to change the spin speed of flywheel. Avoiding or escaping singular states is possible with added extra degree of freedom of reaction wheel speed hence called Variable Speed Control Moment Gyroscopes a Reaction Wheel mounted on gimble motor. In addition to gyroscopic torques VSCMG produces torque by changing reaction flywheel speed. Direction of torque vector is dependent of orientation of wheel spin axis and gimble motion. Various numerical and geometrical steering approaches are demonstrated for singularity avoidance. Such as Gain scheduled steering and control [18] Singular Value Decomposition (SVD) based gimble speed planning of the transient process [19]., Robust pseudo inverse method and null motion. Nonlinear Model predictive control realized by Wu. et al. on two VSCMG in scissor pair configuration. Capability to modulate angular momentum of flywheel can be used to store energy in the form of angular momentum. Yoon, et al. discussed special control algorithm Integrated Power Attitude Control System (IPACS) on VSCMG cluster. [20]. Instead of computing pseudo inverse, Jacobian transpose method can be used for VSCMG steaming. [21] Quang et al. investigated $\theta - D$ controller with nonlinear state dependent factorization modeling. This adaptive controller is robust in case of RW failure. [22]

A heuristic based inverse kinematics method Forward and Backward Reaching Inverse Kinematics for steering of control moment gyroscope proposed by Meldrom, et al. gives approximate but computationally less expensive results.[23]

F. Santoni in 1996 proposed use of neural network trained with optimal nonlinear guidance function, sub-optimal neural network is used to reduce CPU load and memory storage [5]. Machine Learning based models are widely used in classification probability prediction problems of finite discrete domain. Recent advancement in reinforcement learning and increased computational performance of microcomputers paved way to solve search problems with large domain. Reinforcement Learning is way of model training a where Agent learns the policy by interacting with environment. Each action performed by agent based on observation in environment has reward associated with it. Optimum policy is having maximum reward. OpenAI Five trained with 2 million frames per 2 seconds leveraging reinforcement learning technique defeated world champions in highly complex real time strategy e-sport game Dota 2.[24]. Although, reinforcement learning is not limited to discrete deterministic environment. Real life robotics control problems are nonlinear in nature and require complex steering and control method, problem is continuous, has infinite search space non-deterministic environment. OpenAI trained neural network to solve

a Rubik's cube with a human like robotic hand manipulator, Automatic Domain Randomization is used for training. The model is capable of handling disturbances which had never introduced during training process. [25]

Various VSCMG attitude dynamics test bench has been implemented. Candinia and Santoni manufactured miniature test bed with two axis free moment provided by air bearing and mass balancing around center of gravity is achieved using automatically by using linear actuators. [26] Gui et al. talk about testbed with free attitude motion is achieved using spherical air bearing [27]. Vishvanath et al. deal with design of miniature VSCMG for cubesat, attitude sensors of smartphones are used for state estimation with independent low cost 8bit microcontroller for attitude control.[28] Although most of the commercially available attitude control test beds uses air bearing. Air bearing are difficult to manufacture and expensive for sufficiently low friction requirements. Lorenzo Arena et al. produced a research on use of platform balancing on sharp pinpoint with its center of mass kept close to pivot. Outrunner brushless motors are used since their inertia is sufficient and does not require additional flywheel assembly, research demonstrate FPGA based design for fault tolerant application. [29]

1.3 Thesis Outline

Scope of this thesis is divided in three parts. First part deals with Mathematical Background. Starting from formulation kinematics and rigid body dynamics, reference frame and axis definition of CMG and complete nonlinear model VSCMG is realized in chapter 2. Singularity analysis, momentum envelope and singular surface of VSCMG is discussed in chapter 3. Controller design, Lyapunov stability analysis and pseudo inverse based steering law is derived in chapter 4. Finally, computer simulations performed for preliminary verification of control algorithm and sizing of hardware component.

Second part of this thesis is discussion of AI based controller methods, Neural Network and Reinforcement Learning. Machine learning approach especially Deep Neural Network and policy gradient training algorithms are discussed in chapter 5. Complete policy has been implemented and verified on simulation of spacecraft with VSCMG.

Mechanical Design, Fabrication and electronics and embedded system for hardware in Loop simulation of complete VSCMG Test Bench is implemented in third part of thesis described in chapter 6 to chapter 9.

Chapter 2

Equation(s) of Motion

This chapter elaborates selection of reference system, mathematical definition and generalized nonlinear equations of motion of a rigid spacecraft equipped with array of SGCMG units. First inertial and body fixed reference frames assigned to individual components and rotation among frames is defined. Right hand rule is followed for representing rotation of axis in three dimensional space throughout the thesis considering thumb is pointing towards axis of rotation and direction of rotation along curled fingers. Afterwards, inertia property of individual components, their assembly and its derivative is formulated. Later angular momentum of each rotating body is evaluated. Finally, equation of motion is realized for rigid body spacecraft with generic number of SGCMG modules.

2.1 Frame of reference

To realize attitude of rigid body and its evaluation over time as function of initial angular velocity and applied torques, reference frames and rotation among reference needs to be introduced. We attach body frame \mathcal{F}_b having basis vectors $(\hat{b}_1, \hat{b}_2, \hat{b}_3)$ and the orientation of \mathcal{F}_b with respect to inertial reference frame $\mathcal{F}i$ associated basis vector $(\hat{e}_1, \hat{e}_2, \hat{e}_3)$ describes attitude of spacecraft. Rotation from one frame of reference to other can be described with Rotation matrix, Euler axis angles representation, Davenport chained rotations, and unit quaternions.

2.1.1 Rotation Matrix

Three mutually perpendicular basis vectors describes reference frame in Euclidean space. Rotation is represented by specifying vector components of one frame with respect to other. Each column describe components of unit vector.

$$\mathbf{R}_{3 \times 3} = \begin{pmatrix} \vdots & \vdots & \vdots \\ \hat{e}_1 & \hat{e}_2 & \hat{e}_3 \\ \vdots & \vdots & \vdots \end{pmatrix} \quad (2.1)$$

$$\begin{aligned} \mathbf{R}^T \mathbf{R} &= \mathbf{R} \mathbf{R}^T = \mathbf{I}_{3 \times 3} \\ \det \mathbf{R} &= +1 \end{aligned} \quad (2.2)$$

R is real and orthogonal matrix with eigenvalues $\{1, e^{\pm i\theta}\}$, with unit determinant. Successive rotations are represented as product of matrix in order of rotation performed.

$${}^B \mathbf{R}_I = {}^B \mathbf{R}_n {}^n \mathbf{R}_{n-1} \cdots {}^2 \mathbf{R}_1 {}^1 \mathbf{R}_I \quad (2.3)$$

2.1.2 Euler Axis angle

Euler rotation theorem states If \mathbf{R} satisfies Equation 2.2 then there exist non zero vector $\hat{\mathbf{a}}$ which satisfies $\mathbf{R}\hat{\mathbf{a}} = \hat{\mathbf{a}}$. Any arbitrary composition of rotations of a rigid body can be represented as single rotation by angle φ about unique axis $\hat{\mathbf{a}}$ which remains unchanged by the rotation.[30] Rotation matrix \mathbf{R} relates certain vector \mathbf{v} and corresponding rotated vector $\mathbf{v}' = \mathbf{R}\mathbf{v}$ Rodrigues rotation formula for \mathbf{R} as function of unit vector $\hat{\mathbf{a}}$ along the rotation axis and by angle φ is

$$\mathbf{R}(\hat{\mathbf{a}}, \varphi) = \cos \varphi \mathbf{I} + (1 - \cos \varphi) \hat{\mathbf{a}} \otimes \hat{\mathbf{a}} + \sin(\varphi) \hat{\mathbf{a}}^\times \quad (2.4)$$

Here \mathbf{I} is identity matrix and vector with superscript \times is a skew symmetric matrix equivalent for cross product of vector, commonly referred as "Hat-Map" transformation denoted with a^\times represented as

$$a^\times = \begin{pmatrix} 0 & -a_3 & a_2 \\ a_3 & 0 & -a_1 \\ -a_2 & a_1 & 0 \end{pmatrix}$$

With dextro-rotation assumption, \mathbf{R} moves the vectors but not co-ordinate axes hence gives active point of view of rotation.

2.1.3 Davenport chained rotations

Davenport chained rotations are three chained sequence of consecutive intrinsic rotation about body-fixed axes. Based on number of axes used to represent rotation Davenport chain rotations are characterized in two types, "Generalized Euler rotations" if two rotation occurs about same axis and "Generalized Tait–Bryan rotations" if each rotations occur about different axis. Order in which rotations are performed is not cumulative so must be specified. Three numbers indicates axis about which rotations are performed. For example Euler 313 commonly used in aerodynamics to describe satellites position with other parameters. Sequence involves first rotation about third axis, second rotation about first axis and finally, third rotation about third axis. Tait-Bryan angle sequence 123 is commonly used to describe attitude of aircraft and individual rotation is called roll, pitch and yaw (ϕ, θ, ψ) . Classic Euler angles are first introduced by Euler for orbital mechanics and rigid body dynamics. Problem with classic Euler angle is, they become singular near zero angles, on the other hand Tait–Bryan angles become singular when second rotation is $\pi/2$ condition also referred as Gimble Lock.

Elaboration of Tait–Bryan R_{123} is product of three individual coordinate rotation about each axis $R_i : \mathbb{R} \rightarrow SO(3)$ for $i \in \{1, 2, 3\}$ as shown below:

$$R_1(\phi) = \begin{pmatrix} 1 & 0 & 0 \\ 0 & \cos \phi & \sin \phi \\ 0 & -\sin \phi & \cos \phi \end{pmatrix}$$

$$R_2(\theta) = \begin{pmatrix} \cos \theta & 0 & -\sin \theta \\ 0 & 1 & 0 \\ \sin \theta & 0 & \cos \theta \end{pmatrix}$$

$$R_3(\psi) = \begin{pmatrix} \cos \psi & \sin \psi & 0 \\ -\sin \psi & \cos \psi & 0 \\ 0 & 0 & 1 \end{pmatrix}$$

Performing the multiplication, the complete rotation from the body frame to the inertial frame is given by

$$R_{123}(\phi, \theta, \psi) = R_1(\phi)R_2(\theta)R_3(\psi)$$

$$R_{123}(\phi, \theta, \psi) =$$

$$\begin{pmatrix} \cos \psi \cos \theta & \cos \psi \sin \phi \sin \theta - \cos \phi \sin \psi & \sin \phi \sin \psi + \cos \phi \cos \psi \sin \theta \\ \cos \theta \sin \psi & \cos \phi \cos \psi + \sin \phi \sin \psi \sin \theta & \cos \phi \sin \psi \sin \theta - \cos \psi \sin \phi \\ -\sin \theta & \cos \theta \sin \phi & \cos \phi \cos \theta \end{pmatrix}$$

2.1.4 Quaternions

Quaternions were introduced by William Rowan Hamilton as four dimension vector having three imaginary dimensions describing space and a real number perpendicular to it in fourth dimension. Quaternion rotation is written as combination of scalar with hyper-complex numbers in the form of

$$\mathbf{q} = q_0 + q_1 \mathbf{i} + q_2 \mathbf{j} + q_3 \mathbf{k} \quad (2.5)$$

where $\{q_0, q_1, q_2, q_3\} \in \mathbb{R}$ and i, j, k are the fundamental quaternion units. Hamiltonian representation of quaternion follows ¹

$$\mathbf{i}^2 + \mathbf{j}^2 + \mathbf{k}^2 = \mathbf{ijk} = -1 \quad (2.6)$$

The term $\mathbf{i}, \mathbf{j}, \mathbf{k}$ represents three unit Cartesian with imaginary properties and satisfies following relation

$$\begin{aligned} \mathbf{ij} &= \mathbf{k} & \mathbf{ij} &= -\mathbf{k} \\ \mathbf{jk} &= \mathbf{i} & \mathbf{jk} &= -\mathbf{i} \\ \mathbf{ki} &= \mathbf{j} & \mathbf{ki} &= -\mathbf{j} \end{aligned}$$

A quaternion $\mathbf{q} \in \mathbb{H}$ is represented as vector with scalar q_0 and $\mathbf{qv} = [q_1 \ q_2 \ q_3]^T$ as

$$\mathbf{q} = [q_0 \ q_1 \ q_2 \ q_3]^T = \begin{bmatrix} q_0 \\ \mathbf{qv} \end{bmatrix}$$

¹Apart from Hamiltonian representation, an alternative standard representation "JPL" [31] has component order as $q = q_0i + q_1j + q_2k + q_3$ holds algebraic relation $\mathbf{i}^2 + \mathbf{j}^2 + \mathbf{k}^2 = \mathbf{ijk} = 1$

Quaternion norm conjugate and inverse is computed as

$$\mathbf{q}^* = \begin{bmatrix} q_0 \\ -\mathbf{q}_v \end{bmatrix} \quad (2.7)$$

$$\|\mathbf{q}\| = \sqrt{\mathbf{q}\mathbf{q}^*} = \sqrt{q_0^2 + q_1^2 + q_2^2 + q_3^2} \quad (2.8)$$

$$\mathbf{q}^{-1} = \frac{\mathbf{q}^*}{\|\mathbf{q}_v\|^2} \quad (2.9)$$

Quaternion product is noncommutative, defined in terms of scalar and vector part, product of two quaternion \mathbf{q}_1 and \mathbf{q}_2 evaluated as

$$\begin{aligned} \mathbf{q}_1 \otimes \mathbf{q}_2 &= \begin{bmatrix} q_{1,0} \\ q_{1,v} \end{bmatrix} \otimes \begin{bmatrix} q_{2,0} \\ \mathbf{q}_{2,v} \end{bmatrix} \\ &= \begin{bmatrix} q_{1,0}q_{2,0} - q_{1,v} \cdot q_{2,v} \\ q_{1,0}q_{2,v} + q_{2,0}q_{1,v} + \mathbf{q}_1^\times \mathbf{q}_{2,v} \end{bmatrix} \end{aligned} \quad (2.10)$$

Hereafter, unit norm quaternions, a special class of quaternion are followed throughout the thesis which poses following property

$$\|\mathbf{q}\| = \sqrt{q_0^2 + q_1^2 + q_2^2 + q_3^2} = 1 \quad (2.11)$$

Rotation in three dimensions can be represented with unit quaternions, they have been employed in several disciplines such as computer graphics, aerodynamics, quantum computing, robotics and to describe attitude of rigid body. Consider a vector $\mathbf{x} \in \mathbb{R}^3$ in inertial frame \mathcal{F}_i and \mathbf{x}' being same vector viewed from body fixed frame then we get rotation of vector \mathbf{x} as

$$\begin{aligned} \begin{bmatrix} 0 \\ \mathbf{x}' \end{bmatrix} &= \mathbf{q} \cdot \begin{bmatrix} 0 \\ \mathbf{x} \end{bmatrix} \cdot \mathbf{q}^{-1} \\ &= \begin{bmatrix} 1 & \mathbf{0}^T \\ \mathbf{0} & \mathbf{R}(\mathbf{q}) \end{bmatrix} \begin{bmatrix} 0 \\ \mathbf{x}' \end{bmatrix} \\ \mathbf{x}' &= \mathbf{R}(\mathbf{q})\mathbf{x} \\ \mathbf{x} &= \mathbf{R}(\mathbf{q})^T\mathbf{x}' \end{aligned}$$

where rotation matrix \mathbf{R} as function of \mathbf{q} shown below.

$$\begin{aligned} \mathbf{R}(\mathbf{q}) &= \left(q_0^2 - \mathbf{q}_v^T \mathbf{q}_v \right) \mathbf{I}_{3 \times 3} + 2\mathbf{q}_v \mathbf{q}_v^T + 2q_0 \mathbf{q}^\times \\ \mathbf{R}(\mathbf{q}) &= \begin{pmatrix} 1 - 2q_2^2 - 2q_3^2 & 2q_1q_2 - 2q_0q_3 & 2q_1q_3 + 2q_0q_2 \\ 2q_1q_2 + 2q_0q_3 & 1 - 2q_1^2 - 2q_3^2 & 2q_2q_3 - 2q_0q_1 \\ 2q_1q_3 - 2q_0q_2 & 2q_2q_3 + 2q_0q_1 & 1 - 2q_1^2 - 2q_2^2 \end{pmatrix} \end{aligned} \quad (2.12)$$

Relationship with axis angle $\hat{\mathbf{e}} = [e_1 \ e_2 \ e_3]^T$ and rotation by angle φ is expressed as follows

$$\mathbf{q} = \begin{bmatrix} \cos \frac{\varphi}{2} \\ \hat{\mathbf{e}} \sin \frac{\varphi}{2} \end{bmatrix} \quad (2.13)$$

Let us write spacecraft attitude quaternion having body fix frame \mathcal{F}_b with respect to inertial frame frame \mathcal{F}_i as \mathbf{q} and desired attitude in body frame \mathcal{F}_d is \mathbf{q}_d . Magnitude of angular displacement between frame \mathcal{F}_b and frame \mathcal{F}_d is described by angle ε by eigenaxis rotation about $\hat{\mathbf{e}}$ is error between current and desired attitude attitude $\mathbf{q}_e = [\mathbf{q}_{e,0}, \mathbf{q}_{e,v}^T]^T$.

$$\mathbf{q}_d \mathbf{q}_e = \mathbf{q}$$

premultipling by conjugate \mathbf{q}_d^* , we get error quaternion.

$$\mathbf{q}_e = \mathbf{q}_d^* \mathbf{q}$$

$$\begin{pmatrix} \mathbf{q}_{e,0} \\ \mathbf{q}_{e,v} \end{pmatrix} = \begin{pmatrix} \cos(\varepsilon/2) \\ \hat{\mathbf{e}} \sin(\varepsilon/2) \end{pmatrix} = \begin{pmatrix} q_0 q_{d,0} + \mathbf{q}^T \mathbf{q}_d \\ -q_0 \mathbf{q}_{d,v} + q_{d,0} \mathbf{q}_v - \mathbf{q}_d \times \mathbf{q}_v \end{pmatrix} \quad (2.14)$$

2.2 Kinematics

Kinematic relation of rigid body describes changing attitude over time of body fixed reference frame \mathcal{F}_b with inertial reference frame \mathcal{F}_i . To identify kinematic differential equation, let us consider instantaneous angular velocity vector $\boldsymbol{\omega}$ of frame \mathcal{F}_b with respect to frame \mathcal{F}_i as viewed from \mathcal{F}_b frame orthogonal components described as

$$\boldsymbol{\omega} = \omega_1 \hat{\mathbf{b}}_1 + \omega_2 \hat{\mathbf{b}}_2 + \omega_3 \hat{\mathbf{b}}_3$$

Then $\frac{\mathcal{F}_i d}{dt} \{\hat{\mathbf{b}}\}$ is derivative of \mathcal{F}_b base vectors taken in \mathcal{F}_i , applying transport theorem

$$\frac{\mathcal{F}_i d}{dt} \hat{\mathbf{b}}_i = \frac{\mathcal{F}_b d}{dt} \hat{\mathbf{b}}_i + \boldsymbol{\omega} \times \hat{\mathbf{b}}_i \quad (2.15)$$

Selection of attitude coordinate system to represent rotation of spacecraft is crucial in order to simplify mathematics and avoid geometrical or numerical singularity, quaternion kinematics is used in this thesis. In spite of the fact that quaternions are less intuitive, they does not undergo trivial singularity presence in Euler angles moreover quaternions are linear in nature. In this section we will realize quaternion kinematic relation.

Let \mathbf{q} represent attitude of spacecraft with respect to inertial reference frame at time t and \mathbf{q}' be attitude quaternion after $t + \Delta t$ about axis $\hat{\mathbf{e}}$ and by angle $\Delta\varphi$ rotation using Equation 2.13

$$\dot{\mathbf{q}} = \mathbf{q}(t + \Delta t) = \mathbf{q}' = \begin{bmatrix} \cos \frac{\Delta\varphi}{2} \\ \hat{\mathbf{e}} \sin \frac{\Delta\varphi}{2} \end{bmatrix} \quad (2.16)$$

assuming very small angle $\Delta\varphi = \omega \Delta t$ thus $\cos \frac{\Delta\varphi}{2} \approx 1$ and $\sin \frac{\Delta\varphi}{2} \approx \frac{\Delta\varphi}{2}$

$$\begin{aligned} \dot{\mathbf{q}} &= \frac{1}{2} \begin{bmatrix} -\boldsymbol{\omega} \cdot \mathbf{q} \\ q_0 \boldsymbol{\omega} - \mathbf{q}^\times \end{bmatrix} \\ &= \frac{1}{2} \begin{bmatrix} 0 & -\boldsymbol{\omega}^T \\ \boldsymbol{\omega} & -\boldsymbol{\omega}^\times \end{bmatrix} \begin{bmatrix} q_0 \\ \mathbf{q} \end{bmatrix} \end{aligned} \quad (2.17)$$

Considering constant angular velocity for small time step evaluation in body frame a quaternion kinematics equation for rigid body derived as follows.

$$\dot{\mathbf{q}} = \frac{1}{2} \begin{pmatrix} 0 & -\omega_1^b & -\omega_2^b & -\omega_3^b \\ \omega_1^b & 0 & -\omega_3^b & \omega_2^b \\ \omega_2^b & \omega_3^b & 0 & -\omega_1^b \\ \omega_3^b & -\omega_2^b & \omega_1^b & 0 \end{pmatrix} \begin{pmatrix} q_0 \\ q_1 \\ q_2 \\ q_3 \end{pmatrix} \quad (2.18)$$

As seen from inertial frame quaternion derivative in terms of angular velocity can be evaluated by

$$\begin{aligned} \omega^i &= \mathbf{q}^* \omega^i \mathbf{q} \quad \text{or} \quad \omega^b = \mathbf{q}^* \omega^b \mathbf{q} \\ \dot{\mathbf{q}} &= \frac{1}{2} \omega^i(\omega^b) \mathbf{q} = \frac{1}{2} \begin{pmatrix} 0 & -\omega_1^i & -\omega_2^i & -\omega_3^i \\ \omega_1^i & 0 & \omega_3^i & -\omega_2^i \\ \omega_2^i & -\omega_3^i & 0 & \omega_1^i \\ \omega_3^i & \omega_2^i & -\omega_1^i & 0 \end{pmatrix} \begin{pmatrix} q_0 \\ q_1 \\ q_2 \\ q_3 \end{pmatrix} \end{aligned} \quad (2.19)$$

Since no analytical simulation exists for changing angular velocity, kinematics is integrated numerically using Adaptive Runge–Kutta method.

2.3 Dynamics

In order to archive complete system dynamics of spacecraft with array of N - VSCMGs, physical properties such as inertia and angular momentum of a single control moment gyroscope is evaluated first and latter for arrangement of spacecraft with multpile VSCMG units . Body fixed frame \mathcal{F}_b with basis vector $\{\hat{b}_1, \hat{b}_2, \hat{b}_3\}$ attached to center of mass of continuum rigid body at distance \vec{r}_0 from \mathcal{F}_i as shown in Figure 2.1. Body is rotating at angular velocity $\vec{\omega} = [\omega_1 \ \omega_2 \ \omega_3]^T$ as shown in fig. The angular momentum $\delta\vec{h}$ of infinitesimally small mass δm at position $\vec{r} = [x_1 \ y_2 \ z_3]^T$ in body, moving at velocity $\tilde{\mathbf{v}} = \vec{\omega} \times \vec{r}$ is expressed as

$$\delta\vec{h} = \vec{r} \times \delta m \tilde{\mathbf{v}}$$

Total angular momentum for rigid body is given by

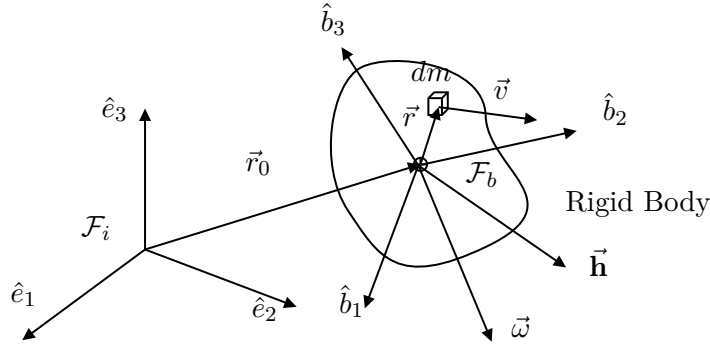


Figure 2.1. Representation of Rigid body rotation in space

$$\begin{aligned}\vec{h} &= \int_{\mathcal{B}} (\vec{r} \times \tilde{\mathbf{v}}) \delta m \\ \vec{h} &= \int_{\mathcal{B}} [\vec{r} \times (\vec{\omega} \times \vec{r})] \delta m\end{aligned}$$

Expanding the vector quantities we get

$$\vec{h} = h_1 \hat{e}_1 + h_2 \hat{e}_2 + h_3 \hat{e}_3$$

Thus angular momentum vector in body frame is given by

$$\begin{aligned}\vec{h}_B &= \mathbf{I} \omega_B \\ \vec{h}_B &= \begin{pmatrix} I_x & -I_{xy} & -I_{xz} \\ -I_y & I_y & -I_{yz} \\ I_z & -I_{zy} & I_z \end{pmatrix} \begin{pmatrix} \omega_1 \\ \omega_2 \\ \omega_3 \end{pmatrix}\end{aligned}\tag{2.20}$$

here components of inertia tensor \mathbf{I} are moment of inertia I_x, I_y, I_z and product of inertia I_{xy}, I_{yz}, I_{xz} are

$$\begin{aligned}I_x &= \int_{\mathcal{B}} (y^2 + z^2) \delta m; & I_y &= \int_{\mathcal{B}} (x^2 + z^2) \delta m; & I_z &= \int_{\mathcal{B}} (x^2 + y^2) \delta m \\ I_{xy} &= \int_{\mathcal{B}} (xy) \delta m; & I_{xz} &= \int_{\mathcal{B}} (xz) \delta m; & I_{yz} &= \int_{\mathcal{B}} (yz) \delta m\end{aligned}$$

Total rotational kinetic energy is evaluated as:

$$\mathcal{T} = \frac{1}{2} \vec{\omega} \cdot \hat{\mathbf{h}} = \frac{1}{2} \vec{\omega}_B^T \cdot \hat{\mathbf{h}}_B \quad (2.21)$$

2.3.1 System Representation

Let us consider a generic CMG attached to rigid free floating spacecraft body with respect to inertial frame \mathcal{F}_i having basis $\{\hat{e}_1, \hat{e}_2, \hat{e}_3\}$ as shown in Figure 2.2. Body frame \mathcal{F}_b with basis vector $\{\hat{b}_1, \hat{b}_2, \hat{b}_3\}$ is used to represent attitude of spacecraft with respect to \mathcal{F}_i . Another reference frame \mathcal{F}_g attached to the center of mass having basis vector $\{\hat{g}, \hat{s}, \hat{t}\}$. Gimbal axis is aligned with unit vector \hat{g} and spin axis attached to \hat{s} and orthogonal to gimbal axis. Transverse axis \hat{t} is described as $\hat{t} = \hat{g} \times \hat{s}$ making it mutually perpendicular to \hat{g} and \hat{s} . Gimbal motor rotates \hat{s} and \hat{t} with respect to \mathcal{F}_b

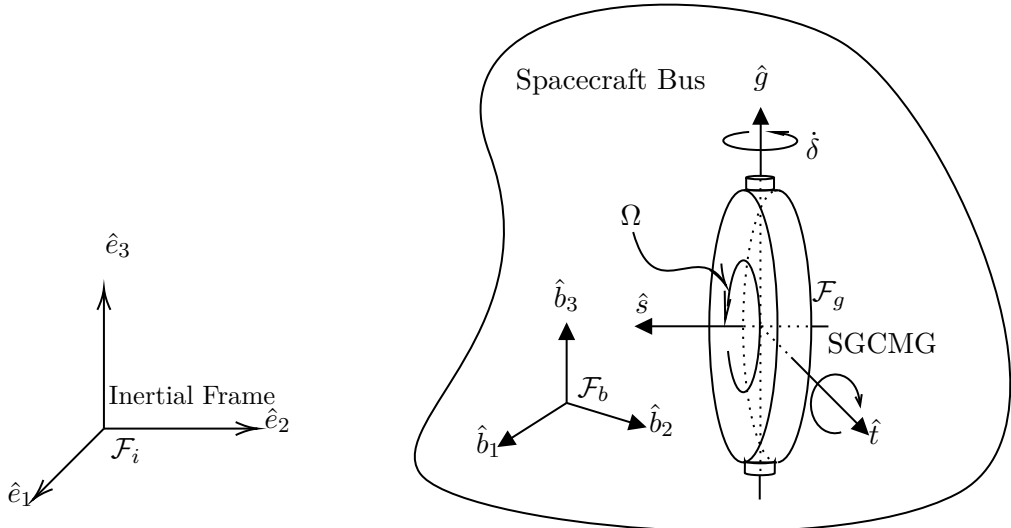


Figure 2.2. Schematic illustration of Spacecraft with Momentum exchange device

2.3.2 Control Moment Gyro Model

A generic CMG contains a flywheel spinning at constant rate Ω , spin axis is rotated about fixed axis (gimbal axis), this action exerts gyroscopic torque on spacecraft body. Rotation angle δ is referred as gimbal angle. Figure 2.3 shows generic control moment gyroscope and its axis representation.

Starting from initial gimbal angle δ_0 spin and transverse axis as function of δ are evaluated in \mathcal{F}_b as

$$\mathbf{R}(\delta) = \cos \delta \mathbf{1} + (1 - \cos \delta) \hat{\mathbf{g}} \otimes \hat{\mathbf{g}} + \sin(\delta) \hat{\mathbf{g}}^\times \quad (2.22)$$

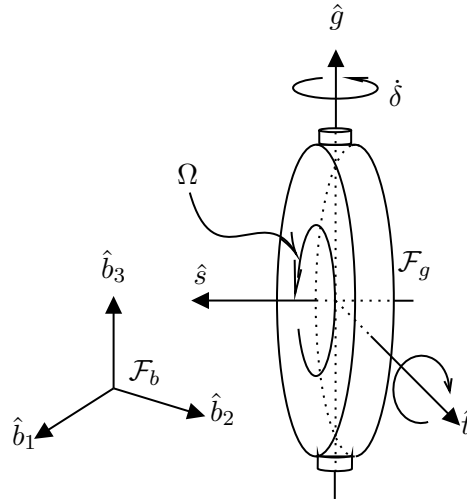


Figure 2.3. Axis definition for generic Control Moment Gyroscope

$$\begin{aligned}\hat{s}(t) &= \mathbf{R}(\delta) \hat{s}(t_0) \\ \hat{t}(t) &= \mathbf{R}(\delta) \hat{t}(t_0)\end{aligned}\quad (2.23)$$

$$\begin{pmatrix} \hat{s}(t) \\ \hat{t}(t) \end{pmatrix} = \begin{pmatrix} \cos(\delta - \delta_0) & \sin(\delta - \delta_0) \\ -\sin(\delta - \delta_0) & \cos(\delta - \delta_0) \end{pmatrix} \begin{pmatrix} \hat{s}(t_0) \\ \hat{t}(t_0) \end{pmatrix} \quad (2.24)$$

Angular velocity vector gimbal frame \mathcal{F}_g with respect to \mathcal{F}_b is

$$\omega_{\mathcal{F}_g/\mathcal{F}_b} = \dot{\delta} \hat{g} \quad (2.25)$$

and angular velocity vector of reaction wheel frame \mathcal{F}_w in \mathcal{F}_g is represented as

$$\omega_{\mathcal{F}_W/\mathcal{F}_g} = \dot{\delta} \hat{s} \quad (2.26)$$

Gimbal inertia matrix expressed in \mathcal{F}_G as diagonal matrix with J_g^* are gimbal frame inertia along superscript * represented as spin \hat{s} transverse \hat{t} and \hat{g} axis Subscript G and W CMG are used to identify gimbal, RW and CMG respectively.

$$J_G = \begin{pmatrix} J_G^s & 0 & 0 \\ 0 & J_G^t & 0 \\ 0 & 0 & J_G^g \end{pmatrix}$$

Flywheel inertia J_W^s is much larger than gimbal inertia and is symmetric about \hat{g} therefore $\mathcal{F}_W J_W = \mathcal{F}_g J_s$ thus reaction wheel inertia about spin axis are given by J_W^s and $J_W^t = J_W^g$

$$J_W = \begin{pmatrix} J_W^s & 0 & 0 \\ 0 & J_W^t & 0 \\ 0 & 0 & J_W^t \end{pmatrix} \quad (2.27)$$

Constant diagonal matrix J_g and J_s are expressed in \mathcal{F}_b as

$$\begin{aligned} J_G &= J_G^s \hat{s} \hat{s}^T + J_G^t \hat{t} \hat{t}^T + J_G^g \hat{g} \hat{g}^T \\ J_W &= J_W^s \hat{s} \hat{s}^T + J_W^t \hat{t} \hat{t}^T + J_W^g \hat{g} \hat{g}^T \end{aligned} \quad (2.28)$$

and tensor of inertia for CMG system is sum of gimbal and reaction wheel inertia and written in \mathcal{F}_b as

$$J_{CMG} = J_{CMG}^s \hat{s} \hat{s}^T + J_{CMG}^t \hat{t} \hat{t}^T + J_{CMG}^g \hat{g} \hat{g}^T \quad (2.29)$$

CMG as asymmetric moving masses, note that center of mass of reaction wheel does may have offset from gimbal axis inertia property of spacecraft change with gamble rotation and are function of $\delta(t)$. Using axis angle rotation matrix $\mathbf{R}(\delta)$

$$J_{CMG}(\delta) = J_{CMG}^s \mathbf{R}(\delta) \hat{s}_0 \hat{s}_0^T \mathbf{R}(\delta)^T + J_{CMG}^t \mathbf{R}(\delta) \hat{t} \hat{t}^T \mathbf{R}(\delta)^T + J_{CMG}^g \hat{g} \hat{g}^T \quad (2.30)$$

We can see that J_{CMG} is not constant and in order to realize angular momentum of CMG in body frame we need to evaluate derivative of CMG inertia tensor

$$\begin{aligned} \dot{J}_{CMG} &= J_{CMG}^s [\dot{\hat{s}} \hat{s} + \hat{s} \dot{\hat{s}}] + J_{CMG}^t [\dot{\hat{t}} \hat{t} + \hat{t} \dot{\hat{t}}] \\ &= \dot{\delta} (J_{CMG}^s - J_{CMG}^t) [\hat{t} \hat{s} + \hat{s} \hat{t}] \end{aligned} \quad (2.31)$$

From Equation 2.31 we can say that derivative of CMG inertia tensor is function of gimbal velocity and difference in moment of inertia about spin and transverse axis. Since these are very small compared and \dot{J}_{CMG} is also very low compared to spacecraft inertia.

We have velocity ω of spacecraft body frame \mathcal{F}_b measured in inertial frame \mathcal{F}_i now angular velocity ω_G and ω_w of gimbal and flywheel are represented in terms gimbal angular velocity Ω_G and RW angular velocity Ω_W is

$$\begin{aligned} \omega_G &= \omega + \Omega_G = \omega + \dot{\delta} \hat{g} \\ \omega_W &= \omega + \Omega_W = \omega + \dot{\delta} \hat{g} + \Omega \hat{s} \end{aligned} \quad (2.32)$$

From Equation 2.31 and Equation 2.32 Gimbal angular momentum \mathcal{H}_G , RW angular momentum \mathcal{H}_W , and CMG angular momentum \mathcal{H}_{CMG} are evaluated as

$$\begin{aligned} \mathcal{H}_G &= J_G \cdot \omega_G \\ &= \omega + \dot{\delta} \hat{g} \\ &= J_G \cdot \omega + J_G^g \dot{\delta} \hat{g} \end{aligned} \quad (2.33)$$

RW Momentum,

$$\begin{aligned} \mathcal{H}_W &= J_W \cdot \omega_W \\ &= \omega + \dot{\delta} \hat{g} + \Omega \hat{s} \\ &= J_W \cdot \omega + J_W^g \dot{\delta} \hat{g} + J_W^s \Omega \hat{s} \end{aligned} \quad (2.34)$$

CMG Momentum is sum of RW and Gimbal momentum as,

$$\begin{aligned} \mathcal{H}_{CMG} &= \mathcal{H}_G + \mathcal{H}_W \\ &= (J_G + J_W) \cdot \omega + (J_G^g + J_W^g) \dot{\delta} \hat{g} + J_W \Omega \hat{s} \\ &= J_{CMG}(\delta) \cdot \omega + J_{CMG}^g \dot{\delta} \hat{g} + J_W^s \Omega \hat{s} \end{aligned} \quad (2.35)$$

From Equation 2.35 we can say that CMG angular momentum is function of body, gimbal, RW angular velocity and gimbal angle δ

2.4 Spacecraft Attitude Dynamics

Rigid body having angular momentum \mathcal{H} with respect to center of mass and applied torque τ , From newton Euler rigid body dynamics we know that rate of change of angular momentum of body is equal to torque applied to it. Time rate of change of angular momentum in body frame is

$$\begin{aligned}\frac{d\mathcal{H}}{dt} &= \tau \\ \dot{\mathcal{H}} &= \tau\end{aligned}\tag{2.36}$$

Using transport theorem derivative of angular momentum expressed in \mathcal{F}_I gives us Newton Euler equation for attitude dynamics.

$$\dot{\mathcal{H}} + \omega \times \mathcal{H} = \tau\tag{2.37}$$

Assuming the hypothesis of rigid body and neglecting all elastic properties of spacecraft in free falling orbit we can expand the torque τ as combination of disturbance torque τ_d external environmental torque τ_e and control torque \mathbf{u} thus Equation 2.37 becomes

$$\dot{\mathcal{H}} + \omega \times \mathcal{H} = \tau_d + \tau_e + \mathbf{u}\tag{2.38}$$

Environmental torques τ_e are the major source of external disturbances that influence dynamics of spacecraft. Gravity gradient torques acting on spacecraft due to variation in gravitational pull acting on distributed mass, they provide small but have significant contribution over the period of time. Due to center of pressure is not coincident with center of mass presence of very small air density at Low Earth Orbit, variation in aerodynamic forces distribution causes couple around center of mass. Magnetic materials and current flowing through electrical systems interacts with earths magnetic field causing contributes to external torque. Solar radiation pressure on spacecraft surface exposed to sun produces torque generally significant amount at Geostationary Orbits. These torques τ_e are known and can be modeled. On the other hand those which are not modeled are disturbance torques τ_d these are due to elastic modes, thruster misalignment, uncertainty in center of gravity and rotating parts.

The demand control torque \mathbf{u} is provided by actuators such as thrusters, momentum devices, magnetotorquer in order to reorient the spacecraft in desired states or to maintain its attitude based on mission requirements. Following section discuss the modeling of momentum deceives to produce \mathbf{u} . Bearing in mind that momentum exchange devices operate on the principle of distributing angular momentum among parts of system keeping total angular momentum conserved as a consequence \mathbf{u} is zero as long as any external saturation system is not present. Other torques τ_e and τ_d are disregarded for preliminary modeling. Accordingly equation becomes

$$\dot{\mathcal{H}} + \omega \times \mathcal{H} = 0\tag{2.39}$$

For the spacecraft equipped with CMG \mathcal{H} is sum of angular momentum of spacecraft platform \mathcal{H}_P and CMG \mathcal{H}_{CMG} . Whereas Inertia tensor of platform is

$$J_P = J_{P,0} + m \sum_{k=1}^n (||\vec{\mathbf{d}}_k|| \vec{\mathbf{I}} - \vec{\mathbf{d}}_k \vec{\mathbf{d}}_k) \quad (2.40)$$

Here, $J_{P,0}$ is inertia of platform without CMG and m is mass of k^{th} CMG whose center of mass is at distance $\vec{\mathbf{d}}_k$ from center of mass of entire system. The angular momentum of platform is

$$\mathcal{H}_P = J_P \cdot \omega \quad (2.41)$$

Total system angular momentum of spacecraft equipped with n number of SGCMGs is

$$\begin{aligned} \mathcal{H} &= \mathcal{H}_P + \sum_{k=1}^n \mathcal{H}_{CMG}^k \\ &= J_P \cdot \omega + \sum_{k=1}^n \left(J_{CMG}^k(\delta_k) \cdot \omega + J_{CMG}^g \dot{\delta}_k \hat{g}_k + J_W^s \Omega_k \hat{s}_k \right) \\ &= \left[J_P + \sum_{k=1}^n J_{CMG}^k(\delta_k) \right] \cdot \omega + J_{CMG}^g \sum_{k=1}^n \dot{\delta}_k \hat{g}_k + J_W^s \sum_{k=1}^n \Omega_k \hat{s}_k \end{aligned} \quad (2.42)$$

Time derivative of Equation 2.42 in platform frame \mathcal{H}_P is expressed as

$$\begin{aligned} \frac{d\mathcal{H}}{dt} &= \left[J_P + \sum_{k=1}^n J_{CMG}^k(\delta_k) \right] \cdot \dot{\omega} + \\ &\quad + \sum_{k=1}^n J_{CMG}^k(\delta_k) \cdot \omega + \\ &\quad + J_{CMG}^g \sum_{k=1}^n \ddot{\delta}_k \hat{g}_k + J_W^s \sum_{k=1}^n \dot{\Omega}_k \hat{s}_k + J_W^s \sum_{k=1}^n \Omega_k \dot{\delta}_k \hat{t}_k \end{aligned} \quad (2.43)$$

Substituting inertia derivative from Equation 2.31 we have

$$\begin{aligned} \dot{\mathcal{H}} &= \left[J_P + \sum_{k=1}^n J_{CMG}^k(\delta_k) \right] \cdot \dot{\omega} + \\ &\quad + \dot{\delta} \left(J_{CMG}^s - J_{CMG}^t \right) \sum_{k=1}^n (\hat{t}_k \hat{s}_k + \hat{s}_k \hat{t}_k) \cdot \omega + \\ &\quad + J_{CMG}^g \sum_{k=1}^n \ddot{\delta}_k \hat{g}_k + J_W^s \sum_{k=1}^n \dot{\Omega}_k \hat{s}_k + J_W^s \sum_{k=1}^n \Omega_k \dot{\delta}_k \hat{t}_k \end{aligned} \quad (2.44)$$

Cross multiplying Equation 2.42 by body angular velocity ω we get gyroscopic part

of Euler attitude equation

$$\begin{aligned}\omega \times \mathcal{H} = & \omega \times \left[J_P + \sum_{k=1}^n J_{CMG}^k(\delta_k) \right] \cdot \omega \\ & + J_{CMG}^g \omega \times \sum_{k=1}^n \dot{\delta}_k \hat{g}_k \\ & + J_W^s \omega \times \sum_{k=1}^n \Omega_k \hat{s}_k\end{aligned}\quad (2.45)$$

Substituting Equation 2.45 and Equation 2.45 in to Equation 2.39 we have Generalized attitude dynamics of a rigid satellite equipped with a cluster of n identical single gimbal VSCMGs

$$\begin{aligned}\dot{\mathcal{H}} + \omega \times \mathcal{H} = & \left[J_P + \sum_{k=1}^n J_{CMG}^k(\delta_k) \right] \cdot \dot{\omega} + \omega \times \left[J_P + \sum_{k=1}^n J_{CMG}^k(\delta_k) \right] \cdot \omega \\ & + \dot{\delta} \left(J_{CMG}^s - J_{CMG}^t \right) \sum_{k=1}^n (\hat{t}_k \hat{s}_k + \hat{s}_k \hat{t}_k) \cdot \omega \\ & + J_W^s \sum_{k=1}^n \dot{\Omega}_k \hat{s}_k + J_W^s \sum_{k=1}^n \Omega_k \dot{\delta}_k \hat{t}_k + J_W^s \omega \times \sum_{k=1}^n \Omega_k \hat{s}_k \\ & + J_{CMG}^g \sum_{k=1}^n \ddot{\delta}_k \hat{g}_k + J_{CMG}^g \omega \times \sum_{k=1}^n \dot{\delta}_k \hat{g}_k\end{aligned}\quad (2.46)$$

Dynamical equation Equation 2.46 is composition of contribution effects due to spacecraft angular velocity, gyroscopic effects the angular momentum of the entire system, variation of moment of inertia flywheel and gimbal velocities explained in Table 2.1 as reasoning of each terms contribution in entire system dynamics. A generalized dynamics for a satellite equipped with generic number of momentum exchange devices. We can see that this equation of motion comprises dynamics of reaction wheel, CMG and VSCMG

2.4.1 Reaction Wheel (RW)

If we freeze the gimbal, i.e. $\dot{\delta} = 0$ in Equation 2.46, resultant equation is satellite with reaction wheels simplified as

$$\dot{\mathcal{H}} + \omega \times \mathcal{H} = J \cdot \dot{\omega} + \omega \times J \cdot \omega + J_W^s \sum_{k=1}^n \dot{\Omega}_k \hat{s}_k + J_W^s \omega \times \sum_{k=1}^n \Omega_k \hat{s}_k = 0 \quad (2.47)$$

here $J = J_P + \sum_{k=1}^n J_{CMG}^k$ and derivative of J is zero. For regulation maneuver which conveys maintain fixed attitude counteracting the external disturbance making body rate $\omega = 0$ becomes.

$$J_W^s \sum_{k=1}^n \dot{\Omega}_k \hat{s}_k = \tau_d \quad (2.48)$$

Contribution rationale	Term
Variation of satellite angular velocity	$\left[J_P + \sum_{k=1}^n J_{CMG}^k(\delta_k) \right] \cdot \dot{\omega}$
Gyroscopic effects due to angular momentum of entire system	$\omega \times \left[J_P + \sum_{k=1}^n J_{CMG}^k(\delta_k) \right] \cdot \omega$
variation of the tensor of inertia	$\dot{\delta} \left(J_{CMG}^s - J_{CMG}^t \right) \sum_{k=1}^n (\hat{t}_k \hat{s}_k + \hat{s}_k \hat{t}_k) \cdot \omega$
variation reaction wheel velocities	$J_W^s \sum_{k=1}^n \dot{\Omega}_k \hat{s}_k + J_W^s \sum_{k=1}^n \Omega_k \dot{\delta}_k \hat{t}_k + J_W^s \omega \times \sum_{k=1}^n \Omega_k \hat{s}$
variation of gimbals velocities	$J_{CMG}^g \sum_{k=1}^n \ddot{\delta}_k \hat{g}_k + J_{CMG}^g \omega \times \sum_{k=1}^n \dot{\delta}_k \hat{g}_k$

Table 2.1. Explanation of individual terms in generalize equation of motion for satellite with generic number of VSCMG

Three reaction wheels with their spin axis mutually perpendicular are sufficient to counteract disturbance in any axis as long as saturation (maximum limit of angular momentum) does not occurs. Output torque is torque is proportional to rate of change of RW angular velocity and moment of inertia.

2.4.2 Control Moment Gyroscope (CMG)

Keeping angular velocity of RW Ω constant in Equation 2.46 we get attitude equation of a satellite equipped with control moment gyros as

$$\begin{aligned}
\dot{\mathcal{H}} + \omega \times \mathcal{H} = & \left[J_P + \sum_{k=1}^n J_{CMG}^k(\delta_k) \right] \cdot \dot{\omega} + \omega \times \left[J_P + \sum_{k=1}^n J_{CMG}^k(\delta_k) \right] \cdot \omega \\
& + \dot{\delta} \left(J_{CMG}^s - J_{CMG}^t \right) \sum_{k=1}^n (\hat{t}_k \hat{s}_k + \hat{s}_k \hat{t}_k) \cdot \omega \\
& + J_W^s \sum_{k=1}^n \Omega_k \dot{\delta}_k \hat{t}_k + J_W^s \omega \times \sum_{k=1}^n \Omega_k \hat{s}_k \\
& + J_{CMG}^g \sum_{k=1}^n \ddot{\delta}_k \hat{g}_k + J_{CMG}^g \omega \times \sum_{k=1}^n \dot{\delta}_k \hat{g}_k
\end{aligned} \tag{2.49}$$

For regulation maneuver disturbance torque can be counteracted as

$$J_W^s \sum_{k=1}^n \Omega_k \dot{\delta}_k \hat{t}_k + J_{CMG}^g \sum_{k=1}^n \ddot{\delta}_k \hat{g}_k = \tau_d \quad (2.50)$$

Torque produced through CMG is sum of gyroscopic couple due to variation in RW axis variation and acceleration of gimbal frame. Since moment of inertia of CMG and acceleration along gimbal axis is very small Equation 2.50 is simplified as

$$J_W^s \sum_{k=1}^n \Omega_k \dot{\delta}_k \hat{t}_k = \tau_d \quad (2.51)$$

Equation 2.51 is torque amplification due to gyroscopic effects of RW in body frame which is larger compared to RW. CMG torques are along transverse axis \hat{t} moving in \mathcal{F}_b and cannot produce orthogonal torque known as singularity.

$$\begin{aligned} \dot{\mathcal{H}} + \omega \times \mathcal{H} &= \left[J_P + \sum_{k=1}^n J_{CMG}^k(\delta_k) \right] \cdot \dot{\omega} + \omega \times \left[J_P + \sum_{k=1}^n J_{CMG}^k(\delta_k) \right] \cdot \omega \\ &+ \dot{\delta} \left(J_{CMG}^s - J_{CMG}^t \right) \sum_{k=1}^n (\hat{t}_k \hat{s}_k + \hat{s}_k \hat{t}_k) \cdot \omega \\ &+ J_W^s \sum_{k=1}^n \Omega_k \dot{\delta}_k \hat{t}_k + J_W^s \omega \times \sum_{k=1}^n \Omega_k \hat{s}_k \\ &+ J_{CMG}^g \sum_{k=1}^n \ddot{\delta}_k \hat{g}_k + J_{CMG}^g \omega \times \sum_{k=1}^n \dot{\delta}_k \hat{g}_k \end{aligned} \quad (2.52)$$

For regulation maneuver torque is evaluated as

$$J_W^s \sum_{k=1}^n \Omega_k \dot{\delta}_k \hat{t}_k + J_{CMG}^g \sum_{k=1}^n \ddot{\delta}_k \hat{g}_k = \tau_d \quad (2.53)$$

Simplified for small gimbal acceleration, regulation maneuver torque

$$J_W^s \sum_{k=1}^n \Omega_k \dot{\delta}_k \hat{t}_k = \tau_d \quad (2.54)$$

2.4.3 Variable Speed Control Moment Gyroscope (VSCMG)

Taking advantage from both reaction wheel and CMG for regulation maneuver to neutralize external disturbance τ_d we have

$$J_W^s \sum_{k=1}^n \dot{\Omega}_k \hat{s}_k + J_W^s \sum_{k=1}^n \Omega_k \dot{\delta}_k \hat{t}_k + J_{CMG}^g \sum_{k=1}^n \ddot{\delta}_k \hat{g}_k = \tau_d \quad (2.55)$$

is combination of RW and torque amplification due to CMG. Trivial presence in CMG can be escaped with RW and high torques are generated with gyroscopic forces. This thesis focuses on VSCMG with pyramid cluster. In order to simplify numerical computation direction vectors can be arranged in matrix form. For n-VSCMG, Unit

direction vectors of Gimbal, Spin and Transverse axis axis are evaluated based on their initial orientation

$$\begin{aligned}\mathcal{G}_g &= [\hat{g}_1 \cdots \hat{g}_n]_{3 \times n} = \mathcal{G}_{g_0} \\ \mathcal{G}_s &= [\hat{s}_1 \cdots \hat{s}_n]_{3 \times n} = \mathcal{G}_{s_0} \cos \delta + \mathcal{G}_{t_0} \sin \delta \\ \mathcal{G}_t &= [\hat{t}_1 \cdots \hat{t}_n]_{3 \times n} = -\mathcal{G}_{s_0} \sin \delta + \mathcal{G}_{t_0} \cos \delta\end{aligned}\quad (2.56)$$

This thesis is focused on pyramid cluster of four VSCMG units. Single Gimbal Control Moment Gyroscope basis vectors, initially orientation of each CMG spin and gimbal axis is shown in Figure 2.4 with gimbal axis skewed by angle β .

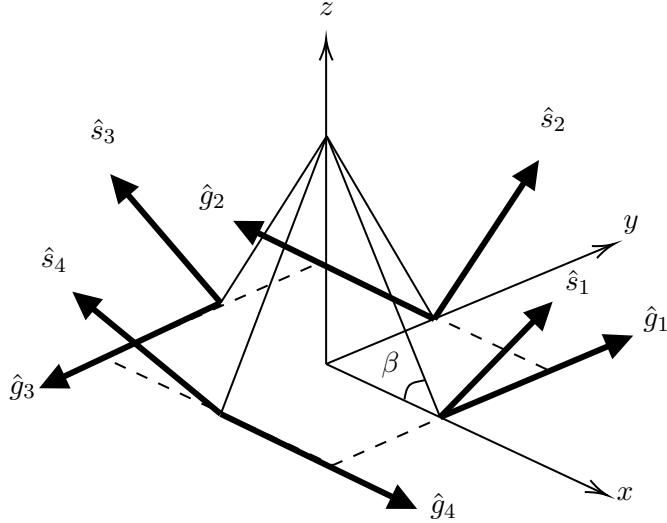


Figure 2.4. VSCMG Pyramid Cluster initial orientation

Evaluation of commutative gimbal, spin and transverse axis in represented as $\mathcal{G}_g, \mathcal{G}_s$ and \mathcal{G}_t respectively about body frame \mathcal{G}_b with basis vector b_1, b_2, b_3 alinged with x, y, z . Gimbae axis of all CMGs are oriented by Skew angle β is given as

$$\mathcal{G}_g = \begin{pmatrix} -\sin \beta & 0 & \sin \beta & 0 \\ 0 & \sin \beta & 0 & -\sin \beta \\ \cos \beta & \cos \beta & \cos \beta & \cos \beta \end{pmatrix} \quad (2.57)$$

$$\mathcal{G}_s = \begin{pmatrix} \cos \beta \cos \delta_1 & -\sin \delta_2 & -\cos \beta \cos \delta_3 & \sin \delta_4 \\ -\sin \delta_1 & -\cos \beta \cos \delta_2 & \sin \delta_3 & \cos \beta \cos \delta_4 \\ \sin \beta \cos \delta_1 & \sin \beta \cos \delta_2 & \sin \beta \cos \delta_3 & \sin \beta \cos \delta_4 \end{pmatrix} \quad (2.58)$$

$$\mathcal{G}_t = \begin{pmatrix} \cos \beta \sin \delta_1 & \cos \delta_2 & -\cos \beta \sin \delta_3 & -\cos \delta_4 \\ \cos \delta_1 & -\cos \beta \sin \delta_2 & -\cos \delta_3 & \cos \beta \sin \delta_4 \\ \sin \beta \sin \delta_1 & \sin \beta \sin \delta_2 & \sin \beta \sin \delta_3 & \sin \beta \sin \delta_4 \end{pmatrix} \quad (2.59)$$

Equation 2.46 can be written in the form of matrix for as

$$\begin{aligned}
\dot{\mathcal{H}} + \omega \times \mathcal{H} &= J\dot{\omega} + \omega^\times (J\omega + \mathcal{G}_t J_{CMG}^g \dot{\delta} + \mathcal{G}_s J_W^s \Omega) \\
&\quad + \mathcal{G}_t [\dot{\delta}]^d (J_{CMG}^s - J_{CMG}^t) \mathcal{G}_s^T + \mathcal{G}_s [\dot{\delta}]^d (J_{CMG}^s - J_{CMG}^t) \mathcal{G}_t^T \\
&\quad + \mathcal{G}_t J_W^s [\Omega]^d \dot{\delta} + \mathcal{G}_s J_W^s \dot{\Omega} + \mathcal{G}_s J_{CMG}^g \ddot{\delta} \\
&= 0
\end{aligned} \tag{2.60}$$

here cumulative moment of inertia including all SGCMG units and platform is denoted as J

$$J = J_P + \sum_{k=1}^n J_{CMG}^k(\gamma_k)$$

and $[\Omega]^d$ and $[\dot{\delta}]^d$ are diagonal matrices with elements being RW angular velocities and gimbal velocities.

Chapter 3

Singularity

Let us start taking analogy of robotic manipulator, Singularity is when robot loses it's degree of freedom at certain configuration or degeneration in mapping from Cartesian space to joint space. As in case when arm is at fully extended configuration when target is out of reach or at folded state when two joint axis are alined referred as internal or external singularity. When rank of mapping matrix which maps joint space to Cartesian space is is not full rank matrix then determinant of matrix is zero making it non invertible. Velocities are very large near singular states. Similarly, for control moment gyro there exist a direction about which torque can not be produced. Singularities are classified in two categories, internal and "external". If motion of gimbal angle does not produce torque in desired direction it is called "internal singularity", it occurs within saturation boundary, unlike "external singularity" in which angular momentum reaches maximum or saturation. Coming out of some singular states can be achieved by adapting null motion control law. Null motion control is changing angular momentum of spacecraft without producing torque on it. Gimbal lock is situation when all components of required torques are along singular direction. It is impassable if Null motion solution does not exist at the singularity.[10]

Let us recall total angular momentum of n-CMG configuration

$$\mathcal{H}_{CMG} = J_W^s \sum_{k=1}^n \Omega_k \hat{s}_k$$

and simplified torque is expressed as bellow with $C = J_W^s \mathcal{G}_t diag[\Omega_k]$ and $\mathcal{G}_t(\delta_k) = [\hat{t}_1 \dots \hat{t}_n]$

$$\begin{aligned} \tau &= J_W^s \sum_{k=1}^n \Omega_k \dot{\delta}_k \hat{t}_k \\ \tau &= C \dot{\delta} \end{aligned}$$

As long as C is full rank matrix τ in any arbitrary direction can be produced. Since $C_{3 \times n}$ is not necessarily square matrix, Gimbal rates can be obtained by taking pseudo inverse.

$$\dot{\delta}_{1 \times n} = C^T (CC^T)^{-1} \tau$$

If rank of $C \neq 3$ i.e. $\det C = 0$ then required $\dot{\delta}$ can not be evaluated. For n-CMG system in singular state, all \hat{t} are co planar and torque can not be produced normal to this plane. Let \hat{u} be the singular vector normal to plane where all \hat{t}_k are co-planar.

$$\hat{u} \cdot \hat{t}_k = 0$$

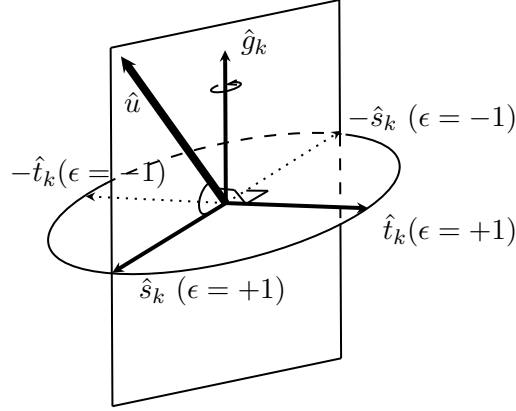


Figure 3.1. Vector representation at singular gimbal state

From Figure 3.1 we can see that flywheel vector \hat{s} has either positive or negative projection on singular vector \hat{u} , hence angular momentum along singular direction is

$$\mathcal{H}_u = \mathcal{H}_{CMG} \cdot \hat{u}$$

Component of angular momentum along singular direction has constant value based on \hat{u} that is Jacobian of \mathcal{H}_u with respect to δ is zero. Since \hat{u} cannot lie along \hat{g} we have $\hat{u} \cdot \hat{t}_k = 0$ for either positive or negative angular momentum component. For given \hat{u} there are 2^n singular states. Let sign of angular momentum component \mathcal{H}_u be $\epsilon_k = \text{sign}(s \cdot u)$ and $\hat{u} \neq \pm \hat{g}_k$. We have,

$$\hat{t}_k = \epsilon_k \frac{\hat{g}_k \times \hat{u}}{|\hat{g}_k \times \hat{u}|}, \quad (3.1)$$

$$\hat{s}_k = \hat{t}_k \times \hat{g}_k = \epsilon_k \frac{(\hat{g}_k \times \hat{u}) \times \hat{g}_k}{|\hat{g}_k \times \hat{u}|} \quad (3.2)$$

And angular momentum at singularity along singular direction is

$$\mathcal{H}_u = \sum_{k=1}^n \hat{s}_k = \sum_{k=1}^n \epsilon_k \frac{(\hat{g}_k \times \hat{u}) \times \hat{g}_k}{|\hat{g}_k \times \hat{u}|} \quad (3.3)$$

Projection of singular vector on total angular momentum can be evaluated for all unit singular vector $\hat{u} \in \mathbb{R}^3$ locus of all such points is singular surface and can be evaluated for given set of ϵ_k . [32]

A Matlab script has been developed in order to generate singular envelope of any CMG configuration with generic number of CMG units.

Results discussed here are considering Pyramid configuration of 4 CMG with skew angle $\beta = 54.73^\circ$ is selected for the fact that momentum distribution envelope is closed to spherical symmetry than other skew angles.[33] As we add more CMG the envelope becomes more closed to spherical but singularities singular direction increased on the order of $O(2^n)$.

Surface plots as shown in Figure 3.2 are generated for each ϵ_k enumerating vector \hat{u} as reasonable number of equidistant points on spherical surface. Figure 3.2a is external singular surface it is set of all singular momentum states equivalent to the maximum array angular momentum with $\epsilon = \{+++ +\}$ or $\epsilon = \{--- -\}$ we can notice there are 8 holes present, these are transition boundaries where singular vector is approaching towards gimbals and we have discontinuity at $\hat{u} = \hat{g}$. Number of circles present on external surface of skewed n-CMG configuration is $2n$ and are present at both ends of gimbal axis initial orientation and surface associated with each ϵ is connected with these circles. fig:sing_int1 is contribution of single gimbal with negative angular momentum of at least one wheel with respect to all other wheels. $\epsilon = \{-+++ +\}$. Notice the circular end caps similar to diverging trumpet are stretched along gimbal axis and their profile matches with holes of external surface. Internal surface has complex geometry and has both elliptical (null motion does not exist) and degenerate hyperbolic singularities (Null motion exist). Non-degenerate Hyperbolic Singularities are possible to avoid on the other hand degenerate hyperbolic singularities leads towards impassable elliptic singularity. Figure 3.2c shows all internal surfaces associated with each gimbal axis, generated by permutations of $\epsilon = \{-+++ +\}$. Figure 3.2d is all surfaces combined together, Figure 3.2e shows another perspective of all singular surfaces of CMG pyramid. Insight from the combination of surfaces is when angular momentum of all CMG units have same sign, holes in external surface denotes singularities are present in the direction of gimbal axis and torque can not be produced in volume encapsulated by conical geometry starting from center of sphere as apex and hole being base, on the other hand if one of CMG has opposite angular momentum it can provide torque in the direction of assumed cone.

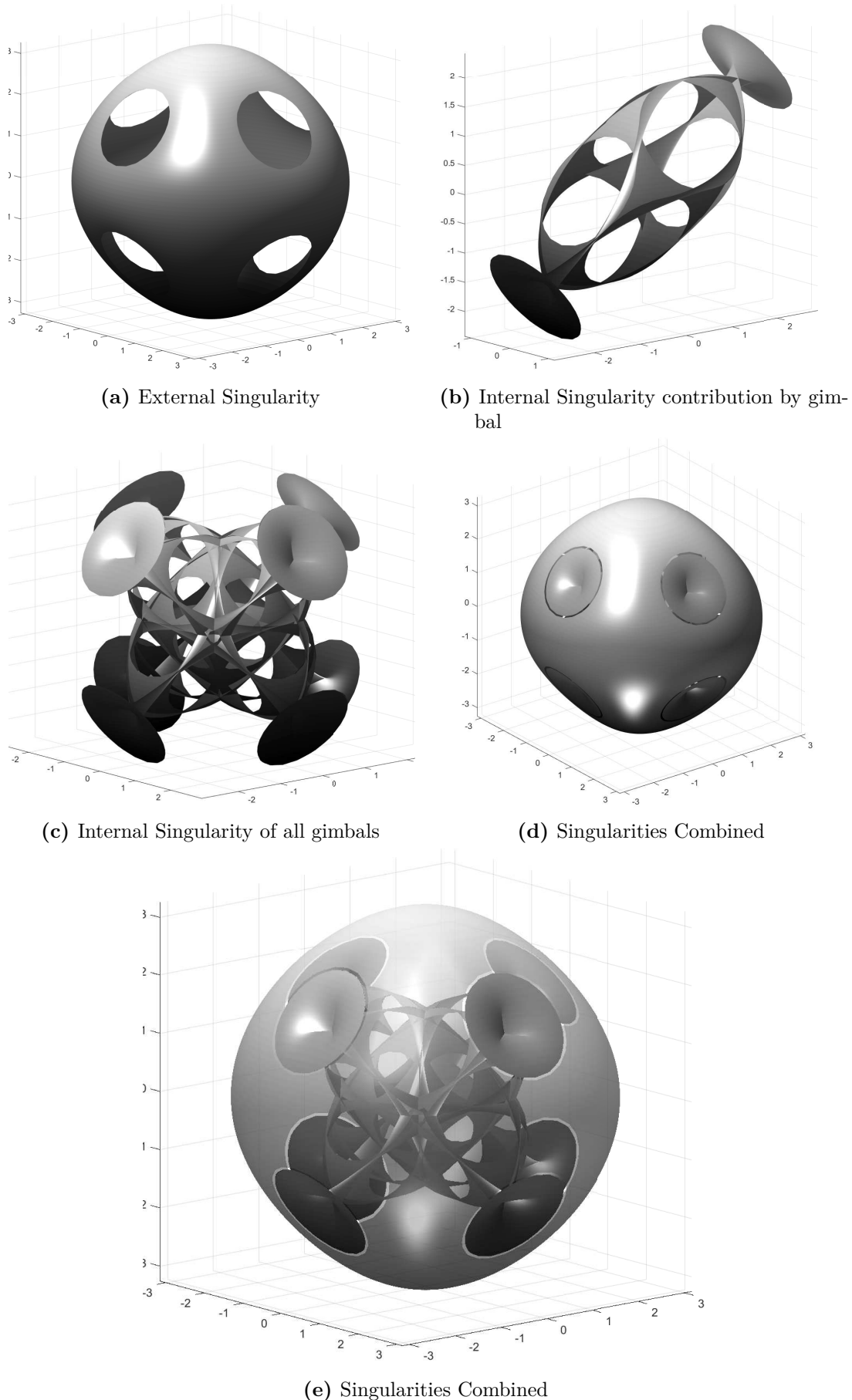


Figure 3.2. Singular surface of control moment gyro in pyramid configuration with skew angle $\beta = 54.73^\circ$

Chapter 4

Controller Design

In the interest of trajectory tracking and regulation maneuver during mission life cycle of spacecraft, suitable controller law is crucial choice ensuring accuracy and stability in presence of disturbances. Bearing in mind that the equation of motion for a spacecraft equipped with VSCMG units are highly complex and nonlinear in nature. It is clear that Equation 2.46 is time varying function of change in moment of inertia, gimbal angle, reaction wheel and gimbal angular velocity and acceleration. Nested control architecture is realized. As shown in Figure 4.1, Outer feedback loop deals with evaluation of torques τ_c based on state error with the intention of regulation or trajectory tracking. Furthermore, inner control loop to produce required torque from individual actuators. RW generates torque by accelerating flywheel whereas in case CMG, torque is proportional to angular momentum of RW and gimbal velocity. The idea is to find out particular combination of gimbal velocities and RW accelerations in order to produce required torque demanded by outer loop with strong emphasis on avoiding singularity.

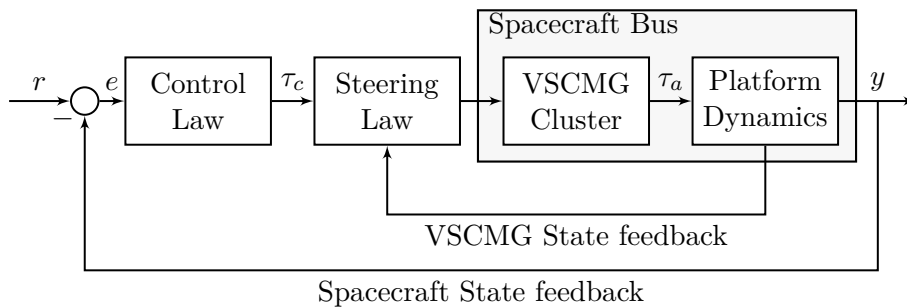


Figure 4.1. VSCMG Spacecraft Attitude Control Architecture

4.1 Lyapunov Stability Method

Lyapunov stability is widely used methods for continuous time nonlinear systems, two methods proposed by Aleksandr Lyapunov in 1892 are indirect methods [34] in which behavior of linearized system about equilibrium point is examined, whereas direct method to verify stability of nonlinear system by inspecting evaluation of

"lyapunov function" an energy like positive definite function composed of system states. If the carefully constructed scalar function decreases over time, the system under study is proved to be stable. It is possible to realize controller which dissipates selected scalar function.

Consider continuous, time-invariant nonlinear system with state x and control input u .

$$\dot{x} = f(x, u)$$

The idea behind Lyapunov direct method is crafting positive definite scalar function $\mathcal{V}(x)$ and substituting $u = u(x)$ making it closed loop dynamical system such a way that with derived controller the derivative $\dot{\mathcal{V}}(x)$ becomes negative. Stability critaria is

$$\begin{aligned}\mathcal{V}(x) &> 0 \\ \dot{\mathcal{V}}(x) &< 0 \\ \mathcal{V}(x) &\rightarrow \infty, \quad \|x\| \rightarrow \infty\end{aligned}\tag{4.1}$$

If selected scalar function with derived controller satisfies Equation 4.1 then system is said to be asymptotically stable.

4.2 Model based Controller Design

A control law must be designed in such a way that it guarantees asymptotic stability of states, by shifting global equilibrium to desired state. For external feedback control loop let \mathcal{F}_d be desired body fixed rotating frame and spacecraft current state body fixed reference frame \mathcal{F}_b described with respect to inertial frame \mathcal{F}_i . As described in chapter 2 let ω be the angular velocity of \mathcal{F}_b and $q = q_0 + q_v$ be current attitude of \mathcal{F}_b . Lets recall rotation matrix from \mathcal{F}_i to \mathcal{F}_b

$$\mathbf{R}(\mathbf{q}) = \left(q_0^2 - \mathbf{q}_v^T \mathbf{q}_v \right) \mathbf{I}_{3 \times 3} + 2\mathbf{q}_v \mathbf{q}_v^T + 2q_0 \mathbf{q}^\times\tag{4.2}$$

Similarly, $q_d = q_{d,0} + q_{d,v}$ the attitude quaternion of \mathcal{F}_d and ${}^i\omega_d$ be angular velocity of desired reference frame. The rotation matrix which transforms \mathcal{F}_i to \mathcal{F}_b is

$$\mathbf{R}(\mathbf{q}_d) = \left(q_{0,d}^2 - \mathbf{q}_{v,d}^T \mathbf{q}_{v,d} \right) \mathbf{I}_{3 \times 3} + 2\mathbf{q}_{v,d} \mathbf{q}_{v,d}^T + 2q_{0,d} \mathbf{q}_d^\times\tag{4.3}$$

Attitude of \mathcal{F}_b described with respect to \mathcal{F}_b can be considered as deviation in tracking, hence with tracking error quaternion $q_e = q_{e,0} + q_{e,v}$ rotation matrix among body and desired frame is expressed as

$$\mathbf{R}(\mathbf{q}_e) = \left(q_{0,e}^2 - \mathbf{q}_{e,d}^T \mathbf{q}_{e,d} \right) \mathbf{I}_{3 \times 3} + 2\mathbf{q}_{e,d} \mathbf{q}_{e,d}^T + 2q_{0,e} \mathbf{q}_e^\times\tag{4.4}$$

recalling from chap error quaternion representation in vectorial and eigen axis from

$$\begin{pmatrix} \mathbf{q}_{e,0} \\ q_{v,e} \end{pmatrix} = \begin{pmatrix} \cos(\varepsilon/2) \\ \hat{\mathbf{e}} \sin(\varepsilon/2) \end{pmatrix} = \begin{pmatrix} q_0 q_{d,0} + \mathbf{q}^T \mathbf{q}_d \\ -q_0 q_{d,v} + q_{d,0} q_v - q_v \times q_{d,v} \end{pmatrix}\tag{4.5}$$

When current attitude and desired attitude are same, angular displacement is ε becomes zero making error quaternion

$$\mathbf{q}_e = \begin{pmatrix} q_{e,0} \\ q_{v,e} \end{pmatrix} = \begin{pmatrix} 1 \\ \mathbf{0} \end{pmatrix} \quad (4.6)$$

Angular velocity tracking error ω_e is angular velocity of body frame with respect to desired frame \mathcal{F}_d can be expressed in \mathcal{F}_b as

$$\omega_e = \omega - \mathbf{R}(\mathbf{q}_e)^i \omega_d = \omega - \omega_d$$

here ω_d is angular velocity of desired frame with respect to current body frame. The quaternion kinematics for error tracking expressed in body frame

$$\begin{aligned} \dot{\mathbf{q}}_e &= \frac{1}{2} \begin{bmatrix} -\omega_e \cdot q_{e,v} \\ q_{e,0}\omega_e - q_{e,v}^\times \end{bmatrix} \\ \mathbf{q}_e &= \frac{1}{2} \begin{bmatrix} 0 & -\omega_e \\ \omega_e & -\omega_e^\times \end{bmatrix} \begin{bmatrix} q_{e,0} \\ q_{e,v} \end{bmatrix} \end{aligned} \quad (4.7)$$

Similar approach will be used to derive “Reward Function” for training Neural Network policy with Reinforcement Learning (RL) methods.

4.2.1 The Lyapunov Candidate Function

Based on previously developed analogy of quaternion tracking error and angular velocity tracking error, for shifted target equilibrium candidate Lyapunov function is selected as [35]

$$\mathcal{V} = \frac{1}{2} \omega_e^T \mathbf{K}^{-1} J \omega_e + q_{e,v} q_{e,v}^T + (q_{e,0} - 1)^2 \quad (4.8)$$

Here, J is inertia tensor of complete spacecraft and function and $\mathbf{K}_{3 \times 3}^{-1}$ is positive definite matrix. consequently \mathcal{V} guarantees to be positive definite since all the terms in Equation 4.8 are in quadratic form. From Equation 4.2 we can deduce that that Candidate becomes zero when velocity tracking error and quaternion error becomes zero. With unit norm quaternion property

$$q_{e,0}^2 + q_{e,v} q_{e,v}^T = 1 \quad (4.9)$$

$$(q_{e,0} - 1)^2 + q_{e,v} q_{e,v}^T = (q_{e,0} - 1)^2 + 1 - q_{e,0}^2 = 2(1 - q_{e,0}) \quad (4.10)$$

Using above relation Lyapunov Candidate function is reduced to

$$\mathcal{V} = \frac{1}{2} \omega_e^T \mathbf{K}^{-1} J \omega_e + 2(1 - q_{e,0}) \quad (4.11)$$

Another popular candidate function selected for regulation is purely based on kinetic energy of spacecraft which is [10]

$$\mathcal{V} = \frac{1}{2} \omega^T J \omega \quad (4.12)$$

4.2.2 Stability Analysis

In order to evaluate stability of system, Candidate function derivative $\dot{\mathcal{V}}$ should be negative which guarantees asymptotic stability of system, in this case chosen function is

$$\mathcal{V} = \frac{1}{2}\omega_e^T \mathbf{K}_q^{-1} J \omega_e + 2(1 - q_{e,0}) \quad (4.13)$$

taking time derivative of candidate function

$$\dot{\mathcal{V}} = \frac{1}{2}\omega_e^T \mathbf{K}_q^{-1} \dot{J} \omega_e + \omega_e^T \mathbf{K}_q^{-1} J \dot{\omega}_e - 2\dot{q}_{e,0} \quad (4.14)$$

Substituting derivative of inertia tensor in above expression we have

$$\begin{aligned} \dot{\mathcal{V}} = & \frac{1}{2} \left(J_{CMG}^s - J_{CMG}^t \right) \omega_e^T \mathbf{K}_q^{-1} \sum_{k=1}^n \dot{\delta}_k [\hat{t}_k \hat{s}_k + \hat{s}_k \hat{t}_k] \cdot \omega_e \\ & - \left(J_{CMG}^s - J_{CMG}^t \right) \omega_e^T \mathbf{K}_q^{-1} \sum_{k=1}^n \dot{\delta}_k [\hat{t}_k \hat{s}_k + \hat{s}_k \hat{t}_k] \cdot \omega \\ & - \omega_e^T \mathbf{K}_q^{-1} [\omega \times J \omega] \\ & - \omega_e^T \mathbf{K}_q^{-1} \left[J_W^s \sum_{k=1}^n \dot{\Omega}_k \hat{s}_k + J_W^s \sum_{k=1}^n \Omega_k \dot{\delta}_k \hat{t}_k + J_W^s \omega \times \sum_{k=1}^n \Omega_k \hat{s}_k \right] \\ & - \omega_e^T \mathbf{K}_q^{-1} \left[J_{CMG}^g \sum_{k=1}^n \ddot{\delta}_k \hat{g}_k + J_{CMG}^g \omega \times \sum_{k=1}^n \dot{\delta}_k \hat{g}_k \right] \\ & - \omega_e^T \mathbf{K}_q^{-1} J \dot{\omega}_d + \omega_e q_e^T \end{aligned} \quad (4.15)$$

In order to ensure $\dot{\mathcal{V}} < 0$, from expression above taking ω_e common and introducing new positive definite matrix \mathbf{K}_w such a way that Equation 4.15 becomes

$$\dot{\mathcal{V}} = -\omega_e^T \mathbf{K}_q^{-1} \mathbf{K}_w \omega_e \quad (4.16)$$

$$\begin{aligned} -\mathbf{K}_q^{-1} \mathbf{K}_w \omega_e = & -\frac{1}{2} \left(J_{CMG}^s - J_{CMG}^t \right) \mathbf{K}_q^{-1} \sum_{k=1}^n \dot{\delta}_k [\hat{t}_k \hat{s}_k + \hat{s}_k \hat{t}_k] \cdot (\omega + \omega_d) \\ & - \mathbf{K}_q^{-1} [\omega \times J \omega] \\ & - \mathbf{K}_q^{-1} \left[J_W^s \sum_{k=1}^n \dot{\Omega}_k \hat{s}_k + J_W^s \sum_{k=1}^n \Omega_k \dot{\delta}_k \hat{t}_k + J_W^s \omega \times \sum_{k=1}^n \Omega_k \hat{s}_k \right] \\ & - \mathbf{K}_q^{-1} \left[J_{CMG}^g \sum_{k=1}^n \ddot{\delta}_k \hat{g}_k + J_{CMG}^g \omega \times \sum_{k=1}^n \dot{\delta}_k \hat{g}_k \right] \\ & - \mathbf{K}_q^{-1} J \dot{\omega}_d + q_e \end{aligned} \quad (4.17)$$

Since \mathbf{K}_q^{-1} appears in both sides, Equation 4.17 can be expressed as

$$\begin{aligned}
 & \frac{1}{2} \left(J_{CMG}^s - J_{CMG}^t \right) \sum_{k=1}^n \dot{\delta}_k [\hat{t}_k \hat{s}_k + \hat{s}_k \hat{t}_k] \cdot (\omega + \omega_d) \\
 & + J_W^s \sum_{k=1}^n \dot{\Omega}_k \hat{s}_k + J_W^s \sum_{k=1}^n \Omega_k \dot{\delta}_k \hat{t}_k \\
 & + J_{CMG}^g \sum_{k=1}^n \ddot{\delta}_k \hat{g}_k + J_{CMG}^g \omega \times \sum_{k=1}^n \dot{\delta}_k \hat{g}_k \\
 & = \mathbf{K}_w \omega_e + \mathbf{K}_q q_e - J \dot{\omega}_d - \omega \times \left[J \omega + J_W^s \sum_{k=1}^n \Omega_k \hat{s}_k \right]
 \end{aligned} \tag{4.18}$$

Substituting Equation 4.18 in Equation 2.46 complete nonlinear dynamical equation

$$J \dot{\omega}_e + J \dot{\omega}_e = -\mathbf{K}_w \omega_e - \mathbf{K}_q q_e \tag{4.19}$$

Equation 4.19 is error tracking control of VSCMG, we can see it resembles proportional derivative control, \mathbf{K}_q being proportional gain while \mathbf{K}_w can be considered as derivative gain matrix. In terms of control torque u expression is

$$u = -\mathbf{K}_w \omega_e - \mathbf{K}_q q_e \tag{4.20}$$

Expression assures asymptotic stability of ω_e , In order to make sure Equation 4.8 satisfies Lyapunov criterion, and guarantying asymptotic stability of all the states as we know $\omega_{e,\infty} \rightarrow 0$ thus $\dot{\omega}_{e,\infty} \rightarrow 0$ we can demonstrate the quaternion vector components tends to zero and scalar becomes 1 thus making

$$\mathbf{K}_q q_{e,\infty} = 0 \tag{4.21}$$

From argument above we can ensure that $q_{e,\infty}$ tends to zero thus Equation 4.8 satisfies Lyapunov criterion for all states. Now, rearranging control variables in order to have control torque that can be generated internally all momentum exchange devices is expressed as

$$\begin{aligned}
 u &= \frac{1}{2} \left(J_{CMG}^s - J_{CMG}^t \right) \sum_{k=1}^n \dot{\delta}_k [\hat{t}_k \hat{s}_k + \hat{s}_k \hat{t}_k] \cdot (\omega + \omega_d) \\
 &+ J_W^s \sum_{k=1}^n \dot{\Omega}_k \hat{s}_k + J_W^s \sum_{k=1}^n \Omega_k \dot{\delta}_k \hat{t}_k \\
 &+ J_{CMG}^g \sum_{k=1}^n \ddot{\delta}_k \hat{g}_k + J_{CMG}^g \omega \times \sum_{k=1}^n \dot{\delta}_k \hat{g}_k
 \end{aligned}$$

Consequently. demand torque required to make $\omega_{e,\infty}$ and $q_{e,\infty}$ tends to zero is

$$u = \mathbf{K}_w \omega_e + \mathbf{K}_q q_e - J \dot{\omega}_d - \omega \times \left[J \omega + J_W^s \sum_{k=1}^n \Omega_k \hat{s}_k \right] \tag{4.22}$$

Making close loop dynamics of Spacecraft with VSCMG suitable for both trajectory tracking and regulation becomes

$$J \dot{\omega} + \frac{1}{2} J \dot{\omega}_e + \omega \times \left[J \omega + J_W^s \sum_{k=1}^n \Omega_k \hat{s}_k \right] = -u \tag{4.23}$$

4.3 Steering Law

In order to generate torque required to reach desired state, appropriate signal must be provided to momentum exchange devices present in spacecraft. VSCMG produce torque using reaction wheel angular acceleration $\dot{\Omega}$, gimbal velocity $\dot{\delta}$ and gimbal acceleration $\ddot{\delta}$. In the interest of evaluating precise values taking into consideration for particular arrangement of generic number of VSCMG cluster.

Demand torque expression written in terms of momentum exchange devices given in equation can be expressed in matrix form for generic number of VSCMG units as

$$u = B\ddot{\delta} + C\dot{\delta} + D\dot{\Omega} \quad (4.24)$$

here coefficient matrices $B_{3 \times n}$, $C_{3 \times n}$ and $D_{3 \times n}$ are composed of 3 rows and n columns as

$$\begin{aligned} B &= J_{CMG}^g \sum_{k=1}^n \hat{g}_k \\ B &= J_{CMG}^g \mathcal{G}_g \end{aligned} \quad (4.25)$$

$$\begin{aligned} C &= \sum_{k=1}^n \left[J_W^s \Omega_k \hat{t}_k + \frac{1}{2} (J_{CMG}^s - J_{CMG}^t) [\hat{t}_k \hat{s}_k + \hat{s}_k \hat{t}_k] \cdot (\omega + \omega_d) + J_{CMG}^g \omega \times \hat{g}_k \right] \\ C &= J_W^s [\Omega]^d \mathcal{G}_t + \frac{1}{2} (J_{CMG}^s - J_{CMG}^t) \mathcal{G}_{stw^+} + J_{CMG}^g \omega \times \mathcal{G}_g \end{aligned} \quad (4.26)$$

$$\begin{aligned} D &= \sum_{k=1}^n J_W^s \hat{s}_k \dot{\Omega}_k \\ D &= J_W^s \mathcal{G}_s \end{aligned} \quad (4.27)$$

where, direction cosines of gimbal spin and transverse axis are written as

$$\begin{aligned} \mathcal{G}_g &= \begin{bmatrix} | & | & | \\ \hat{g}_1 & \hat{g}_2 & \dots & \hat{g}_n \\ | & | & & | \end{bmatrix}_{3 \times n} & \mathcal{G}_t &= \begin{bmatrix} | & | & | \\ \hat{t}_1 & \hat{t}_2 & \dots & \hat{t}_n \\ | & | & & | \end{bmatrix}_{3 \times n} & \mathcal{G}_s &= \begin{bmatrix} | & | & | \\ \hat{s}_1 & \hat{s}_2 & \dots & \hat{s}_n \\ | & | & & | \end{bmatrix}_{3 \times n} \\ \mathcal{G}_{stw^+} &= \begin{bmatrix} | & | & | \\ [\hat{t}_1 \hat{s}_1 + \hat{s}_1 \hat{t}_1] \cdot (\omega + \omega_d) & \dots & [\hat{t}_1 \hat{s}_1 + \hat{s}_1 \hat{t}_1] \cdot (\omega + \omega_d) \\ | & & | \end{bmatrix}_{3 \times n} \end{aligned}$$

Diagonal matrix is represented by brackets with superscript $[]^d$ as

$$[\Omega]^d = \begin{bmatrix} \Omega_1 & & & 0 \\ & \Omega_2 & & \\ & & \ddots & \\ 0 & & & \Omega_n \end{bmatrix}_{3 \times n}$$

Neglecting smaller terms in Equation 4.26, C becomes

$$C = J_W^s [\Omega]^d \mathcal{G}_t \quad (4.28)$$

And for momentum wheel portion, keeping constant gimbal angle at all times makes D constant, thus Equation 4.24 is simplified as

$$\begin{aligned} u &= \sum_{k=1}^n J_W^s \hat{s}_k \dot{\Omega}_k \\ u &= D \dot{\Omega}_k \end{aligned} \quad (4.29)$$

Equation 4.29 is considering only reaction wheel based control torques. Whereas keeping RW angular velocity $\dot{\Omega}$ constant and neglecting very small gimbal acceleration term, CMG based control is achieved as

$$u = C[\dot{\delta}]^d \quad (4.30)$$

4.3.1 Reaction Wheel Optimization

As seen earlier sections, VSCMG clusters gives ability to produced torques by only using Reaction Wheels as torque producing unit, and required torques can be realized by

$$u = D \dot{\Omega} \quad (4.31)$$

Since number of equations 3 and are more than number of unknown variables due to the fact that more that there will be more than three reaction wheels present for the purpose redundancy. The solution has dimension $N(D) = m - n$ degrees of freedom. Where number of equations $n = 3$ and number of unknown variables $m > 3$. There is no trivial solution for such problem and required solution can only be found with optimization criteria. In this case minimum norm criteria is used for RW acceleration. Let us define Lagrangian \mathcal{L} and Lagrangian

$$\mathcal{L}(\dot{\Omega}) = ||\dot{\Omega}|| = \dot{\Omega}^T \dot{\Omega} \quad (4.32)$$

In order to minimize $\min ||\dot{\Omega}||$ for $u = D \dot{\Omega}$ by introducing Lagrangian multiplier λ

$$f = \dot{\Omega}^T \dot{\Omega} + \lambda^T (u - D \dot{\Omega}) \quad (4.33)$$

Conditions for minimum norm solutions is partial differentiation above function with respect to $\dot{\Omega}$ and λ must be equal to zero

$$\begin{aligned} \frac{\partial f}{\partial \dot{\Omega}} &= 0 \\ \frac{\partial f}{\partial \lambda} &= 0 \end{aligned} \quad (4.34)$$

Thus from Equation 4.33 and Equation 4.34 optimum Lagrangian multiplier λ^* is

$$\dot{\Omega}^* = \frac{1}{2} D^T \lambda^* \quad (4.35)$$

$$\begin{aligned} u &= D \dot{\Omega}^* \\ u &= \frac{1}{2} D D^T \lambda^* \end{aligned} \quad (4.36)$$

Matrix DD^T is full rank making it invertible thus equation for optimum acceleration $\dot{\Omega}$ for u is

$$\dot{\Omega}^* = D^T (DD^T)^{-1} u \quad (4.37)$$

$$\dot{\Omega}^* = D^\dagger u \quad (4.38)$$

here $D^\dagger = D^T (DD^T)^{-1}$ is pseudo inverse of matrix D commonly used in inverse kinematics of robotics manipulator. Although Equation 4.38 guarantees optimum solution, but does not address the saturation problem involved with RW. Since we know that $\ker D \neq 0$, Extra degree of freedom gives ability to employ reaction null method which basically distributing momentum among flywheels without producing torque. As a result angular momentum of RWs can be minimized with taking minimum norm as

$$\mathcal{L}(\mathcal{H}) = \mathcal{H}\mathcal{H}^T \quad (4.39)$$

and thus angular momentum can be minimized for required \mathcal{H}_r by optimum angular momentum expression

$$\mathcal{H}^* = S^T (SS^T)^{-1} \mathcal{H}_r = S^\dagger \mathcal{H}_r \quad (4.40)$$

Equation above gives optimum steering of MW for desaturation, Equation 4.38 gives power optimized RW control law. In order to minimize both power consumption with desaturation, required command torque is written with introducing vector x such that $Sx = 0$ that is $x \in \ker\{S\}$

$$u = S [J_W^s \dot{\Omega}^* + \mathbf{x}] \quad (4.41)$$

Optimum angular momentum by introducing Lagrange multiplier λ is

$$\mathcal{H}^* = \frac{1}{2} S^T \lambda^* \quad (4.42)$$

Let us rewrite the expression by Singular Value Decomposition (SVD) of S as $S = \mathbf{U}\Sigma\mathbf{V}^T$, where left singular vector $\mathbf{U}\mathbf{U}^T = \mathbf{I}_{3\times 3}$ and right singular vector $\mathbf{V}\mathbf{V}^T = \mathbf{I}_{4\times 4}$ and $\Sigma_{3\times 4}$ is rectangular diagonal matrix with non negative real numbers on diagonal σ_i are singular values

$$\Sigma = \begin{pmatrix} \sigma_1 & 0 & 0 & 0 \\ 0 & \sigma_2 & 0 & 0 \\ 0 & 0 & \sigma_3 & 0 \end{pmatrix} \quad (4.43)$$

applying SVD to S and multiplying by \mathbf{V}^T Equation 4.41 becomes

$$\begin{aligned} \mathbf{V}^T \mathcal{H}^* &= \frac{1}{2} \mathbf{V}^T \mathbf{V} \Sigma^T \mathbf{U}^T \lambda^* \\ &= \frac{1}{2} \Sigma^T \mathbf{U}^T \lambda^* \\ &= \Sigma^T \mathbf{U}^T \bar{\lambda}^* \end{aligned} \quad (4.44)$$

Forth column \mathbf{v}_4 of Equation 4.42 is null vector thus

$$\gamma = \mathbf{v}_4^T \mathcal{H}^* = 0 \quad (4.45)$$

Equation 4.45 denotes that if angular momentum is optimum γ becomes zero thus can be considered as optimality index for angular momentum distribution. Similarly, $\mathbf{v}_4^T \dot{\Omega}$ becomes zero only if $\dot{\Omega}$ is optimal. Introducing optimality index, torque required is

$$u = S\tau = S [J_W^s \dot{\Omega} - \gamma \mathbf{k}] \quad (4.46)$$

multiplying Equation 4.46 by \mathbf{v}_4^T and rate of change of angular momentum $\dot{\mathcal{H}} = \tau$

$$\begin{aligned} \mathbf{v}_4^T \dot{\mathcal{H}} &= J_W^s \dot{\Omega}^* - \gamma \mathbf{v}_4^T \mathbf{k} \\ &= -\gamma \mathbf{v}_4^T \mathbf{k} \end{aligned}$$

we can deduce that

$$\dot{\gamma} = -\mathbf{v}_4^T \mathbf{k} \gamma \quad (4.47)$$

$\mathbf{k} = \beta \mathbf{v}_4$ for nonzero positive β , consequently $\mathbf{v}_4^T \mathbf{v}_4 = 1$ we get

$$\dot{\gamma} + \beta \gamma = 0 \quad (4.48)$$

as a result γ tends to zero distributing angular momentum in optimal way. Again using SVD and taking $S\mathbf{k} = \beta S\mathbf{v}_4$ Equation 4.46 can be written as

$$\begin{aligned} \beta S\mathbf{v}_4 &= \beta \mathbf{U} \boldsymbol{\Sigma} \mathbf{V}^T \mathbf{v}_4 \\ &= \beta \mathbf{U} \boldsymbol{\Sigma} \begin{pmatrix} 0 \\ 0 \\ 0 \\ 1 \end{pmatrix} \\ &= 0 \end{aligned} \quad (4.49)$$

From above expression, it is clear that \mathbf{v}_4 belongs to null space of matrix S , thus does not contribute to produce output torque but useful to redistribute angular momentum. Finally, torque produced by Reaction Wheel is

$$u = J_W^s \dot{\Omega} - \beta \gamma \mathbf{v}_4 \quad (4.50)$$

4.3.2 Acceleration-Based Gimbal Tracking

Since signal given to the electric motors are superposed to be proportional to acceleration another feedback loop is needed for gimbal velocity $\dot{\delta}$. Once required gimbal velocity $\dot{\delta}_r$ is determined by steering law then gimbal acceleration can approximated to

$$\ddot{\delta} = \mathbf{K}_g(\dot{\delta} - \dot{\delta}_r) + \ddot{\delta} \approx \mathbf{K}_g(\dot{\delta} + \dot{\delta}_r) \quad (4.51)$$

by selecting appropriate gain matrix \mathbf{K}_g tracking $\dot{\delta}_r$ is possible and $\dot{\delta} \rightarrow \dot{\delta}_r$ as $t \rightarrow \infty$.

4.3.3 Velocity Based VSCMGs Steering Law

As discussed earlier, minimum three Reaction Wheels arranged in each body axis are capable of producing torque in any direction but amplitude is small. On the other hand CMGs gives ability to amplify the torque but also come with singularity problem, i.e. when all transverse axis are in same plane and demand torque is normal to this plane. Combining ability of both CMG and RW we get Variable Speed Control moment gyroscope in which ability to produce torque with RW can be used to escape or avoid singular states. Consequently feedback law for VSCMG is

$$\tau_r = B\ddot{\delta} + C\dot{\delta} + D\dot{\Omega} \quad (4.52)$$

In this case B is very small thus can be neglected, otherwise $\ddot{\delta}$ becomes very large an unseasonable to produce demand torque, thus VSCMG equation becomes

$$\tau_r = C\dot{\delta} + D\dot{\Omega} \quad (4.53)$$

This thesis is focused on pyramid cluster of VSCMG units, let us define variables as

$$x = \begin{pmatrix} \dot{\delta} \\ \dot{\Omega} \end{pmatrix} \quad (4.54)$$

$$\mathbf{Q} = \begin{bmatrix} C & D \end{bmatrix} \quad (4.55)$$

thus Equation 4.53 becomes

$$\tau_r = \mathbf{Q}x \quad (4.56)$$

we know that C tends singular as its determinant reaches zero, thus to have some sense of singularity, can be measured as

$$m_w = \sqrt{\det CC^T} \quad (4.57)$$

in Equation 4.56 we have more unknowns than equations, hence problem can be solved with optimization method, let weighted Lagrangian function be

$$\mathcal{L}(x) = x^T W^{-1} x \quad (4.58)$$

here weight matrix is diagonal matrix with positive scalar weights α_i are associated with gimbal rates, and $\beta_i = k_0 e^{-k_1 m_w}$ are associated with reaction wheel accelerations, as m_w becomes larger more weight is given to gimbal velocities, contrary to this more RWs are weighted more as m_w tends to zero.

scalar quantities k_0 and k_1 are chosen carefully for desired performance. The optimization problem formulated as

$$\begin{cases} \min\{\mathcal{L}(x)\} \\ Qx = u \end{cases} \quad (4.60)$$

Using Lagrange multiplier let the function be

$$f = x^T W^{-1} x + \lambda^T (u - Qx) \quad (4.61)$$

Conditions to solve above mentioned optimization functions are

$$\begin{cases} \frac{\partial f}{\partial x} = 0 \\ \frac{\partial f}{\partial \lambda} = 0 \end{cases} \quad (4.62)$$

thus to have optimum acceleration for required torque relation becomes

$$x^* = \frac{1}{2} W Q^T \lambda^* \quad (4.63)$$

$$u = \frac{1}{2} Q W Q^T \lambda^* \quad (4.64)$$

$Q W Q^T$ guarantees to be invertible hence we have optimal acceleration vector in the form of

$$x^* = W Q^T (Q W Q^T)^{-1} u \quad (4.65)$$

$$\begin{pmatrix} \dot{\delta} \\ \dot{\Omega} \end{pmatrix}^* = W Q^T (Q W Q^T)^{-1} u \quad (4.66)$$

It is clear that scalar component β_i of weight matrix W_i depends on singularity measure m_c of CMG. When CMG are not singular m_c is large making β_i very small but in case of CMG singularity beta becomes larger intern making smooth transition to reaction wheel based control. Although this steering law works well in order to avoid CMG singularities, we also need to introduce m_w the singularity measure for Reaction Wheels. To consider both RW and CMG singularities weights are determined as

$$\begin{aligned} \beta &= k_0 \exp(-k_1 m_c / m_w) \\ m_w &= \sqrt{\det D D^T} \end{aligned} \quad (4.67)$$

where m_w is singularity measure of reaction wheel cluster. These weights takes care of both CMG and RW singularities. Although there are certain conditions where both m_w and m_c are very small, this may occur when wheel spin rate is zero for all RWs and CMGs are in singular state. To deal with this issue let us take Singular Value Decomposition of $Q = \mathbf{U} \Sigma \mathbf{V}^T$

$$\begin{aligned} \Sigma &= \begin{pmatrix} \sigma_1 & 0 & 0 & 0 & 0 & 0 & 0 & 0 \\ 0 & \sigma_2 & 0 & 0 & 0 & 0 & 0 & 0 \\ 0 & 0 & \sigma_3 & 0 & 0 & 0 & 0 & 0 \end{pmatrix}_{3 \times 8} \\ \mathbf{U} &= (u_1 \ u_2 \ u_3)_{3 \times 3} \\ \mathbf{V} &= (v_1 \ v_2 \ v_3 \ v_4 \ v_5 \ v_6 \ v_7 \ v_8)_{8 \times 8} \end{aligned}$$

Q can be represented with singular values σ_i , right singular matrix \mathbf{V} and left singular matrix \mathbf{U} as

$$Q = \sum_{i=1}^3 \sigma_i u_i v_i^T \quad (4.68)$$

in this way Q^{-1} can be computed as

$$Q^{-1} = \sum_{i=1}^3 \frac{1}{\sigma_i} v_i u_i^T \quad (4.69)$$

Introducing singularity measure of complete VSCMG cluster $m_v = \sqrt{\det(QQ^T)}$ in Equation 4.66 we have SVD based steering law to escape singularity as

$$\begin{pmatrix} \dot{\delta} \\ \dot{\Omega} \end{pmatrix}^* = W Q^T (Q W Q^T)^{-1} u + \kappa v_1 \quad (4.70)$$

where

$$\begin{aligned} \beta &= k_0 \exp(-k_1 m_c / m_w) \\ \kappa &= k_3 \exp(-k_4 m_v) \end{aligned} \quad (4.71)$$

for large m_v Equation 4.70 approaches Equation 4.66 otherwise to escape singular state, maximum torque applied orthogonal to singular surface through vector v_1 . Hybrid of Equation 4.70 with Off diagonal Singularity Robust steering law is given as

$$\begin{pmatrix} \dot{\delta} \\ \dot{\Omega} \end{pmatrix} = W Q^T (Q W Q^T + \lambda \mathbf{E})^{-1} u + \kappa v_1 \quad (4.72)$$

\mathbf{E} is not a diagonal metrics instead symmetric metrics with non diagonal elements.

$$\mathbf{E} = \begin{pmatrix} 1 & \epsilon_3 & \epsilon_2 \\ \epsilon_3 & 1 & \epsilon_1 \\ \epsilon_2 & \epsilon_1 & 1 \end{pmatrix} \quad (4.73)$$

weights of non diagonal elements of \mathbf{E} are harmonics composed as $\epsilon_i = \epsilon_0 \sin(nt + \varphi)$, $\varphi_i = \{0, \pi/2, \pi\}$

Chapter 5

Numerical Simulations

Numerical Simulations are performed in order to have better understanding of system and for validation of control and steering law. For better system sizing a priory results from numerical simulations are important and very crucial in design process. Adaptive Runge Kutta method is used for numerical integration of nonlinear equation of motion. Customized software code is developed with ability to easily change system physical characteristics and constants in equation of motion. Developed code is capable to simulate Reaction Wheel, CMG individually and combination of both as VSCMG. Tests results are discussed for regulation and rest to rest with the vicinity of singular states.

5.1 A priory dimensions

Small form factor is considered utmost priority in design of test bench, hence starting with base platform considering which should fit under 250x250x250mm³ and should not weigh more than 1.5kg. Apart from these test bed should also capable of carrying out maneuver with angular rate more than 3°/sec. For preliminary understanding, parameters shown in Table 5.1 considered for simulations.

Parameter	Symbol	Value	Unit
Skew Angle	β	54.73	deg
Platform Inertia	J_P	$diag([0.08, 0.08, 0.015])$	$kg \cdot m^2$
RW Inertia	J_W^s	10×10^{-6}	$kg \cdot m^2$
RW Inertia	J_W^g, J_W^t	5×10^{-6}	$kg \cdot m^2$
Gimbal Inertia	J_G^s, J_G^t, J_G^g	3×10^{-6}	$kg \cdot m^2$
CMG Inertia	$J_{CMG}^s, J_{CMG}^t, J_{CMG}^g$	$diag([15, 8, 8]) \times 10^{-6}$	$kg \cdot m^2$

Table 5.1. Preliminary system configuration and dimensions

5.2 RW based ACS

This section covers results in order to verify the dynamical model and sizing of reaction wheel. Two cases ha been studied, rest to rest reorientation to cancel

attitude error and station keeping maneuver with initial angular velocity error.

5.2.1 Rest to rest reorientation with RW only

Consider a case where satellite has to be reoriented 60 deg about its yaw axis in order to point solar panels towards sun, maneuver has to be done only using RWs and as per state defined in Table 5.2. This yaw error should be canceled within 20 seconds in order to satisfy minimum agility required.

Parameter	Value	Unit
q	$[1 \ 0 \ 0 \ 0]^T$	-
ω	$[0 \ 0 \ 0]^T$	deg / sec
q_d	$[\cos(\pi/6) \ 0 \ 0 \ \sin(\pi/6)]^T$	-
ω_d	$[0 \ 0 \ 0]^T$	rad/sec
δ	$[0 \ 0 \ 0 \ 0]^T$	rad
Ω	$[0 \ 0 \ 0 \ 0]^T$	rad/sec

Table 5.2. Initial and desired states with yaw error of 60 deg

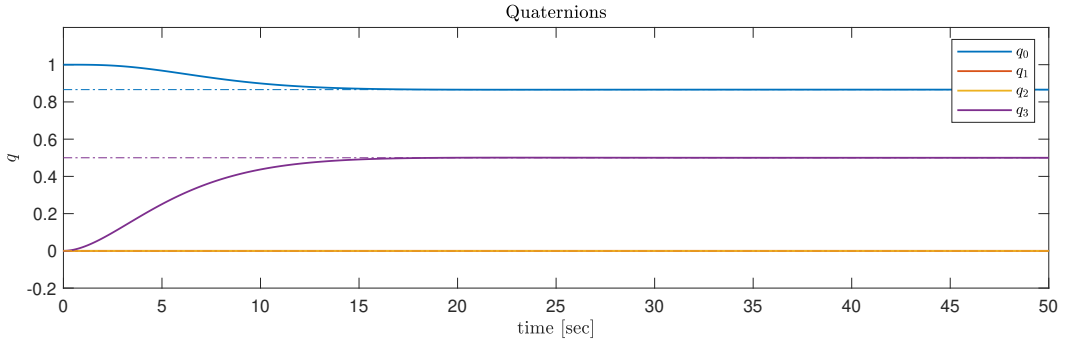


Figure 5.1. Quaternions for RW only rest to rest maneuver

Figure 5.1 to Figure 5.5 are results for given conditions in Table 5.2. It is clear from Figure 5.1 that system approaches steady state within 20 seconds. Controller gains are selected such that attitude in terms of Euler angle is shown in Figure 5.2 approaches reference yaw angle without overshoot.

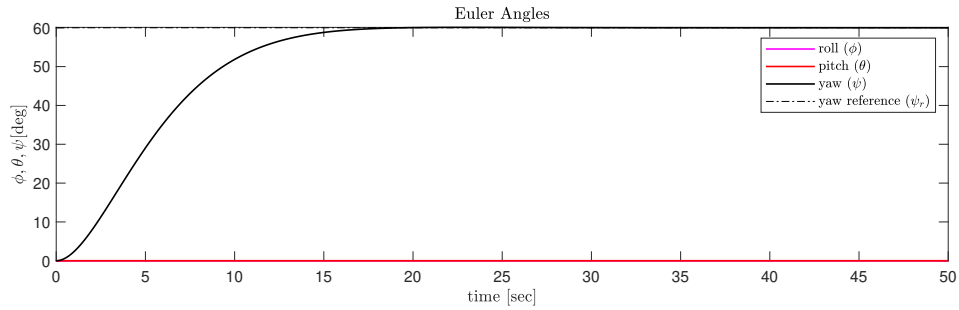


Figure 5.2. Euler angles for RW only rest to rest maneuver

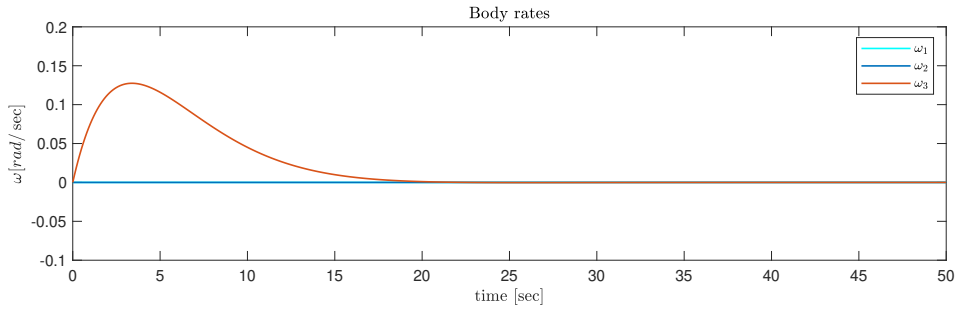


Figure 5.3. Body rates for RW only rest to rest maneuver

Notice in Figure 5.3 body angular velocity about yaw third axis considered as yaw starts from 0rad/sec . Peak angular velocity $0.125\text{rad/sec} \approx 7.16^\circ/\text{sec}$ occurs near 4 seconds and overall satisfying agility criteria of $3^\circ/\text{sec}$ by reaching steady state close to 20 sec.

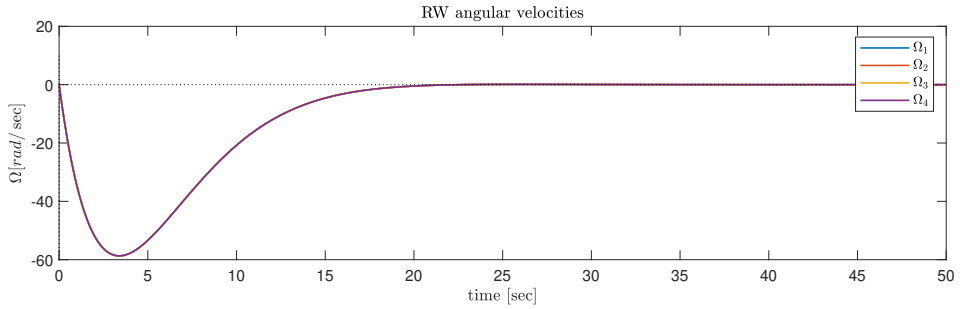


Figure 5.4. RW velocity for RW only rest to rest maneuver

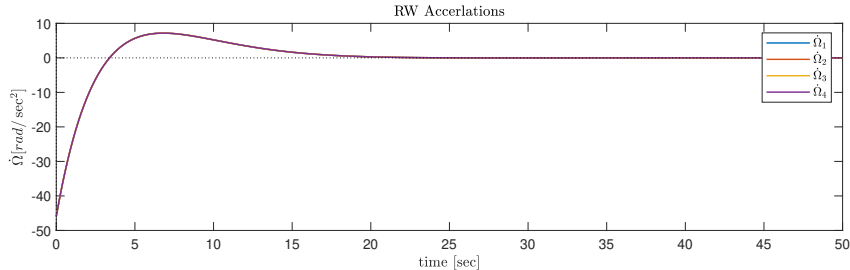


Figure 5.5. RW accelerations for RW only rest to rest maneuver

All the reaction wheels rotated in same direction with almost equal rate which is understandable for given situation, maximum wheel speed is within reasonable range close to $60\text{rad/sec} \approx 570\text{RPM}$, although initial RW acceleration starts from -50rad/sec^2 which probably should be smoothed by introducing proper gain scheduling, although these results are with preliminary assumption of geometrical properties and inertia and may change for final geometry.

5.2.2 Regulation maneuver with RW only ACS

Consider a scenario in which a satellite with configuration mentioned in Table 5.1 but subjected to small disturbance along body axis undergoes initial body rate error $\omega_e = [-2 \ 5 \ 2]^T \text{deg/sec}$ has to counteract this error and should maintain its steady state such a way that asymptotic $q_e = [1 \ 0 \ 0 \ 0]^T$. This is type of station attitude keeping maneuver often needs to be performed when satellite deploys its antenna or solar panel or subjected to impulse disturbance. Starting with same initial conditions from Table 5.2 except $q_d = q = [1 \ 0 \ 0 \ 0]^T$

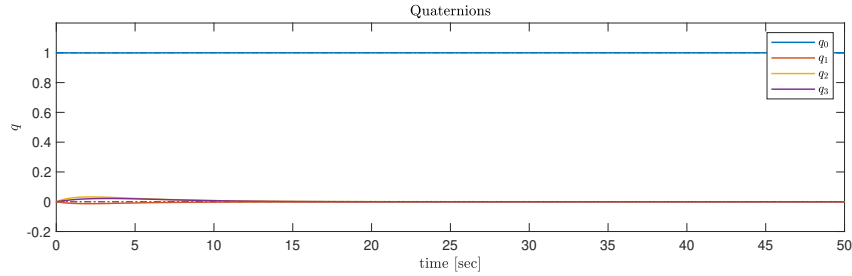


Figure 5.6. Quaternions for RW only station keeping maneuver

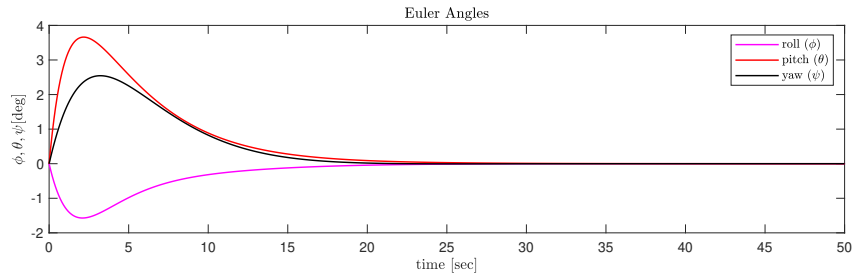


Figure 5.7. Euler angles for RW only station keeping maneuver

Results of initial body error problem are shown in Figure 5.6 to Figure 5.10. We can note quaternion initially at rest are subjected to small variation and approaches its initial state in about 15 seconds. This is clearly visible in terms of Euler angles shown in Figure 5.7 all three angles roll, pitch and yaw moved to peak angles approximately -1.5° , 3.5° and 2.4° respectively and slowly approaches to zero. Body rates shown in Figure 5.8 starts from $[-0.0349, 0.0873, 0.0349] \text{rad/sec}$ smoothly approaches zero without showing any overshoot thanks to selected controller gain values.

$$\mathbf{Kq} = \begin{pmatrix} 300 & 0 & 0 \\ 0 & 300 & 0 \\ 0 & 0 & 300 \end{pmatrix}; \quad \mathbf{Kw} = \begin{pmatrix} 850 & 0 & 0 \\ 0 & 850 & 0 \\ 0 & 0 & 850 \end{pmatrix} \quad (5.1)$$

In Figure 5.9 notice how RW rates starting from zero diverge initially for 5 seconds and then maintain steady state velocities within range of -50 to 100 rad/sec although these are within the limit but may undergo saturation for large disturbances

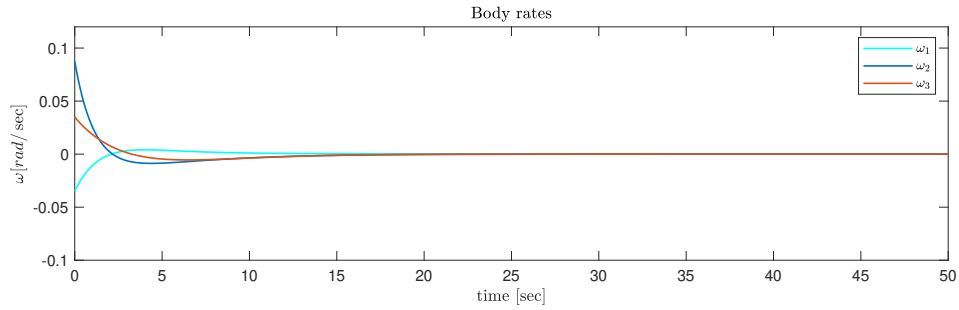


Figure 5.8. Body rates for RW only station keeping maneuver

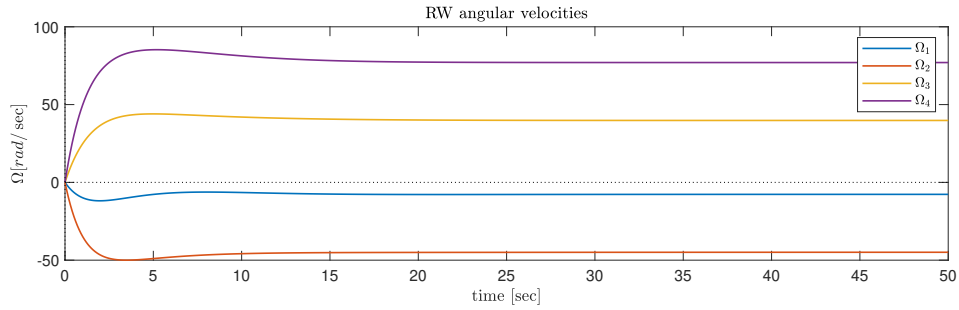


Figure 5.9. RW velocity for RW only station keeping maneuver

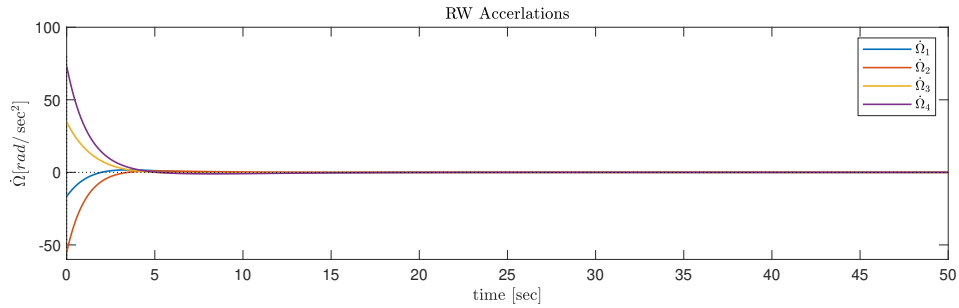


Figure 5.10. RW accelerations for RW only station keeping maneuver

From Figure 5.5 we can see that Reaction wheels undergoes accelerations with magnitude up to rad/sec^2 this parameter depends on inertia ratio of Platform to RW and can be reduced by either reducing platform inertia or by increasing RW inertia which is not suitable most of the time, thus torque amplification by CMG can be performed.

5.3 CMG based ACS

Despite the fact that RW based ACS is capable of eliminating attitude error in any direction, magnitude of torque produced is very low and limited by RW inertia, and may lead to saturation for large torque requirements. Subsequently, in the interest of taking advantage of torque amplification rest to rest and regulation maneuver are studied with CMG only control system.

5.3.1 Rest to rest reorientation with CMG only ACS

Consider a satellite has to perform reorientation maneuver in order to cancel the attitude error in Euler angle $[\phi \theta \psi] = [30 60 90]$ deg considering initial and desired states mentioned in Table 5.3

Parameter	Value	Unit
q	$[1 0 0 0]^T$	-
ω	$[0 0 0]^T$	deg / sec
q_d	$[0.6830 - 0.1830 0.5000 0.5000]^T$	-
ω_d	$[0 0 0]^T$	rad/sec
δ	$\left[\frac{\pi}{2}, \frac{\pi}{2}, \frac{\pi}{2}, \frac{\pi}{2} \right]^T$	rad
Ω	$[800, 800, 800, 800]^T$	rad/sec

Table 5.3. Initial and desired states for attitude error $\phi = 30^\circ, \theta = 60^\circ, \psi = 90^\circ$

Time criterion for maneuver to be performed within 30 seconds will demonstrate performance beyond baseline agility requirement, and to do so Horowitz gains should be carefully selected for asymptotic stability.

$$\mathbf{Kq} = \begin{pmatrix} 1 & 0 & 0 \\ 0 & 1 & 0 \\ 0 & 0 & 1 \end{pmatrix}; \quad \mathbf{Kw} = \begin{pmatrix} 1.5 & 0 & 0 \\ 0 & 1.5 & 0 \\ 0 & 0 & 1.5 \end{pmatrix} \quad (5.2)$$

Notice gains selected for CMG only ACS are much lower than those mentioned in Equation 5.1 selected for RW only ACS, we can infer that CMG can produce much higher torques compared with RW thus gain is reduced by order of magnitude of hundreds.

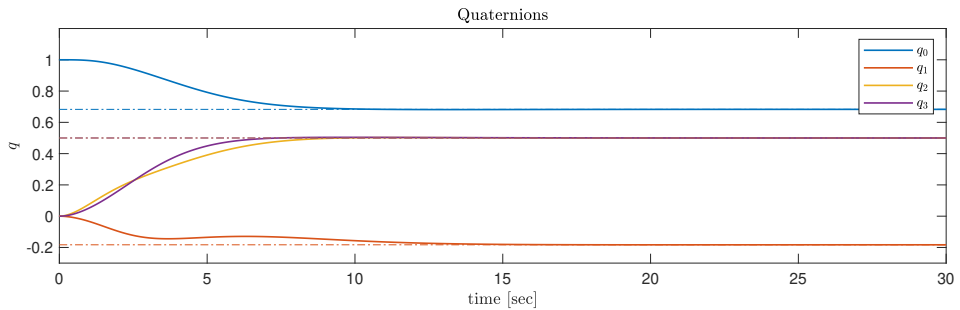


Figure 5.11. Quaternions for CMG only reorientation with attitude error $[\phi \theta \psi] = [30, 60, 90]^\circ$

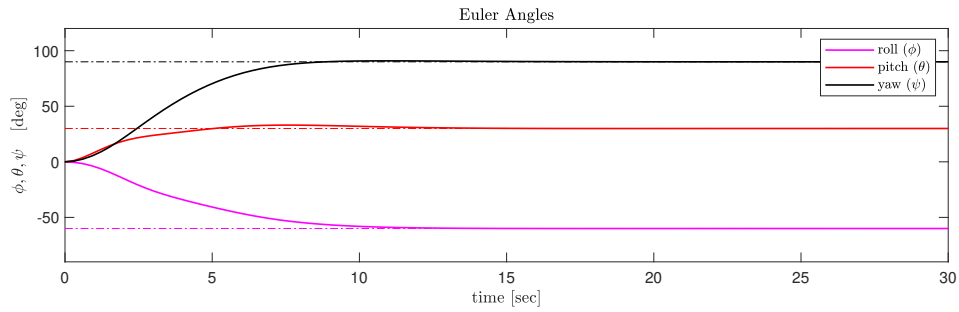


Figure 5.12. Euler angles for CMG only reorientation with attitude error $[\phi \theta \psi] = [30, 60, 90]^\circ$

Figure 5.11 to Figure 5.16 are results for attitude error compensation maneuver with reference roll pitch yaw set as $[\phi \theta \psi] = [30, 60, 90]^\circ$. Since gimbal state is far away from singularity, satellite smoothly approaches to reference states clearly seen from Figure 5.11 and Figure 5.12.

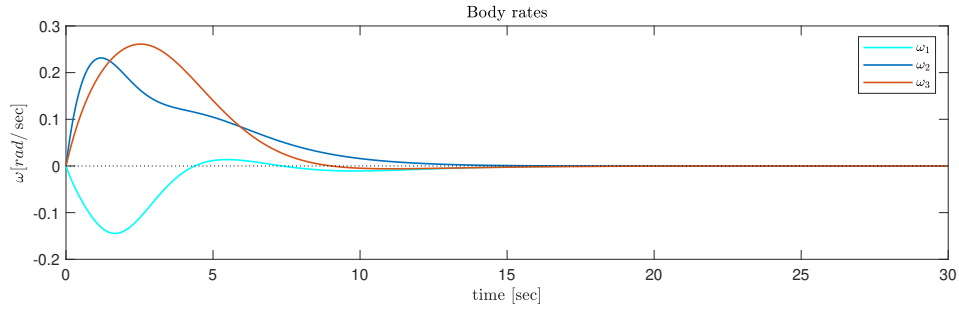


Figure 5.13. Body rates for CMG only reorientation with attitude error $[\phi \theta \psi] = [30, 60, 90]^\circ$

With negligible overshoot in body rate about third axis, satellite reaches steady state within 20 seconds seen in Figure 5.13. Gimbal angles initially set at $\pi/2\text{rad}$ remains within magnitude of 1.2 to 1.9 radian and no more than 20° variation in gimbal angles is noticeable in Figure 5.14. Although gimbal angular velocities shown in Figure 5.15 has rapid variations which is understandable due to such a large slew motion is performed within 20 seconds. Moreover, smooth curves denotes CMG, was far away from singularity.

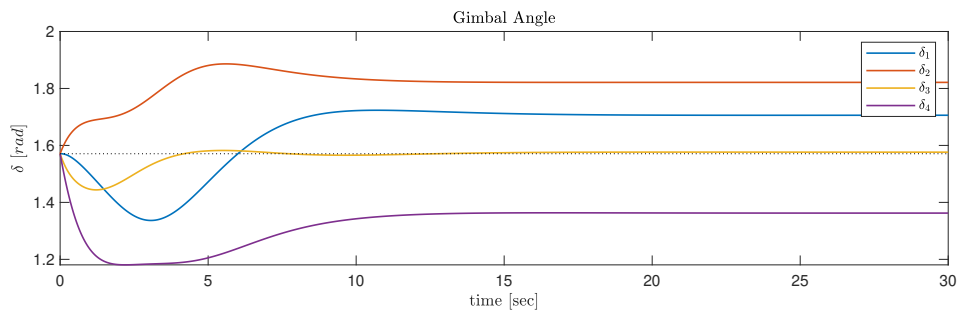


Figure 5.14. Gimbal angles for CMG only reorientation with attitude error $[\phi \theta \psi] = [30, 60, 90]^\circ$

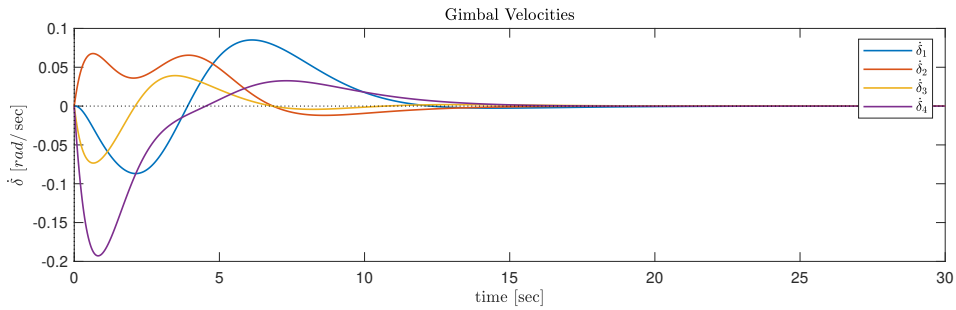


Figure 5.15. Gimbal rates for CMG only reorientation with attitude error $[\phi \theta \psi] = [30, 60, 90]^\circ$

Gimbal acceleration shown in Figure 5.16 are signals provided to gimbal motor in order to track required gimbal velocity for steering law. These accelerations are proportional to current supplied to gimbal motor. Acceleration magnitude is within range of 1rad/sec^2 will not compromise the structural integrity of system.

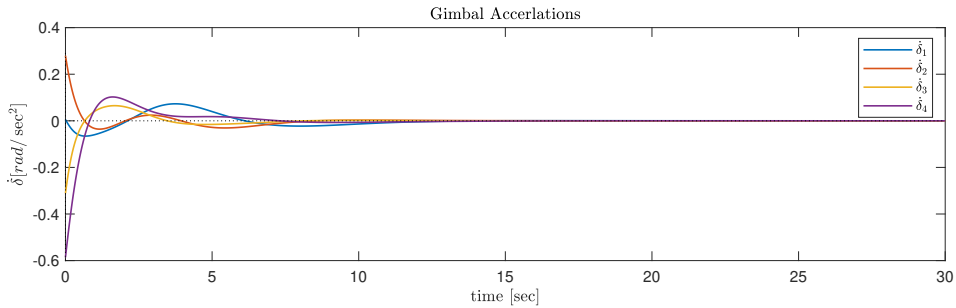


Figure 5.16. Gimbal rates for CMG only reorientation with attitude error $[\phi \theta \psi] = [30, 60, 90]^\circ$

5.3.2 Body rate regulation with CMG only ACS

Consider another scenario in which satellite is subjected to step disturbance, ACS has to cancel angular velocity error and approach to its initial attitude, considering states from

Parameter	Value	Unit
$q = q_d$	$[1 \ 0 \ 0 \ 0]^T$	-
ω	$[0 \ 10 \ 0]^T$	deg / sec
ω_d	$[0 \ 0 \ 0]^T$	rad / sec
δ	$[0, \ 0, \ 0, 0]^T$	rad
Ω	$[800, \ 800, \ 800, \ 800]^T$	rad / sec

Table 5.4. Initial and desired states for angular velocity error with CMG in singular configuration

It is clear that CMG is at inescapable singularity thus combination of SVD based and off diagonal singularity avoidance steering law is used with gains selected

by trial and error with numerous iterations.

$$\mathbf{Kq} = \begin{pmatrix} 5.3 & 0 & 0 \\ 0 & 5.3 & 0 \\ 0 & 0 & 5.3 \end{pmatrix}; \quad \mathbf{Kw} = \begin{pmatrix} 2.5 & 0 & 0 \\ 0 & 2.5 & 0 \\ 0 & 0 & 2.5 \end{pmatrix} \quad (5.3)$$

with using off diagonal singularity robust steering steering law as

$$\dot{\delta} = \mathbf{WG}_t^T (\mathcal{G}_t \mathbf{WG}_t^T + \lambda \mathbf{E})^{-1} + \lambda \mathbf{v}_1 \quad (5.4)$$

where, weight matrices are selected by adding off diagonal harmonics as

$$\mathbf{W} = \begin{pmatrix} 1 & \lambda & \lambda & \lambda \\ \lambda & 2 & \lambda & \lambda \\ \lambda & \lambda & 3 & \lambda \\ \lambda & \lambda & \lambda & 4 \end{pmatrix}$$

and

$$\mathbf{E} = \begin{pmatrix} 100 & \epsilon_3 & \epsilon_2 \\ \epsilon_3 & 100 & \epsilon_1 \\ \epsilon_2 & \epsilon_1 & 100 \end{pmatrix}$$

with $\epsilon_i = 0.1 \sin(\pi t + \varphi)$, $\varphi_i = \{0, \pi/2, \pi\}$ and $\lambda = 0.1 \exp(-10 \det(\mathcal{G}_t \mathcal{G}_t^T))$. Results of CMG at singular states are shown in simulation Figure 5.17 to Figure 5.22. Since CMG singularity is zero at the beginning satellite slowly diverges from set point, at first it performs complete 360° rotation in yaw axis for about 245 seconds shown in Figure 5.19. Note that even there is discontinuity visible at 150 seconds, it is due to wrapping of Euler angles within range of -180° to 180°. Rapid variation in body rate occurs, a spike seen near 250 seconds in Figure 5.18 and from zoomed view of body rate shown in Figure 5.22b magnitude of about 1.5 rad/sec occurs before reaching steady within next 10 seconds.

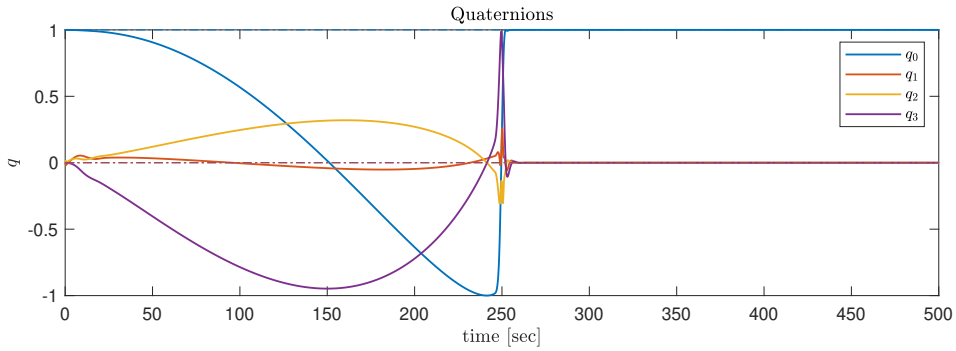


Figure 5.17. Quaternions for station keeping with CMG only ACS

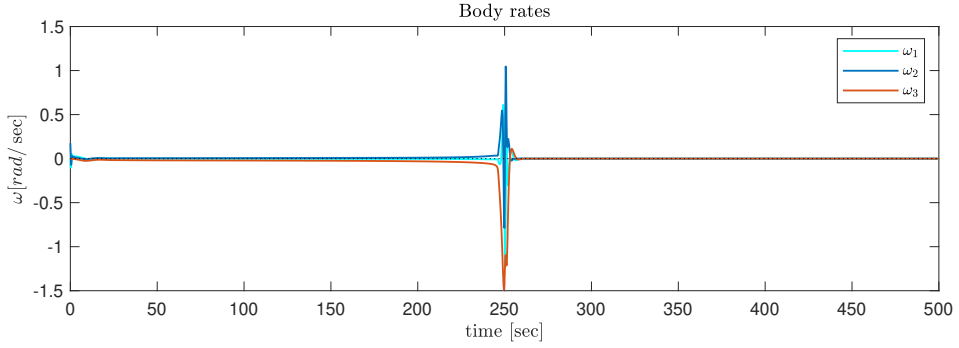


Figure 5.18. Body Rates for station keeping with CMG only ACS

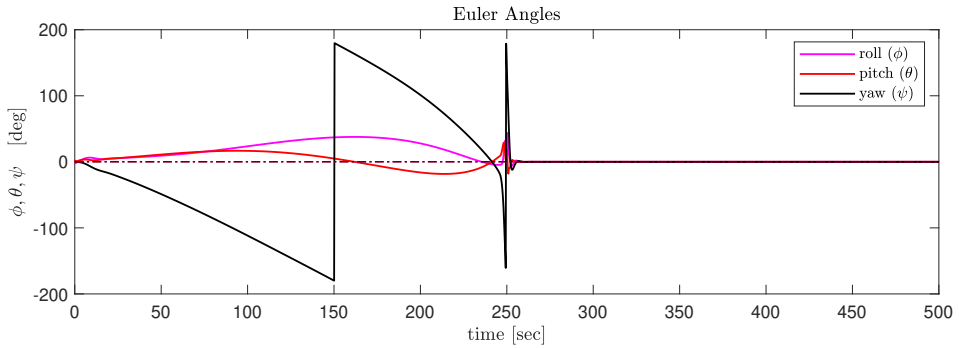


Figure 5.19. Euler angles for station keeping with CMG only ACS

Gimbal angles slowly increase till 240 seconds and sudden jump occurs near 250 seconds. Figure 5.21 and Figure 5.22c are gimbal velocity and its zoomed view, notice how gimbal velocities rapidly change from 245 to 255 seconds Despite the fact that gimbal velocities are not exceptionally high, entire maneuver took about 270 seconds before reaching steady state which is not favorable. Thus being capable of producing large torque amplification, CMG alone can not guarantee smooth tracking performance. Moreover, finding perfect parameters and gains for particular task is not trivial since they vary depending on type of singularity and state.

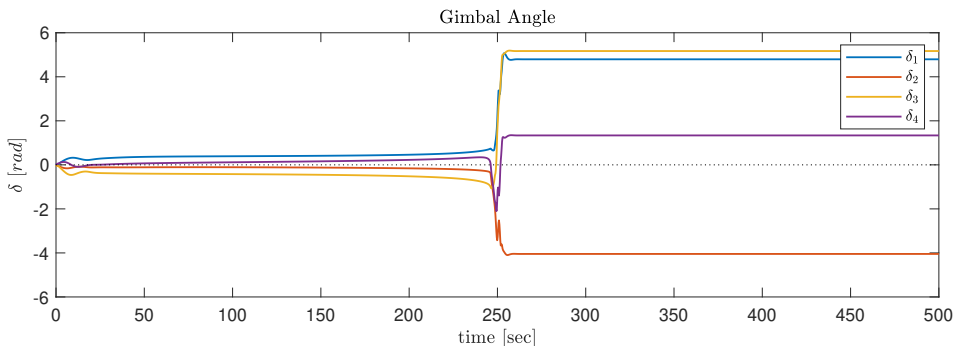


Figure 5.20. Gimbal angles for station keeping with CMG only ACS

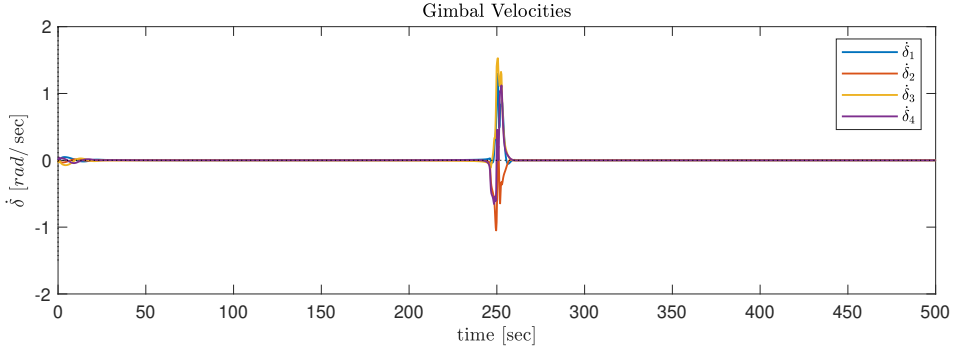


Figure 5.21. Gimbal velocities for station keeping with CMG only ACS

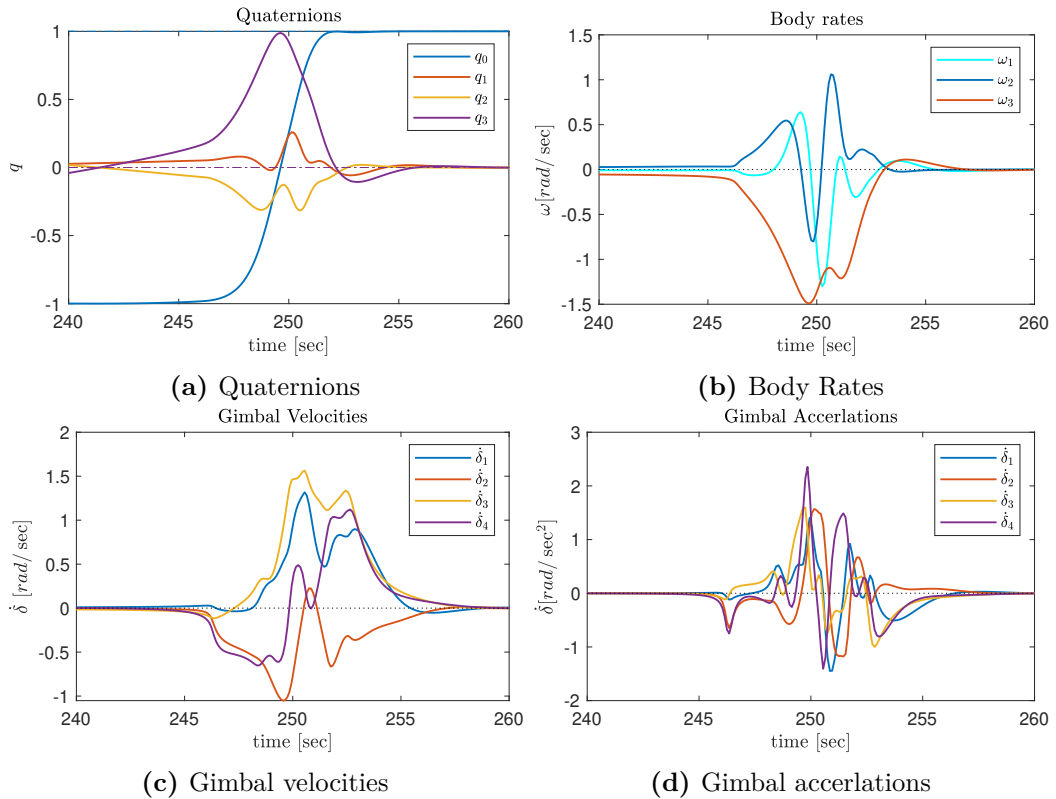


Figure 5.22. Zoomed view of station keeping maneuver with CMG only ACS

5.4 VSCMG based ACS

In this section simulation results Attitude Control System based of complete Variable Speed Control Moment Gyroscope arranged in as pyramid cluster is discussed. Two types of simulations are performed first comparison with only CMG based ACS and later trajectory tracking maneuver is presented.

5.5 Body rate regulation with VSCMG

Considering same scenario of CMG only ACS discussed in previous section. We have deliberately set the gimbal configuration satellite state and initial angular velocity as shown in Table 5.4 so that CMG is in singular state. Now advancing with same situation occurred with VSCMG based ACS. Controller gains and steering parameters are set as

$$\mathbf{Kq} = \begin{pmatrix} 300 & 0 & 0 \\ 0 & 300 & 0 \\ 0 & 0 & 300 \end{pmatrix}; \quad \mathbf{Kw} = \begin{pmatrix} 850 & 0 & 0 \\ 0 & 850 & 0 \\ 0 & 0 & 850 \end{pmatrix} \quad (5.5)$$

Notice selected gains are much higher than CMG only ACS. Bearing in mind that with higher gains were not Horowitz due to singularities present in CMG and bringing settling closer to 60 seconds was not possible. And constants for off-diagonal singularity robust steering law are

$$\begin{aligned} \lambda &= 0.01 \exp(-10m_c) \\ \beta_i &= \min \left\{ 1 \times 10^3 \exp(-0.01m_c/m_v), 1000 \right\} \\ \kappa &= 0.001 \exp(-10m_v) \end{aligned}$$

here β_i is clipped to 1000 in order to avoid computational singularity when m_v approaches zero.

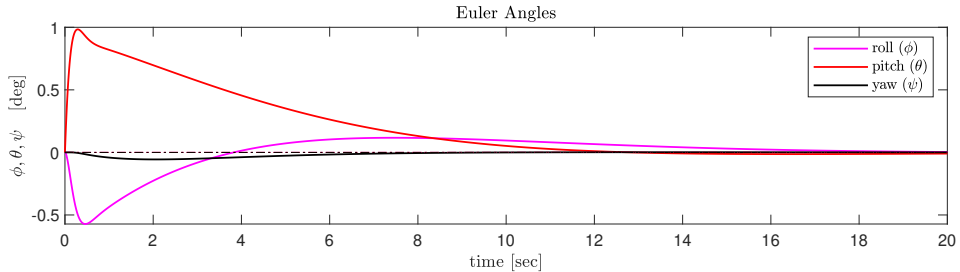


Figure 5.23. Euler angles for station keeping with VSCMG in vicinity of singularity

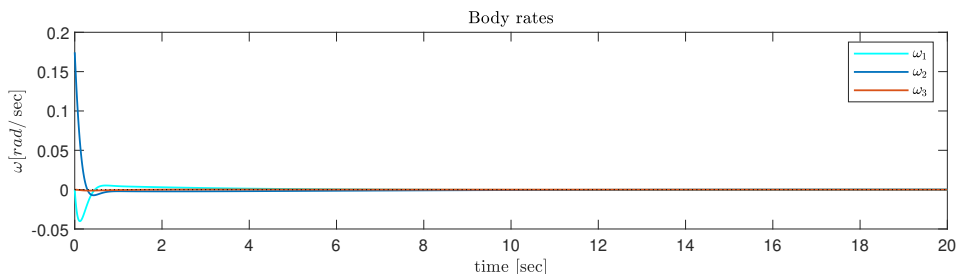


Figure 5.24. Body rates for station keeping with VSCMG in vicinity of singularity

Upon initial disturbance Euler angles first rapidly increase but does not change more than 1° due to high value of \mathbf{K}_w and smoothly settles to desired state within 20

seconds as shown in Figure 5.23. Cancellation of velocity error verified from body rates shown in Figure 5.24

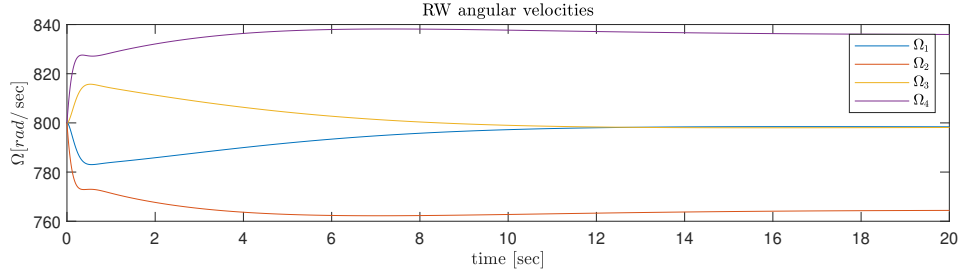


Figure 5.25. RW rates for station keeping with VSCMG in vicinity of singularity

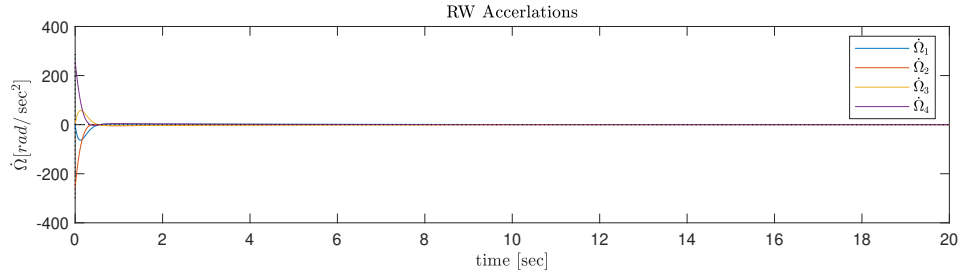


Figure 5.26. RW accelerations for station keeping with VSCMG in vicinity of singularity

Despite RW change in velocities in Figure 5.25 are not too large, they are subjected to high accelerations shown in Figure 5.26 with maximum magnitude if 220 rad/sec^2 which can be minimized with relaxed settling time criterion. At the same time gimbal velocities are considerably low which is evident due to high momentum of RW. Overall there is no chattering or high frequency components present in any of state despite existence of singularity.

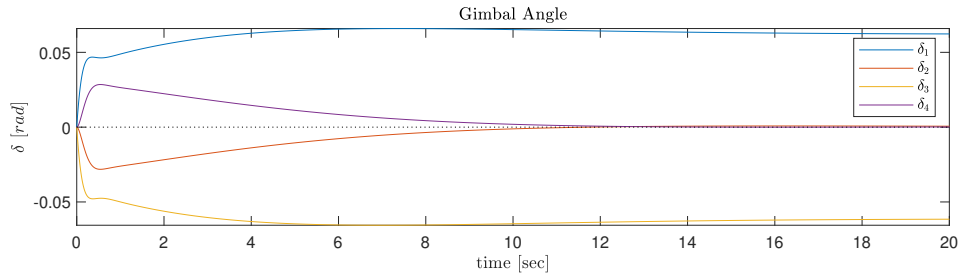


Figure 5.27. Gimbal angles for station keeping with VSCMG in vicinity of singularity

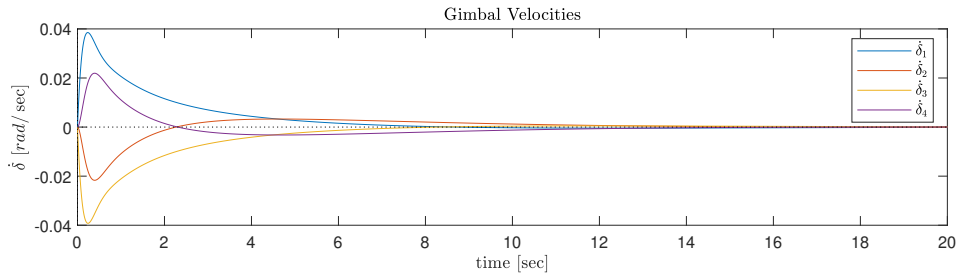


Figure 5.28. Gimbal velocities for station keeping with VSCMG in vicinity of singularity

5.6 Trajectory tracking with VSCMG ACS

For verification of VSCMG based ACS and in order to test capabilities of steering law for large maneuvers for long period. An hypothetical scenario is assumed as a nadir pointing satellite in highly elliptical orbit has to maintain its payload towards earth. Since for elliptical satellite has to rotate at non constant speed in order to maintain its attitude with respect to true anomaly. Orbital parameters of “MOLNIYA 1-86” launched on 26 May 1993 by USSR is taken as reference satellite. A Highly Elliptical Orbit with parameters shown in Table 5.5 was communications satellite used to test a system of radio communications and television broadcasting using earth satellites as active transponders and to experiment with the system in practical use.[36]

Parameter	Value	Unit
Inclination	63.103	deg
Eccentricity	0.48485	-
Semi major axis	13353.0	km
Apogee	13457.1	km
Perigee	508.0	km
Time period	15354.2	sec

Table 5.5. MOLNIYA 1-86 Orbital details

Reference trajectory in terms of Euler axis angle is realized by numerically solving Kepler equations of mean motion (n), Mean (M) Eccentric (E) and True anomaly

$$n = \sqrt{\frac{\mu}{a^3}} \quad (5.6)$$

$$\begin{aligned} M &= M_0 + n(t - t_0) \\ M &= E - e \sin E \end{aligned} \quad (5.7)$$

$$\tan \frac{\nu}{2} = \sqrt{\frac{1+e}{1-e}} \tan \frac{E}{2} \quad (5.8)$$

Iterative solution is used to find mean anomalies for 10 periods of satellite to form a reference trajectory such that axis orthogonal to orbital plane is rotated by angle ν and quaternions are computed as

$$q(t) = \left[\cos \frac{\nu(t)}{2}, 0, 0, \sin \frac{\nu(t)}{2} \right]^T$$

Reference quaternions for Nine complete orbits are shown in Figure 5.29 and results of trajectory tracking are shown from Figure 5.33 to Figure 5.33.

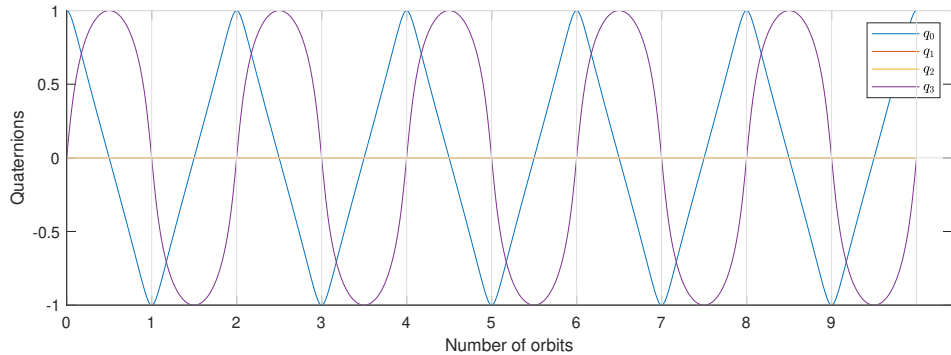


Figure 5.29. Reference trajectory quaternions computed for MOLNIYA 1-86

Since trajectory tracked by satellite overlaps reference trajectory, least square residuals between reference quaternions and simulated quaternions are shown in Figure 5.30 notice the deviation is within order of magnitude 10^{-6}

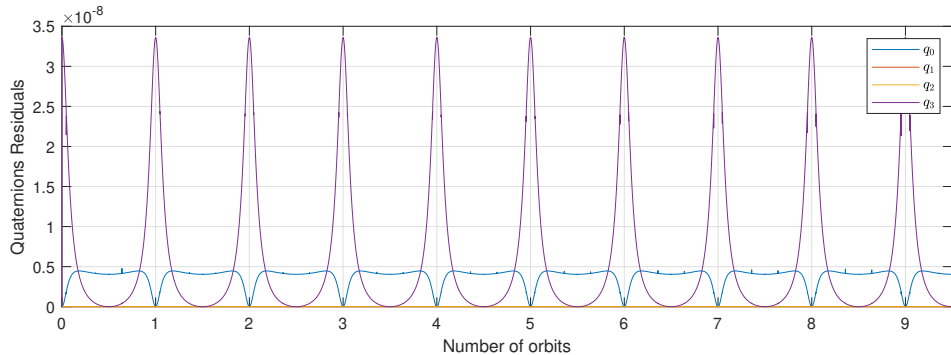


Figure 5.30. Least square residuals of quaternions computed for MOLNIYA 1-86

Pitch and roll axis were placed in orbital plane, 9 complete revolutions are seen about yaw axis shown in Figure 5.31.

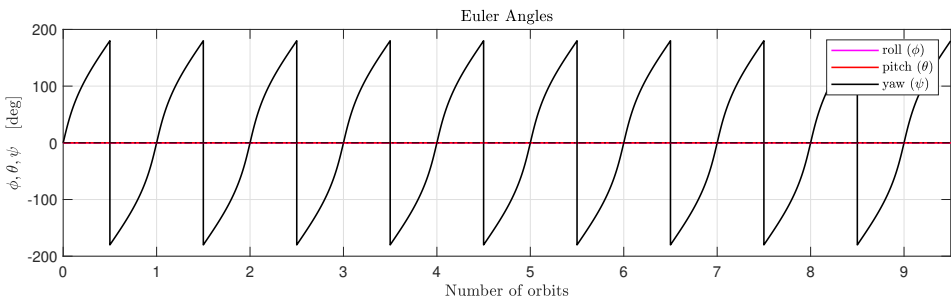


Figure 5.31. Euler angles computed for MOLNIYA 1-86

Satellite orbital period is large and has to perform only one revolution per orbit due as a result body rates of tracked trajectory are very low. Although we can see from peaks at each orbit that rates slows down till apogee and accelerates till perigee.

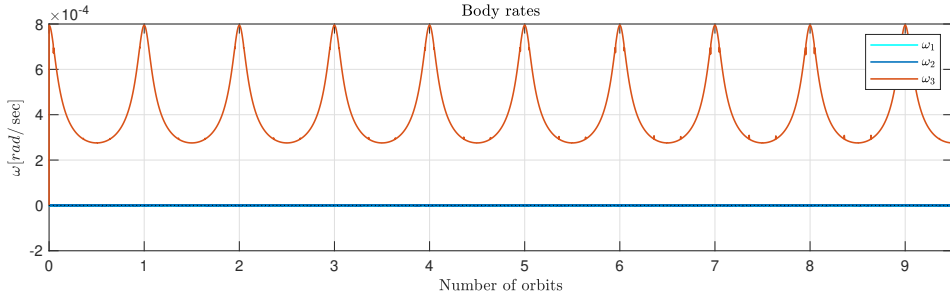


Figure 5.32. Body rates for trajectory tracking maneuver

Similarly, in order to maintain varying body rate, RW velocities oscillate within magnitude of 0.2 rad/sec

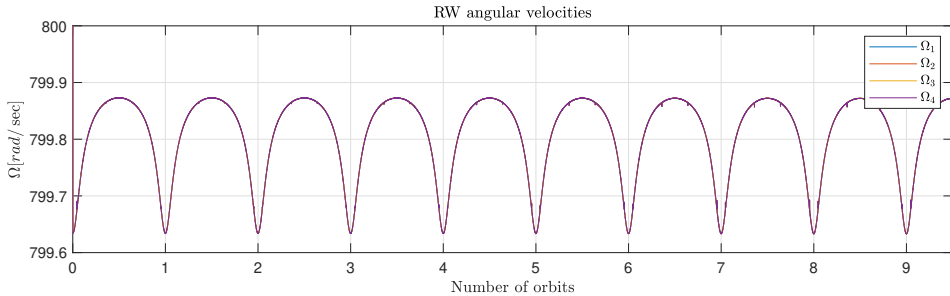


Figure 5.33. RW angular velocity for trajectory tracking maneuver

From the results, it is clear that VSCMG based ACS are more beneficial than RW based and CMG based ACS. Clear advantages of VSCMG are listed below.

1. VSCMG does not poses problem of singularities.
2. they can produce large torque amplification like CMG,
3. are able to steer away from singular state by using RWs.
4. Moreover, Operation is smooth and gimbal rates are within permissible range and no impulsive motion or chattering occurs thus does not poses threat to mechanical integrity of system.

Verified dynamics of VSCMG is further implemented in to standalone environment in C++ with Runge–Kutta ODE solver for integration. This environment is used for training Neural Network based steering law through reinforcement learning explained in next Chapter.

Chapter 6

Neural Network based Learning Agent

In this chapter Artificial Intelligence based agent particularly Neural Network strategy is proposed to evaluate steering of variable speed control moment gyroscope. Machine learning scheme especially reinforcement learning with combination of supervised learning is followed to train neural network. From equations of motion and control architecture derived in it is evident that spacecraft attitude dynamics is nonlinear function of its states. Moreover singularity avoidance steering mechanism is complex and computationally expensive. Neural network are capable of approximating nonlinear functions and produce sub-optimal solution which is beneficial to reduce computational loads moreover steering is possible without matrix inversion. To design complete neural network based ACS following sections are discussed to clear some concepts. Starting with a brief introduction about machine learning types, particular interest of this thesis is focused on policy gradient method especially Proximal Policy Optimisation is discussed in detail.

6.1 Machine Learning

Machine learning is sub domain of AI is strategy to solve specific task without explicitly programming details of system. Strategy or plan is learned through available labeled data sets. Basically a black box model is approximated by studying large amount of input associated output, exploring unlabeled data or by enumerating inputs and outputs of black box function. Based on strategy machine learning is classified in three major parts and their application is shown in figure.

6.1.1 Supervised Learning

In this strategy labeled output for particular inputs are known and agent learns relation from input and output mostly used in predictive analysis. Explicitly defined labels are needed hence the name. Model predicts output based on current input and later compare it with labeled output. Two types of supervised learning are classification with categorical output and regression with numerical output such as fitting a curve. In this thesis supervised learning is used to partially learn strategy

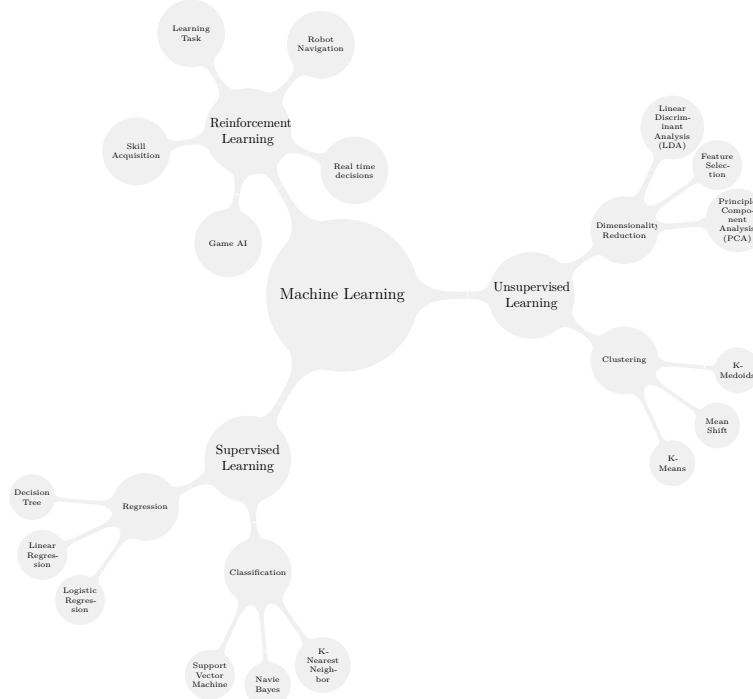


Figure 6.1. Machine Learning Classifications

from data set produced using steering law discussed in previous chapter in order to reduce training time.

6.1.2 Unsupervised Learning

Machine learns by exploring large chunk of unlabeled data set. Clustering and dimensionality reduction are two sub-classes of unsupervised learning. In this case information is retrieved from data set with keeping simpler and spars representation than original data, can be used to discover pasterns in given data-set. In pattern recognition similar data samples are clustered together.

6.1.3 Reinforcement Learning

Reinforcement learning is a close loop problem where agent takes action, each Action is associated with Reward or penalty, and based on outcome agent tries to maximize reward or minimize the penalty by exploring in to environment or exploiting past experiences through trial and error along with received feedback. Figure 6.2 shows architecture of agent-environment interaction in Markov Decision Processes.[37]

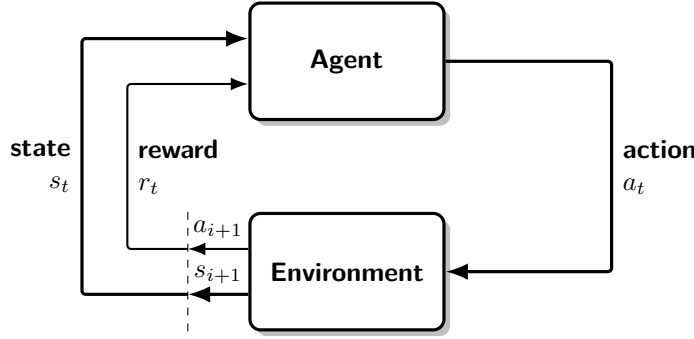


Figure 6.2. The agent-environment interaction in interaction in a Markov Decision Process.
[1]

Agent is any entity that perceives Environment using sensors and acts on it using actuators. A rational agent should take appropriate actions based on strategy to reach goal. Success of agent is determined by performance measure. Agent function that maps precept history to action is given as:

$$f : \mathcal{P}^* \longrightarrow \mathcal{A} \quad (6.1)$$

Environment is a real situation or simulated plant dynamics and may have properties such fully or partially observable, deterministic or stochastic, discrete or continuous. **Perceptions** are observed states $s \in \mathcal{S}$ in the environment through sensors whereas **actions** $a \in \mathcal{A}$ are performed by agent through actuators. Agent at State s inside environment, chooses one action a among many choices in order to evolve its state and evolution is determined by state transition probability. For each action, environment provides reward $r \in \mathcal{R}$ as feedback. The Markov Decision Processes (MDP) consists of set of states \mathcal{S} , set of actions \mathcal{A} , transition probability function P reward function R , discounting factor for future rewards γ

$$\mathcal{M} = \langle \mathcal{S}, \mathcal{A}, P, R, \gamma \rangle$$

A **Policy** $\pi(s)$ is, therefore, a strategy that an agent uses in pursuit of goals.[37] Policy determines actions that has to be taken by agent at state s . Policy can be deterministic: $\pi(s) = a$ or stochastic: $\pi(a|s) = \mathbb{P}_\pi[A = a|S = s]$

Each state is associated with a **Value** $V(s)$ function which is probability of future rewards than can be received by acting on policy at given state. With future reward as total some of rewards going forward from time t noted as G_t

$$G_t = R_{t+1} + \gamma R_{t+2} + \dots = \sum_{k=0}^{\infty} \gamma^k R_{t+k+1} \quad (6.2)$$

Here discount factor $\gamma \in [0, 1]$ is introduced to penalize the future rewards since propagation of uncertainty becomes larger for long time. The state value is expected return at given state:

$$V_\pi(s) = \mathbb{E}_\pi[G_t | S_t = s] = \sum_{a \in \mathcal{A}} Q_\pi(s, a) \pi(a|s) \quad (6.3)$$

Where, action-value of state action pair

$$Q_\pi(s, a) = \mathbb{E}_\pi[G_t | S_t = s, A_t = a] \quad (6.4)$$

Advantage function $A(s, a)$ is difference between state-value and action value, it asses quality of selected action with respect to certain state.

$$A_\pi(s, a) = Q_\pi(s, a) - V_\pi(s) \quad (6.5)$$

An optimum Value function that produces maximum returns is

$$V_*(s) = \max_\pi V_\pi(s), Q_*(s, a) = \max_\pi Q_\pi(s, a) \quad (6.6)$$

and the policy that achieves optimum value function is optimal policy given as

$$\pi_* = \arg \max_\pi V_\pi(s), \pi_* = \arg \max_\pi Q_\pi(s, a) \quad (6.7)$$

The agent-environment interaction is produces series of state, action and reward each time step evolved from $t = 0, 1, 2, \dots, T$. Hence, evolution is sequence state $S_t \in \mathcal{S}$, action $A_t \in \mathcal{A}(s)$ and rewards $R_{t+1} \in \mathcal{R}$ taken at each time t to end of an Episode at terminal time T . Markov Decision Processes shown in Figure 6.2 gives rise to sequence:

$$S_0, A_0, R_1, S_1, A_1, R_2, \dots, S_T, A_T, R_{T+1},$$

The model is function that describes environment with associated transition probability P and reward function R . Evaluation from state s to next state s' fro action a and associated reward r is transition step and represented as tuple (s, a, s', r) . The probability of transition $s \xrightarrow{a} s'$ is given as

$$P(s', r | s, a) = \mathbb{P}[S_{t+1} = s', R_{t+1} = r | S_t = s, A_t = a] \quad (6.8)$$

state transition matrix as function of $P(s', r | s, a)$:

$$P_{ss'}^a = P(s' | s, a) = \mathbb{P}[S_{t+1} = s' | S_t = s, A_t = a] = \sum_{r \in \mathcal{R}} P(s', r | s, a) \quad (6.9)$$

and reward function that predicts next reward upon action is

$$R(s, a) = \mathbb{E}[R_{t+1} | S_t = s, A_t = a] = \sum_{r \in \mathcal{R}} r \sum_{s' \in \mathcal{S}} P(s', r | s, a)$$

In MDP future only depends on current state and does not have effects of history.

$$\mathbb{P}[S_{t+1} | S_t] = \mathbb{P}[S_{t+1} | S_1, \dots, S_t] \quad (6.10)$$

Decomposition of value function in to immediate reward and the discounted future values using Bellman Equations as

$$\begin{aligned} V(s) &= \mathbb{E}[G_t | S_t = s] \\ &= \mathbb{E}[R_{t+1} + \gamma R_{t+2} + \gamma^2 R_{t+3} + \dots | S_t = s] \\ &= \mathbb{E}[R_{t+1} + \gamma(R_{t+2} + \gamma R_{t+3} + \dots) | S_t = s] \\ &= \mathbb{E}[R_{t+1} + \gamma G_{t+1} | S_t = s] \\ &= \mathbb{E}[R_{t+1} + \gamma V(S_{t+1}) | S_t = s] \end{aligned} \quad (6.11)$$

and action value also referred as Q value is

$$\begin{aligned} Q(s, a) &= \mathbb{E}[R_{t+1} + \gamma V(S_{t+1}) | S_t = s, A_t = a] \\ &= \mathbb{E}[R_{t+1} + \gamma \mathbb{E}_{a \sim \pi} Q(S_{t+1}, a) | S_t = s, A_t = a] \end{aligned} \quad (6.12)$$

6.2 Policy Gradient Methods

In order to solve RL problem that is to find optimal strategy with which agent achieves optimal rewards. Policy Gradient Method [38] learns with parametrized function of $\theta, \pi_\theta(a|s)$. The reward value depends on the policy and learning is done through optimizing θ for best rewards. The reward function is defined as:

$$J(\theta) = \sum_{s \in \mathcal{S}} d^\pi(s) V^\pi(s) = \sum_{s \in \mathcal{S}} d^\pi(s) \sum_{a \in \mathcal{A}} \pi_\theta(a|s) Q^\pi(s, a) \quad (6.13)$$

here d^π is the stationary distribution of Markov chain for π_θ . The idea is for by exploring states of

Markov chain for long period of time, probability of conversing to one state becomes constant and known as stationary probability for π_θ . Starting from initial state s_0 up to state s_t with using policy π_θ the stationary distribution d^π is given as:

$$d^\pi(s) = \lim_{t \rightarrow \infty} P(s_t = s | s_0, \pi_\theta) \quad (6.14)$$

Now with using gradient ascent search for best θ that gives maximum rewards.

6.2.1 Policy Gradient Theorem

Consider the θ with k dimensions is to be optimized, numerical gradient of θ can be found with introducing small perturbation ϵ

$$\frac{\partial J(\theta)}{\partial \theta_k} \approx \frac{J(\theta + \epsilon u_k) - J(\theta)}{\epsilon} \quad (6.15)$$

and for analytical gradient of $J(\theta)$

$$\begin{aligned} J(\theta) &= \sum_{s \in \mathcal{S}} d(s) \sum_{a \in \mathcal{A}} \pi(a|s, \theta) Q_\pi(s, a) \\ \nabla J(\theta) &= \sum_{s \in \mathcal{S}} d(s) \sum_{a \in \mathcal{A}} \nabla \pi(a|s, \theta) Q_\pi(s, a) \\ &= \sum_{s \in \mathcal{S}} d(s) \sum_{a \in \mathcal{A}} \pi(a|s, \theta) \frac{\nabla \pi(a|s, \theta)}{\pi(a|s, \theta)} Q_\pi(s, a) \\ &= \sum_{s \in \mathcal{S}} d(s) \sum_{a \in \mathcal{A}} \pi(a|s, \theta) \nabla \ln \pi(a|s, \theta) Q_\pi(s, a) \\ &= \mathbb{E}_{\pi_\theta} [\nabla \ln \pi(a|s, \theta) Q_\pi(s, a)] \end{aligned} \quad (6.16)$$

and finally, we get policy gradient theorem as

$$\nabla J(\theta) = \mathbb{E}_{\pi_\theta} [\nabla \ln \pi(a|s, \theta) Q_\pi(s, a)] \quad (6.17)$$

Since probabilities of each actions are not computed,policy gradient methods are suitable for continuous action space.

6.2.2 Proximal Policy Optimization (PPO)

Proposed by John et. al. PPO[2] which optimizes a clipped/surrogate objective function using stochastic gradient ascent. In this method multiple epochs of mini batch updates are used instead of one update per batch. Let consider probability ratio of old and new policies as:

$$r(\theta) = \frac{\pi_\theta(a|s)}{\pi_{\theta_{old}}(a|s)} \quad (6.18)$$

then objective function of TRPO¹ is reduced to

$$J^{TRPO}(\theta) = \mathbb{E}[r(\theta)\hat{A}_{\theta_{old}}(s, a)] \quad (6.19)$$

if distance between θ_{old} and θ is not limited, extremely large parameter updates will be made to optimize $J^{TRPO}(\theta)$, leading to instability. In PPO $r(\theta)$ is bounded close to $1 \pm \epsilon$, here ϵ is hyperparameter and minimum of either same objective or clipped objective is selected.

$$J^{CLIP}(\theta) = \mathbb{E}[\min(r(\theta)\hat{A}_{\theta_{old}}(s, a), \text{clip}(r(\theta), 1 - \epsilon, 1 + \epsilon)\hat{A}_{\theta_{old}}(s, a))] \quad (6.20)$$

ratio $r(\theta)$ is clipped between $1 - \epsilon$ and $1 + \epsilon$ as shown in Figure 6.3 surrogate $J^{CLIP}(\theta)$ as function of probability ratio r for one step starting from $r = 1$. since ratio is clipped and does not vary rapidly large policy updates are skipped hence increasing stability. algorithm 1 is actor critic style parallel implementation of PPO.

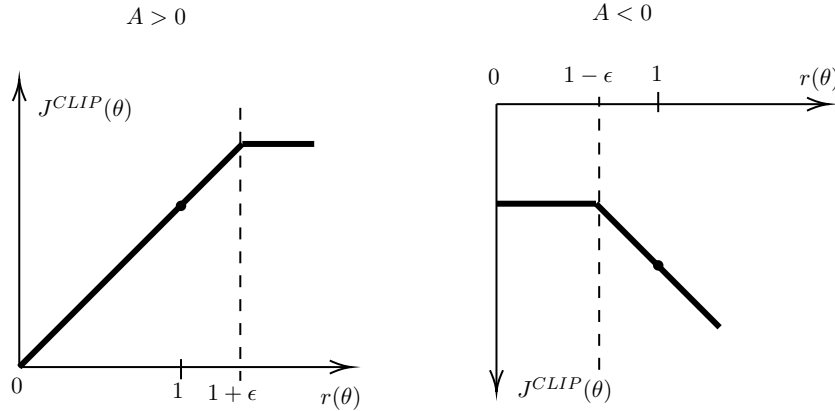


Figure 6.3. Surrogate $J^{CLIP}(\theta)$ as function of probability ratio for positive (left) and negative (right) advantage, figure reconstructed from original paper. [2]

¹Trust Region Policy Optimization[39] avoids parameter updates that change the policy rapidly

Algorithm 1: PPO,Actor-Critic Style

Result: Write here the result

```

for iteration=1,2,... do
    for actor=1,2,...,N do
        | Run policy  $\pi_{\theta_{old}}$  in environment for  $T$  time steps.
        | Compute advantage estimates  $\hat{A}_1, \dots, \hat{A}_T$ 
    end
    Optimize surrogate  $L$  wrt  $\theta$ , with  $K$  epochs and minibatch size  $M \leq NT$ 
     $\theta_{old} \leftarrow \theta$ 
end

```

6.3 Neural Network

Neural networks were first introduced in 1944 by Warren McCullough and Walter Pitts. Inspired by human brain neural networks are large graphs made up of densely connected processing nodes. These processing nodes are referred as neurons, It may take multiple inputs and produce one output. Each input x_i is associated with some weight w_i , neuron produces weighted sum of inputs adds bias to it and squeezes the results with pre-selected activation function. As shown in Figure 6.4 neuron functions as

$$y_{out} = f(b + \sum_{i=1}^n x_i w_i) \quad (6.21)$$

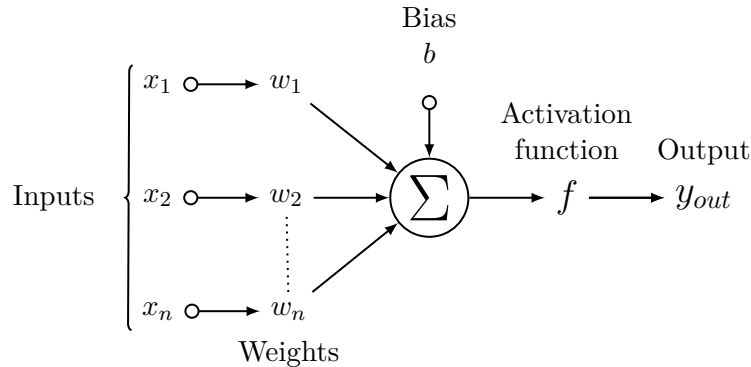


Figure 6.4. Components of individual Neuron. The activation function is denoted by f and applied on the weighted sum of inputs with added bias

Activation function is basically squeezing of weighted sum in to some allowable values, sometimes activation can be just a trigger which occurs after reaching decided threshold. Shapes of commonly used activation functions are shown in Figure 6.5. Apart from its shape most important property of activation function is its derivative which has crucial role for training a neural network. Few commonly used activation functions are mentioned in Table 6.1

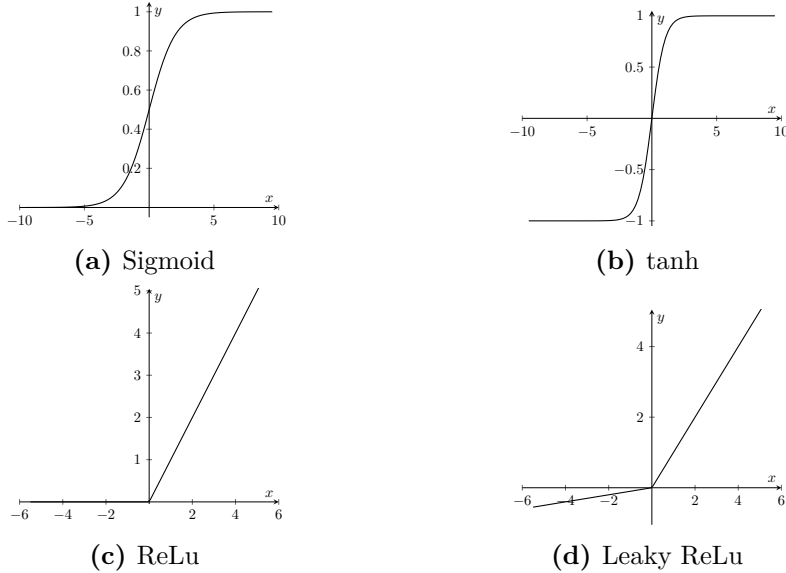


Figure 6.5. Commonly used activation functions

Activation Function	Function $f(z)$	Derivative $f'(z)$
Sigmoid	$f(z) = \frac{1}{1 + e^{-z}}$	$f'(z) = f(z) \cdot (1 - f(z))$
Tanh	$f(z) = \frac{e^z - e^{-z}}{e^z + e^{-z}}$	$f'(z) = 1 - \tanh(z)^2$
Linear	$f(z) = z\alpha$	$f'(z) = \alpha$
Exponential Linear Unit (ELU)	$f(z) = \begin{cases} z & z > 0 \\ \alpha(e^z - 1) & z \leq 0 \end{cases}$	$f'(z) = \begin{cases} 1 & z > 0 \\ \alpha e^z & z \leq 0 \end{cases}$
Rectified Linear Units (ReLU)	$f(z) = \begin{cases} z & z > 0 \\ 0 & z \leq 0 \end{cases}$	$f'(z) = \begin{cases} z & z > 0 \\ 0 & z \leq 0 \end{cases}$
LeakyRelu	$f(z) = \begin{cases} z & z > 0 \\ \alpha z & z \leq 0 \end{cases}$	$f'(z) = \begin{cases} z & z > 0 \\ \alpha & z \leq 0 \end{cases}$
Arctan	$f(z) = \tan^{-1}(z)$	$f'(z) = \frac{1}{1 + z^2}$
Swish	$f(z) = \frac{z}{1 + e^{-z}}$	$f'(z) = \frac{f(z)(1 - f(z))}{1 + e^{-z}}$
Soft Plus	$f(z) = \ln(1 + e^z)$	$f'(z) = \frac{1}{1 + e^{-z}}$

Table 6.1. Commonly used activation functions and their derivative

6.3.1 Multi Layer Perceptron policy

Multi Layer Perceptron is a complex network of perceptrons connected based on various architectures. Most common method is feed forward neural network. Neurons are grouped in a single stage called a layers. Every unit in a layer is connected to all units of previous layers. Three distinct layers are Input, Hidden and Output. Data enters from input and passes thorough hidden layers finally emitted from output

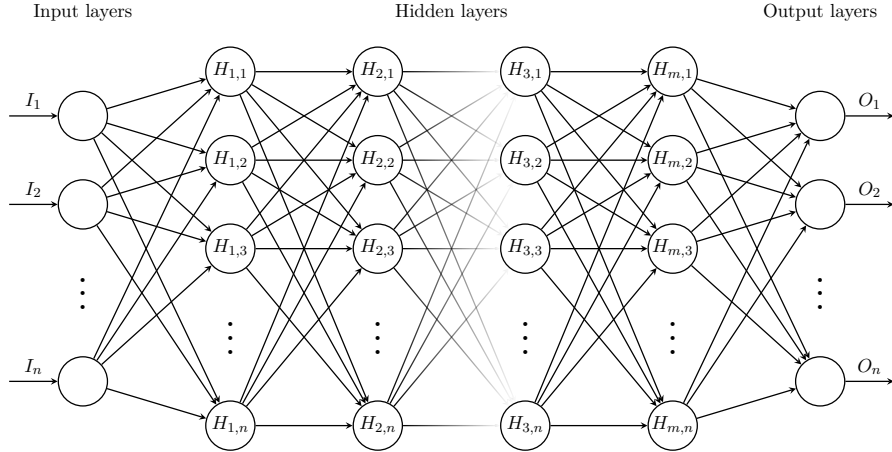


Figure 6.6. Multi Layer Perceptron

layer. Hidden layers are not accessible to external world hence the name. Shallow neural network has one hidden layer as opposed to Deep neural networks, which may have multiple hidden layers, an example shown in Figure 6.6. With properly chosen weights, Neural network can approximate any nonlinear function. Process of finding weights is called training an iterative process where data is passed from input layer and based on error between evaluated and expected output weights are updated in backward direction layer by layer, process referred as propagation. Lets recall operation of each neuron with n inputs.

$$\hat{y} = f_{act}(b + W_{n \times 1}^T X_{n \times 1}) \quad (6.22)$$

$$\hat{y} = f_{act}(\vec{w} \cdot \vec{x} + b)$$

for input vector \vec{x} error between output \hat{y} and expected output y can be computed using Mean Square Error (MSE) for set of N input output pair $X = \{\vec{x}_i, y_i\}, i \in \{1, N\}$ as:

$$E(X) = \frac{1}{2N} \sum_{i=1}^N (\hat{y}_i - y_i)^2 = \frac{1}{2N} \sum_{i=1}^N (f_{act}(\vec{w} \cdot \vec{x}_i + b) - y_i)^2 \quad (6.23)$$

Objective of training is to minimize the error $E(X)$ which can be done with gradient descent

$$\begin{aligned} \vec{w}_{i+1} &= \vec{w}_i - \alpha \frac{\partial E(X)}{\partial \vec{w}_i} \\ b_{i+1} &= b_i - \alpha \frac{\partial E(X)}{\partial b_i} \end{aligned} \quad (6.24)$$

Here α is learning rate, typically a small value the weight deviation $\Delta \vec{w} = \vec{w}_{i+1} - \vec{w}_i$ bias deviation $\Delta b = b_{i+1} - b_i$ for iteration is calculated as:

$$\begin{aligned}\Delta \vec{w} &= \frac{1}{N} \sum_{i=1}^N \alpha(\vec{y}_i - \hat{y}_i) f'_{act}(\vec{w} \cdot \vec{x} + b) \vec{x}_i \\ \Delta b &= \frac{1}{N} \sum_{i=1}^N \alpha(\vec{y}_i - \hat{y}_i) f'_{act}(\vec{w} \cdot \vec{x} + b)\end{aligned}\quad (6.25)$$

6.4 Neural Network based VSCMG steering Law

Starting with fundamentals discussed in earlier sections, a neural network is trained to solve problem of VSCMG steering. Idea is, for required torque at particular state of spacecraft, what signals should be given to the gimbal and flywheel motors are evaluated from neural network described in Figure 6.7.

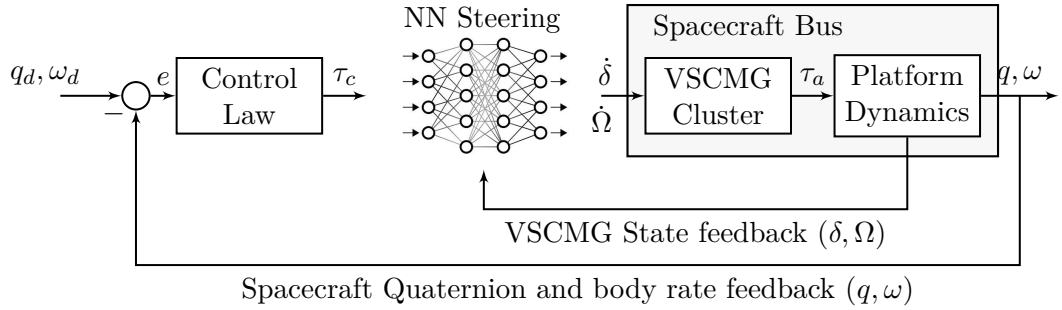


Figure 6.7. Neural Network based VSCMG Spacecraft Steering and Control Architecture

6.4.1 Reinforcement Learning Agent

As previously reported Reinforcement Learning based strategy has an “Agent” learns a policy in this case a MLP policy by interacting with environment in order to maximize the received reward. The observation space of agent is states that agent can precept and action space is actuators that agent can act on. MLP policy is designed such a way that input layer is observation space and output layer is action space. In order to train the model a critic network is required, input layer of critic is sum observation space and action space while only one output.

6.4.2 Training Procedure

With regard to Figure 6.8 a custom environment with complete VSCMG dynamical equation of motion stepper compatible with OpenAI Gym [40] is developed in python. This environment evolves predefined time-step at each call, although time-steps considered are order of magnitude of milliseconds environment takes multiple intermediate time-steps based on adaptive Runge–Kutta Cash–Karp method in order to preserve accuracy of numerical integration. After integrating for one step environment returns observations, action, reward and few status parameters for

monitoring learning process. It is realised that python based Ordinary Differential Equation (ODE) integrator is slow and knowing the fact that simulation time must be in magnitude of millions of seconds, entire equation of motion is developed in C++ with Boost library [41] for high performance ODE integrator. The developed Dynamical Linked Library (DLL) has exported interface with python consequently increasing performance and speed of simulation. Tensorflow and Open Source machine learning library has been used to train the agent. Along with plots of system states, OpenGL based real time 3D visualization of VSCMG is devolved in order to have better understanding of system dynamics. Some core components of VSCMG Environment are

6.4.3 Observation Space

Choice of observation can be a vector of states comprising quaternion error, body rate error, RW velocities and gimbals angles. Since outer loop is of control remains same, for steering law observation which is input layer of policy layer is selected as vector comprising demand torque, gimbal angles and RW velocities. This reduced length observation space from 15 to 11, keeping information of attitude error and rate error in the form of required torque. Selecting reduced observation space also played important role for reduction in storage requirements. Since for supervised learning, large amount of trajectory with input output pairs need to be stored.

$$s_{11 \times 1} = \begin{pmatrix} \tau_c \\ \dot{\delta} \\ \Omega \end{pmatrix} \quad (6.26)$$

6.4.4 Action Space

All Reaction wheel angular accelerations, and gimbal velocities are considered as action space which is output layer of Policy network.

$$a_{8 \times 1} = \begin{pmatrix} \ddot{\delta} \\ \dot{\Omega} \end{pmatrix} \quad (6.27)$$

here gimbal velocity and angular acceleration bounded by actuator limit within $\dot{\delta}_{4 \times 1} \in [-5, 5] \text{ rad/sec}^2$ and $\dot{\Omega}_{4 \times 1} \in [-30, 30] \text{ rad/sec}$

6.4.5 Reward Function

Selection of reward function is crucial process, with a good reward function agent quickly learns policy, with bad reward function, may stuck in to local maxima. Perhaps agent finds certain sequence of action which might not be the solution but still prefers since it is increasing reward. although there is no general method to find best reward function and it is chosen based on information about system with few iteration of trial and error. An example of torque based reward function with distance to singularity is shown below gives tendency to move away from singularities.

$$\begin{aligned}
R = & k_0 \exp(-\tau_c^T \tau_c) \\
& + k_1 \det(QQ^T) \\
& + k_2 \ln(\det(CC^T)) \\
& + k_3 \ln(\det(DD^T))
\end{aligned} \tag{6.28}$$

with k_1, k_2 and k_3 are positive constants to weight distance from VSCMG, CMG and RW singularities.

6.5 Training

Initially trajectories of state action pairs are generated using Monte-Carlo Simulation of VSCMG based steering law (expert agent) for 3000 episodes with 1000 steps of time $\Delta t = 0.01sec$ each eposode starting with random initial states and attitude error. Supervised learning implementation using Tensorflow [42] an Open Source library to develop and train ML library is used to pretrain the agent in order to reduce training time. Pre trained model is later trained with PPO algorithm shown in Figure 6.8 with hyper parameters configuration set as Table 6.2. Apart from 11 neurons in input and 8 neurons in output Policy network has 7 fully connected hidden layers having architecture of neurons in each layer as [32,64,64,64,64,32,16] with tanh activation hence total of 355 Neurons in a policy. Value function has same hidden layer configuration as policy network but 19 neurons in input layer (11 observations and 8 actions of policy layer) and only one neuron in output layer making total of 356 neurons in value network.

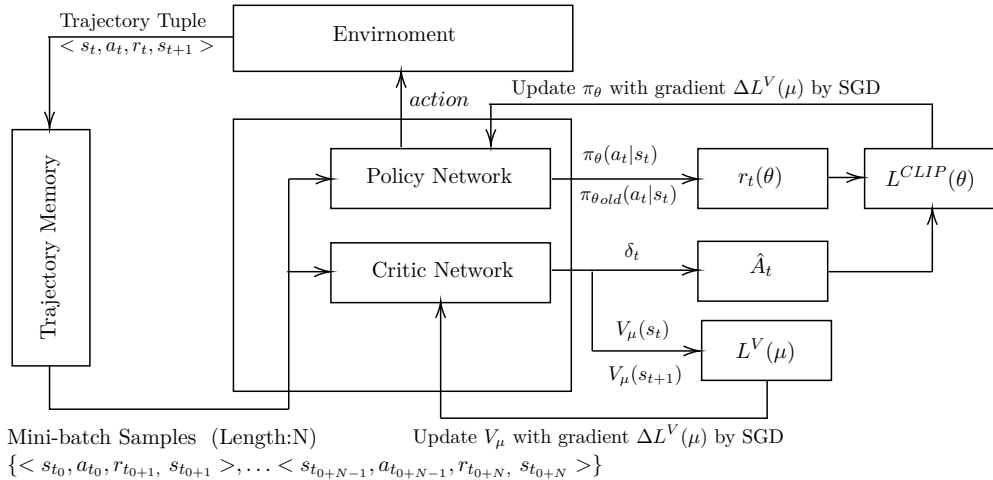
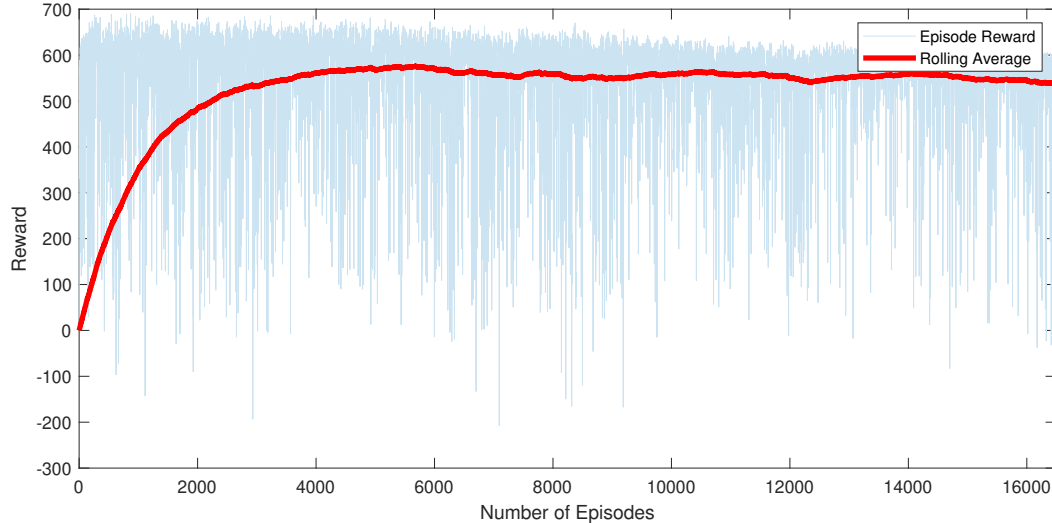


Figure 6.8. Flowchart of actor critic based PPO learning model [3]

Hyper-parameter	Value
Clipping parameter (ϵ)	0.2
Optimization algorithm	Adam
Learning rate (η_μ, η_θ)	0.0001
Discount factor (γ)	0.99
The number of steps to run for each environment per update	1000
Entropy coefficient for the loss calculation	0.01
Number of training mini batches per update	4

Table 6.2. PPO Algorithm Hyper-parameter configuration

After pre training, model is trained for $16 \cdot 10^6$ time steps with 1000 steps per episode using PPO algorithm. Figure 6.9 shows reward per episode and rolling average. Notice how model learned within 5000 episodes, and later reward is saturated within 500 to 600.

**Figure 6.9.** Averaged episode reward for 16000 episodes of PPO training

6.5.1 Test Results

Let us consider a test case, Neural Network based steering has to cancel attitude error in terms of Euler angles $\phi, \theta, \psi = [-179, -37, 140]$ deg considering initial and final state shown in Table 6.3

Parameter	Value	Unit
q	$[0.3036 \quad 0.3228 \quad -0.8891 \quad -0.1146]^T$	-
ω	$[0 \ 0 \ 0]^T$	deg / sec
q_d	$[1 \ 0 \ 0 \ 0]^T$	-
ω_d	$[0 \ 0 \ 0]^T$	rad/ sec
δ	$[-0.7729 \quad 1.2424 \quad 0.6058 \quad 2.6412]^T$	rad
Ω	$[0 \ 0 \ 0 \ 0]^T$	rad/ sec

Table 6.3. Initial and desired states for Attitude error tracking with Neural Network based VSCMG steering Law

Results of error canceling maneuver using Neural network based steering are in Figure 6.10 to Figure 6.14. Being long slew maneuver, initial attitude error was large as consequence large demand torque variation can seen in first few seconds although after 10 seconds.

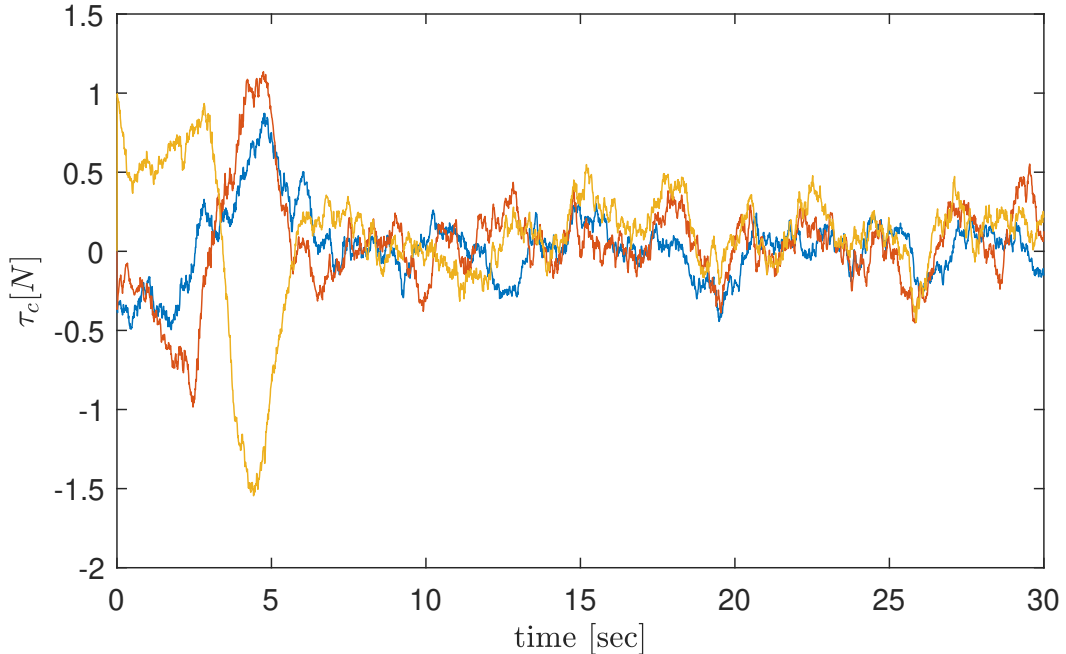


Figure 6.10. NN based steering: Required torques

Variations in reaction wheels spins are more than that compared to gimbal angles, hence we can infer neural network has prioritized RWs over CMGs for this maneuver.

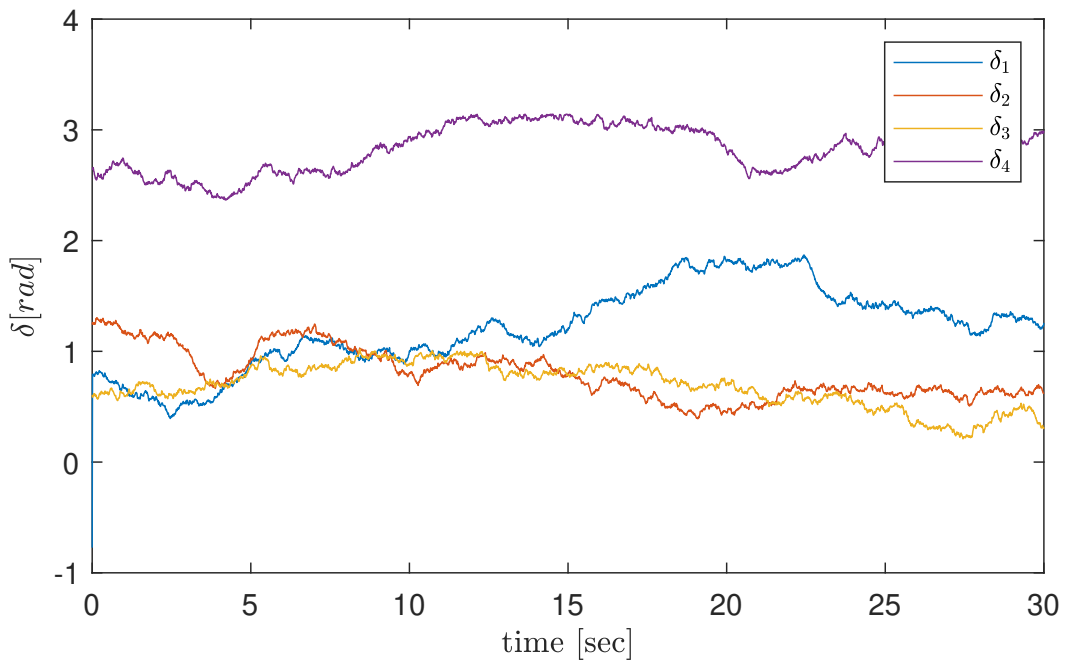


Figure 6.11. NN based steering: Gimbal angles

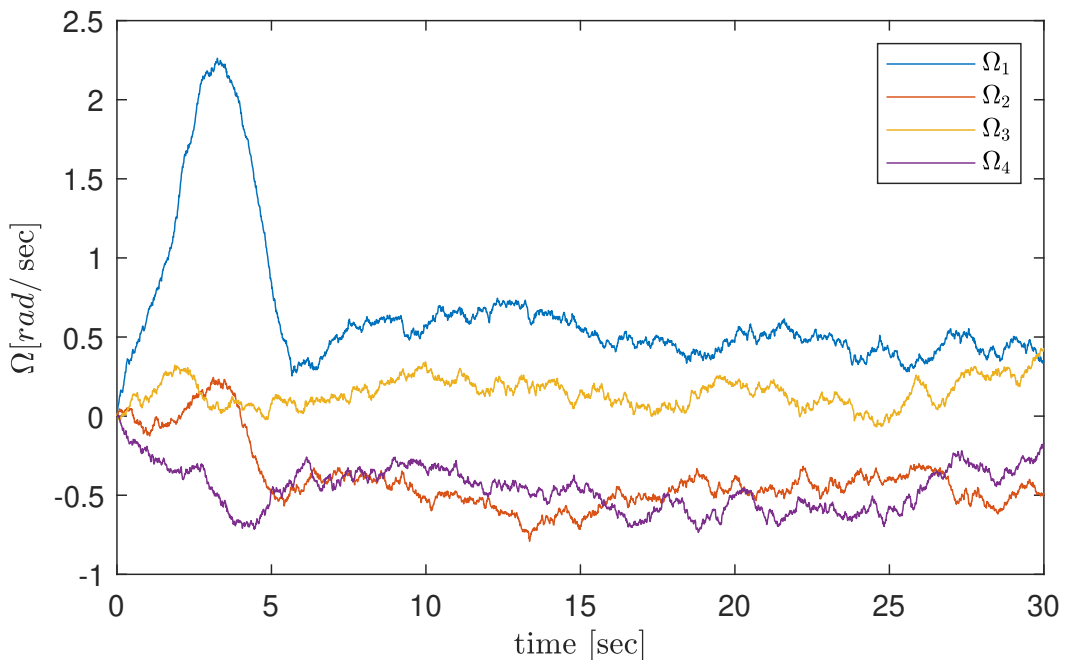


Figure 6.12. NN based steering: RW velocities

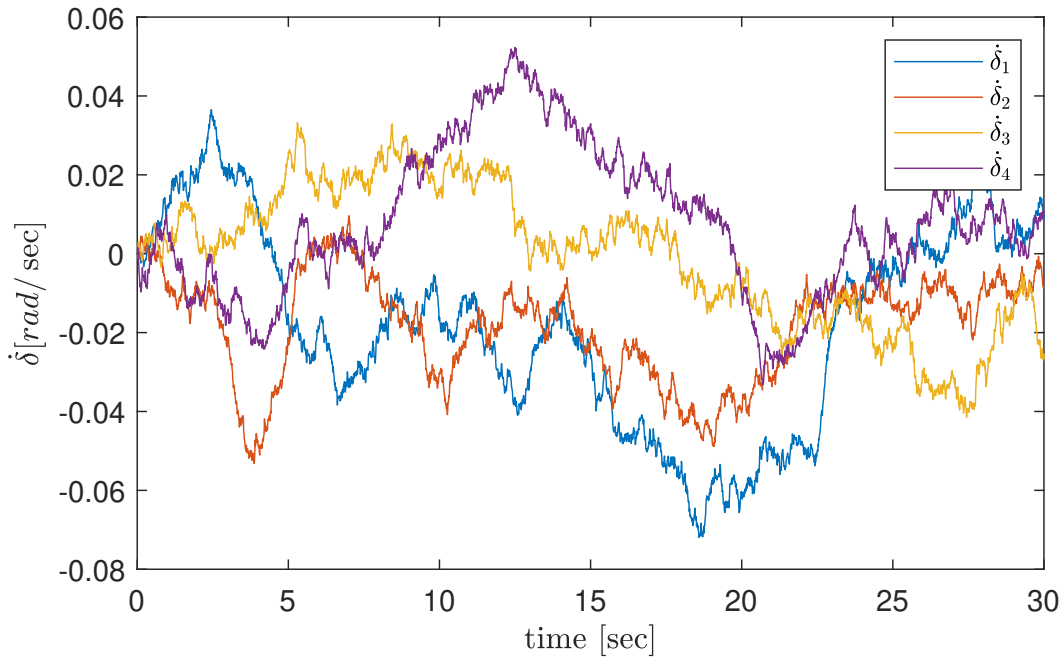


Figure 6.13. NN based steering: Gimbal Velocities

Figure 6.13 and Figure 6.14 are control action performed by agent. Notice order of magnitude of RW accelerations and gimbal velocities are within permissible range and no large variation occurred.

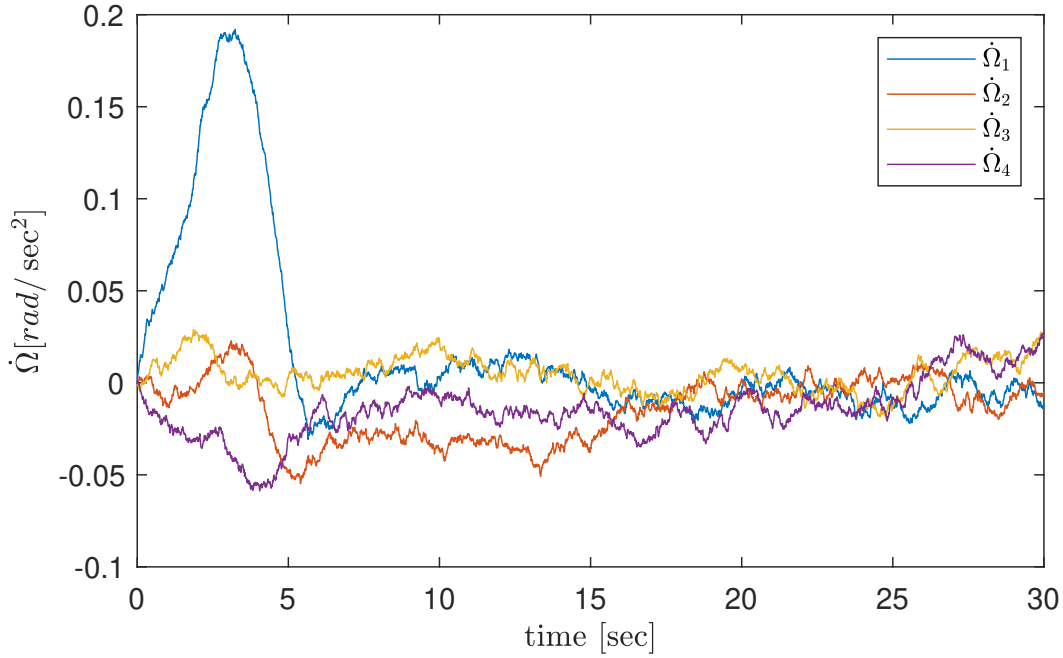


Figure 6.14. NN based steering: RW Accerlations

Output data of neural network can be amplified or attenuated based on steady state requirements, moreover different activation functions at output layer can be used.

A GUI based script is developed in order to monitor states and 3d visualization of VSCMG. Screenshot of testing trained PPO model is shown in Figure 6.15. Main advantage of script is along with plots, attitude command and other model related parameters can be updated in real time, giving user an option for better calibrating the ACS according to required performance.

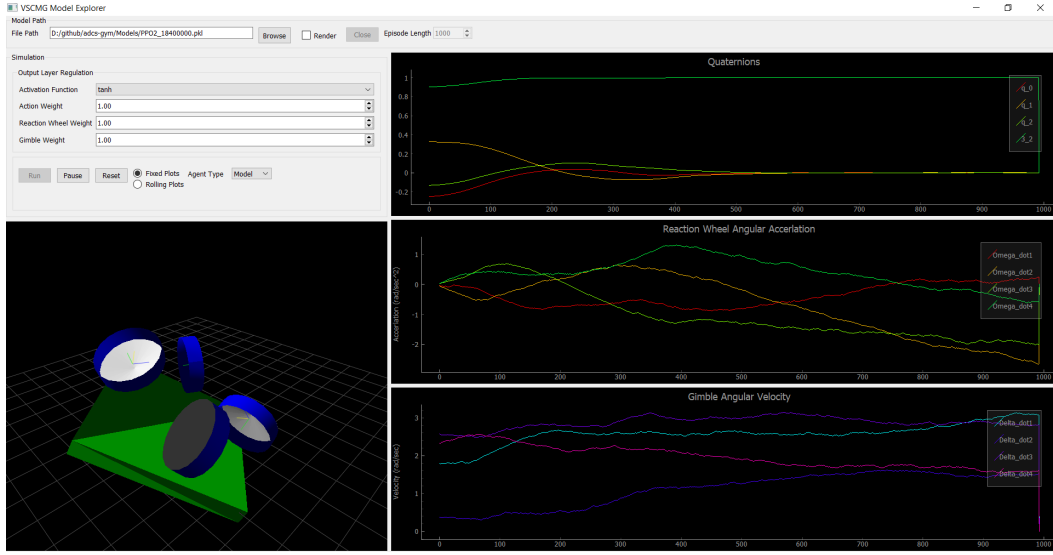


Figure 6.15. VSCMG Model and expert agent Testing GUI

6.6 Comparison of Neural Network and SR-VSCMG Steering Law

Following discussion assumes regulation maneuver with initial attitude error of 90° in yaw angle has to be canceled. In order to evaluate the performance of steering law, spacecraft actuators are deliberately kept in singular states as shown in Table 6.4. Notice angular momentum of all reaction wheels is zero, moreover required torque is orthogonal to CMG torque axis.

Parameter	Value	Unit
q	$[1 \ 0 \ 0 \ 0]^T$	-
q_d	$[0.7071 \ 0 \ 0 \ 0.7071]$	-
ω_d	$[0 \ 0 \ 0]^T$	rad/sec
δ	$[0, \ 0, \ 0, 0]^T$	rad
Ω	$[0, \ 0, \ 0, 0]^T$	rad/sec
K_w	4.4	-
K_q	10.1	-

Table 6.4. Simulation parameters for regulation maneuver in order to cancel attitude error of 90° in yaw angle.

Results of Neural Network based and Singularity-Robust VSCMG Steering Law (SR-VSCMG) are concurrently simulated using specially developed Model Explorer

software Figure 6.15 discussed in earlier section. Quaternions of simulation with neural network based steering are shown in Figure 6.16a and Singularity-Robust VSCMG Steering Law shown in Figure 6.16b. Notice that with NN based steering quickly approaches desired state within 5 seconds but a small steady state error persists, whereas with SR-VSCMG steering, slight overshoot is seen followed by long period osculation near desired state. Notice that with same control gains NN based steering quickly stabilizes and follows different trajectory than SR-VSCMG steering law. As shown in Figure 6.17 small variation in body rates are visible in other two axis since NN based steering is following slightly different trajectory than SR-VSCMG for which variation in body rate is only along yaw axis. Even after approaching close to desired state small but significant amount of variations are persistent in all three body rates.

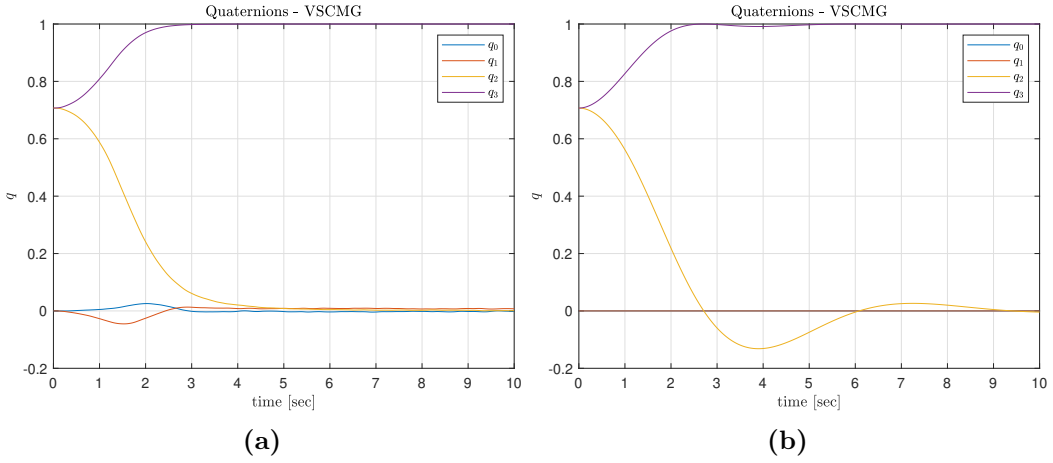


Figure 6.16. Attitude quaternions : (a) Neural Network based steering (b) SR-VSCMG steering

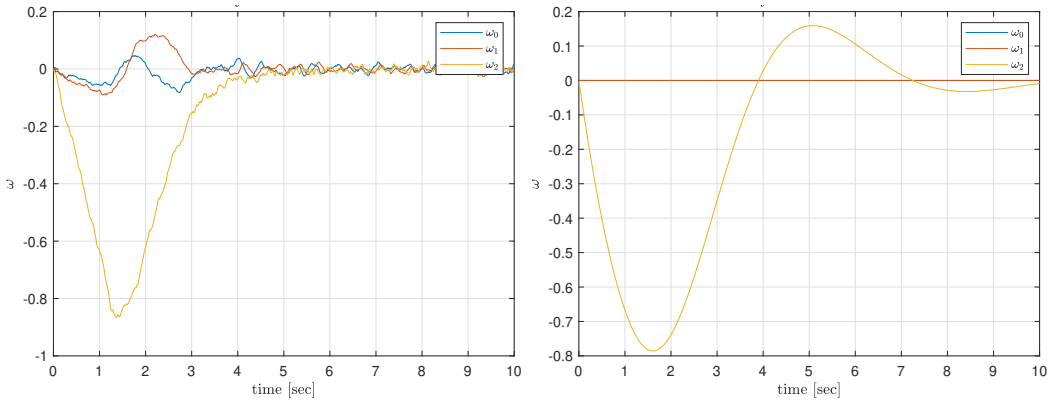


Figure 6.17. Body rates (rad/sec): (a) Neural Network based steering (b) SR-VSCMG steering

Each reaction wheel wheel is running at slightly different angular velocity in case of NN based steering, in fact this is the reason we can observe slightly different

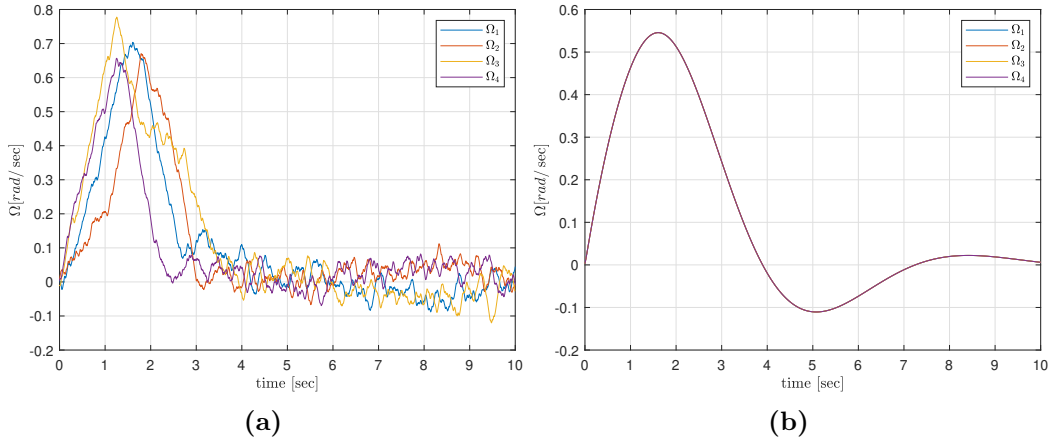


Figure 6.18. Reaction wheel angular velocity : (a) Neural Network based steering (b) SR-VSCMG steering

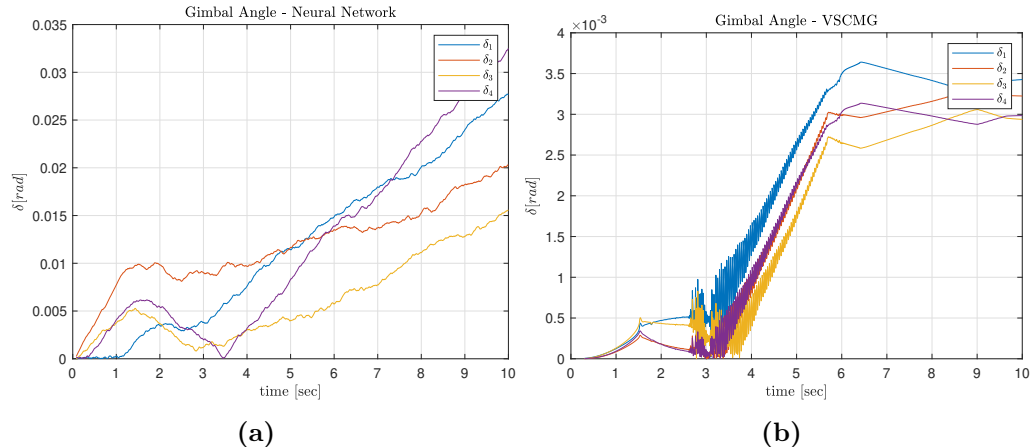


Figure 6.19. Gimbal Angle : (a) Neural Network based steering (b) SR-VSCMG steering

path followed than shortest path as in case of SR-VSCMG steering. Most significant difference is seen in Gimbal Angles, comparison is shown in Figure 6.21. Very high frequency jitter is clearly visible in ?? since CMGs are very close to singularity, whereas in the case of Figure 6.21a even in the proximity of singularity no high frequency contents are visible. Considering structural integrity of system Neural network based steering performs better near singular state. Figure 6.20 depicts three types of singularities. System becomes singular in case of rank deficiency that is transformation matrix is no longer full rank and hence non invertible. Degree or closeness to singularity can be measured with taking determinant of matrix. Here CMG singularity measure $m_c = \det(CC^T)$, Reaction wheel singularity measure measure $m_s = \det(DD^T)$ and complete VSCMG singularity measure measure $m_{vscmg} = \det(QQ^T)$ is shown in Figure 6.20. CMGs are in singular state at the beginning since all reaction wheels are at rest. As angular momentum of RW is increased CMGs are getting away from singular state. Notice that in case of NN based steering distance from singularity is much higher at maximum RW angular

momentum. Measure of RW remains constant in case of SR-VSCMG steering law since only RWs are used throughout the maneuver and gimbal angle remains constant. Whereas in case of NN-Steering, reaction wheel are moving far away from singularity due to variation in gimbal angle. Another contributing factor for increased in singular distance of RW singularity is different angular momentum of RWs.

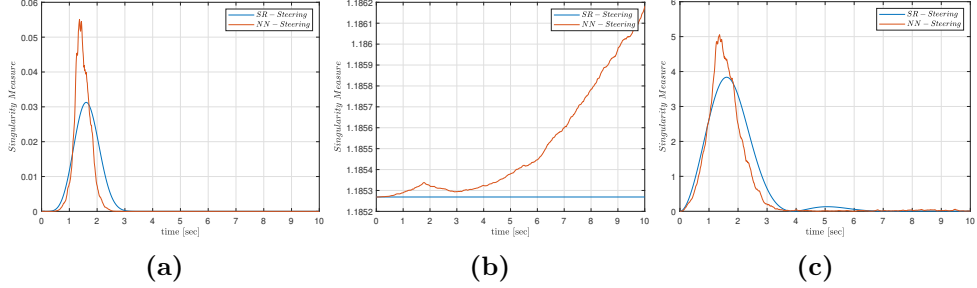


Figure 6.20. System approaches singular state as singularity measure tends to zero (a) CMG singularity; (b) Reaction Wheel singularity and (c) VSCMG singularity

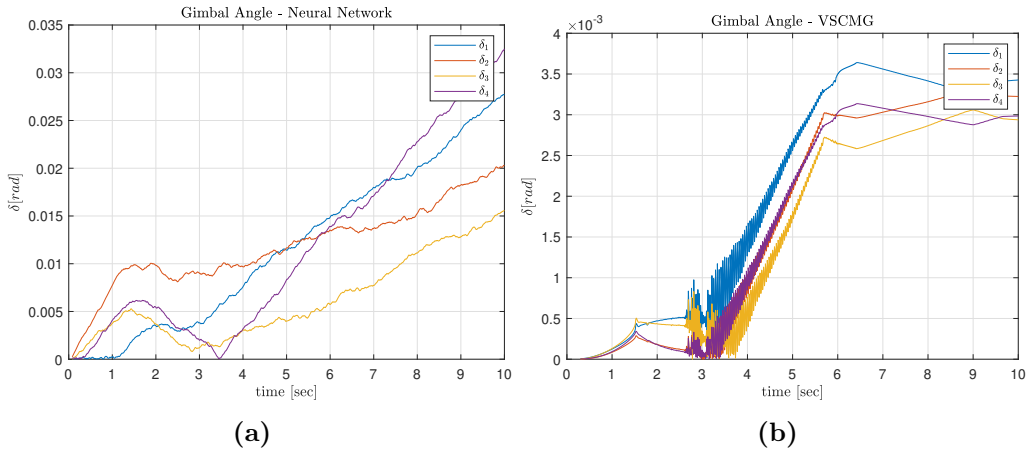


Figure 6.21. CMG gimbal angles : (a) Neural Network based steering (b) SR-VSCMG steering

Multiple simulations keeping same scenario are performed considering both NN based and SR-VSCMG based steering law. For above maneuver of 10 seconds, SR-VSCMG based steering law requires average of 3.82 seconds to complete entire simulation whereas neural network based steering requires 2.16 seconds on intel i7 processor. Processing time is reduced by 1.66 seconds which is clear computational advantage provided by proposed steering law. From above results it is clear that SR-VSCMG steering law provides more precise attitude tracking performance, although Neural network based steering is better at quickly approaching desires state following different trajectory with maintain body in allowable range. Most important advantage of proposed technique is seen in proximity of singularity. SR-VSCMG based steering undergoes very high frequency jitter which not favourable considering structural integrity of spacecraft. NN based steering is inversion free technique thus very large velocities are not present in proximity of singularity. Steady state error

and body rate oscillations in proximity of desired state can be reduced by regulating output layer by appropriate activation such as softmax and by filtering the output in order provide smooth actions to actuators. After numerous Monte Carlo simulations it is observed that NN based agent always converges to desired states but may follow trajectories which are not intuitive or similar to SR-VSCMG law. NN performance can be improved by more training and selecting better reward function crafted for required performance. A Hybrid of both steering law can be used, NN based steering for large slew maneuvers when error is large and SR-VSCMG based steering when current state is in proximity of desired state i.e. when error is small.

Chapter 7

Mechanical Design

In this section brief description of VSCMG test-bed mechanical design is described. Various manufacturing techniques has been employed and design choices are made in order to make sure simplicity and keeping overall cost within affordable range.

7.1 System Overview

Test bed is designed in order to simulate attitude control system of satellite equipped with momentum exchange device. A re-configurable and modular designed is realised so that various arrangements of Reaction Wheel, CMG configurations could be tested with minimum modification. Primary design consist of four SGCMG units arranged in pyramid configuration on sandwich of two acrylic sheets as main platform to hold entire electronics and power system. This platform is balanced on sharp pin keeping center of gravity of entire unit below but close to pin point. This pin joint allows complete 360 degree of rotation around yaw axis as well as ± 60 deg in roll and pitch axis constraining translation motion. Selected degree of freedom is sufficient for most of the GNC verification requirements. Entire assembly is balanced on tip placed on a small custom made tripod, a rendered view of test bed is shown in 7.1



Figure 7.1. VSCMG Attitude Control System test bed Assembly

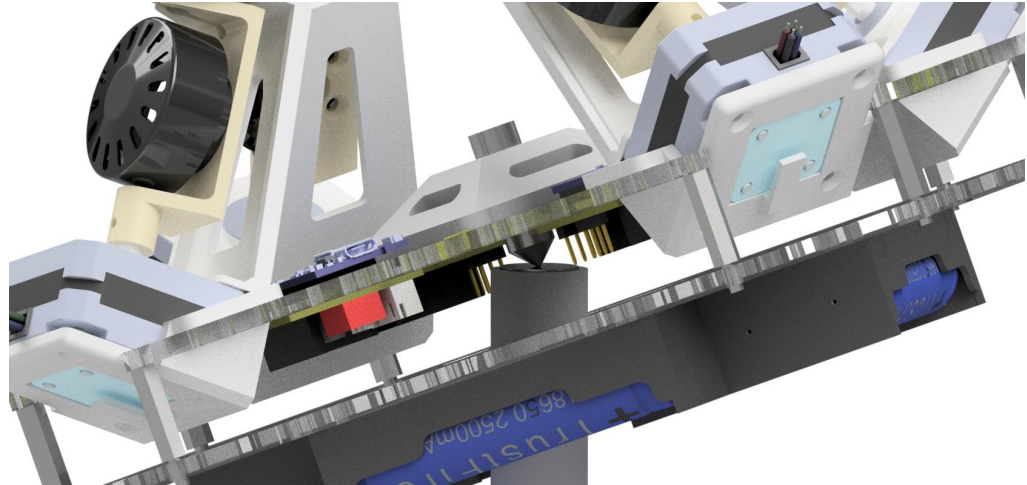


Figure 7.2. VSCMG Attitude Control System placed over tripod with sharp tip being only point of contact

7.2 Reaction Wheel Motor

Three phase permanent magnet Brushless DC (BLDC) outrunner motor is selected for reaction wheel. As name suggest brushless motor does not have brush contact for electric power and needs special commutation sequence in order to properly operate at desired torque and speed explained in next chapter. These are highly efficient and provide greater torques compared to brushed dc motors [43]. Outrunner motor has external rotor casing with attached permanent magnets and inner stator with three phase coil winding. Very low cost high RPM and High rotor inertia BLDC motors found shown in Figure 7.3 which can rotate at 900 RPM/Volt and has with inertia 3.140kg mm^2 evaluated using CAD software. This configuration is suitable for ACS testbench requirements.

7.3 Gimbal Motor

From numerical simulations performed in earlier chapters it is noted that gimbal motor speed is relatively very slow hence 4 wire stepper motor is selected as gimbal actuator. As shown Figure 7.4 is a stepper motor of 20mm length with 1.8 deg step angle [4] is used due to simplicity of control by using appropriate step sequence and ability of micro stepping in order to have precise resolution. These type of motors are available in standard form factor and in affordable cost since most of the 3d printers available in market are equipped with such motor.

7.4 Slip Ring

In order to transfer power from stationary component to rotating component slip ring is used. 6 channel slip ring is used as shown in Figure 7.5 it has 6 wires going in to large stationary part with flange and coming out from rotating end. Selected



Figure 7.3. Three phase, outrunner, Brushless DC Motor as reaction wheel

slip ring has 1A nominal current carrying capacity at maximum 300 RPM. One of the most important component needs to taken care of while designing SGCMG assembly.

7.5 SGCMG Assembly Design

In order to achieve modular design, an unit of Single Gimble Control Moment Gyroscope sub assembly is designed. Each SGCMG unit has a reaction wheel motor mounted on a gimbal attached to gimbal motor keeping reaction wheels center of mass in line with gimbal rotation axis. Since gimbal motor may perform multiple revolutions, inner motor which is reaction wheel needs to be powered such a way that power cables should not hinder and entangle due to rotations of outer gimbal motor. For this reason a power wires for reaction wheel motors are passed through slip ring which allows transmission of power supply from stationary to rotating structure. A magnetic encoder is placed behind the gimbal motor in order to have angle and angular velocity feedback from gimbal motor, an SGCMG unit is shown in. Two structural components of SGCMG fabricated with 3D printing ABS material are:

- Gimbal Motor Mount
- Reaction Wheel Mount

7.5.1 Gimbal Motor Mount

Important structural component of SGCMG is designed to support stepper motor at one end and slip ring at other end. Special attention given so that Reaction wheel mount which would be attached to gimbal motor shaft should have enough clearance to allow free rotation of Reaction Wheel Mount. Power to the reaction wheel is



Figure 7.4. Stepper motor [4]

provided through slip ring, hence a provision is made to hold slip ring with it's axis in line with gimbal motor shaft as shown in Figure 7.6. A slot at the end of mount allows proper placement of magnetic encoder in order to have feedback from stepper motor. A complete standalone SGCMG unit is shown in Figure 7.8.

7.5.2 Reaction Wheel Mount

C shaped mount is used to hold Reaction Wheel motor as shown in, BLDC motor is mounted on web of C channel. Reaction wheel mount is connected to stepper motor shaft at one end while other end is supported by rotating end of slip ring. Special attention is paid in order to connect BLDC wires from slip ring without hindering any component.

7.6 Base Platform

Central structure of test bed which shall hold together all the SGCMG units, power system and other required electronics components. Base platform consist of two acrylic plates fabricated using laser cutting as per design, sand-witched together using spacers. This type of two layer design incorporated so that most of the electronic components and PCBs can use the place between two plates. Batteries are fixed on bottom plate whereas four SGCMG units are bolted on top plate in order to bring center of mass as close to plates as possible. Entire design is kept symmetric in order to simplify manufacturing but most important mass balancing requirement. Most important requirements is the entire platform needs to be balanced on sharp tip with it's center of mass below but closer to tip. Since there will be uncertainties in mass distribution due to the fact presence of wiring and other non modeled



Figure 7.5. 6 channel Slip Ring



Figure 7.6. Gimbal Motor Mount

components we can not guaranty that CoM is at desired location. Hence a threaded Allen bolt with sharp tip is used. A 3D printed pyramid structure is mounted on top base plate. This part has threaded hole at the center in order to hold sharp cone pointed bolt. This sub assembly shown in Figure 7.10 allows variable position of pivot so that distance of center of mass from pivot along z axis can be shifted as per requirement. A small 3D printed tripod is designed on which entire base platform shall be balanced. Due to the fact that sharp tip may easily damage 3D printed structure, a steel coin is fixed on the top of tripod shaft and entire satellite platform will rest on this steel coin at the edge of tip.



Figure 7.7. Reaction Wheel Motor Mount



Figure 7.8. assembled SGCMG unit

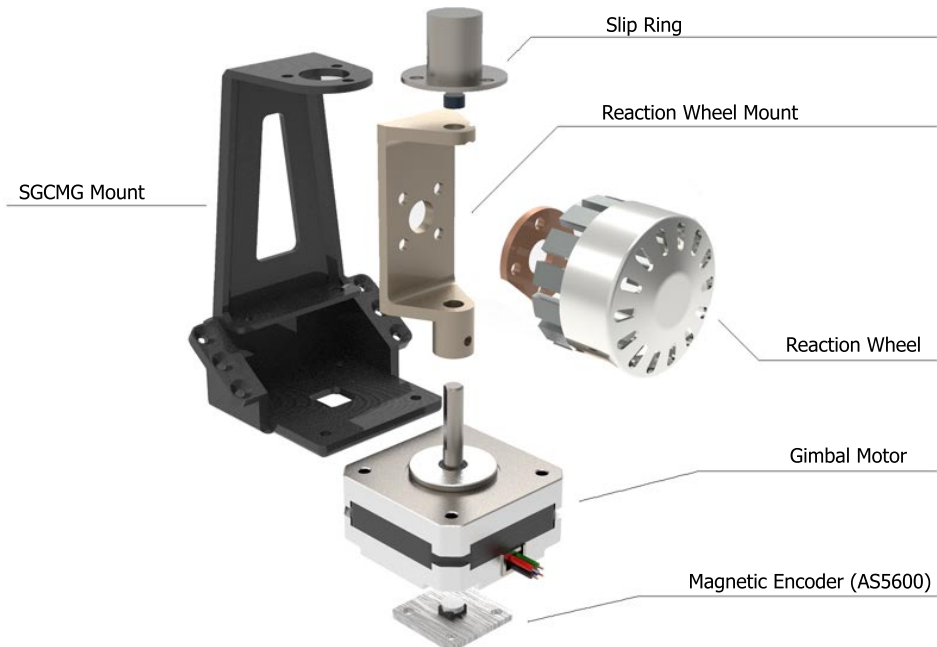


Figure 7.9. SGCMG assembly exploded view

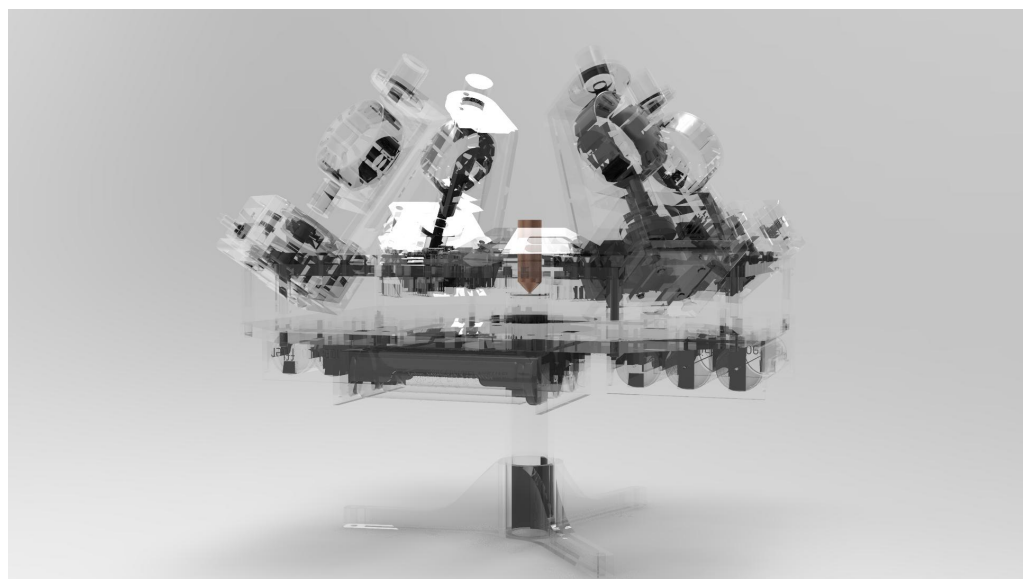


Figure 7.10. Sharp tip mounting assembly employed to minimize rotational friction with 360 degree rotational freedom in yaw axis and ± 60 deg allowed rotation in roll and pitch axis

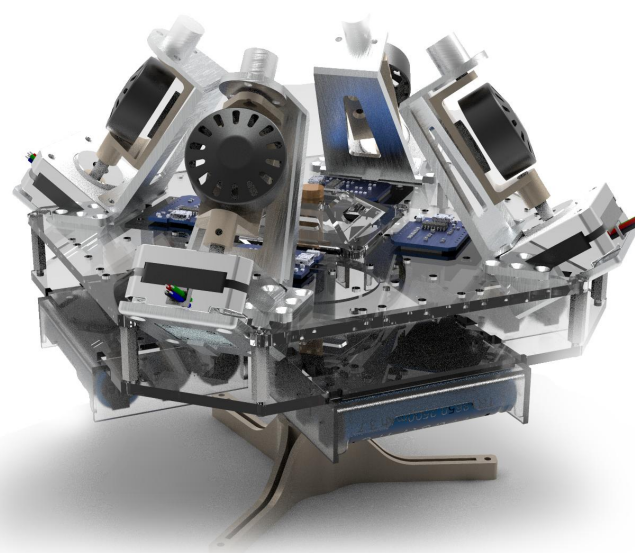


Figure 7.11. Complete VSCMG testbed Assembly Rendered view

Chapter 8

Embedded System Architecture

In this chapter electronics architecture along with communication scheme is briefly explained. Complete close loop SGCMG unit is realised. Each individual SGCMG unit consist of a three phase close loop brushless motor driver to control reaction wheel at specified angular velocity with given angular acceleration signal. Gimbal motor is driven with Stepper Motor Driver and a dedicated micro-controller which provides appropriate signal to both motor drivers. Angular velocity of gimbal motor is measured using magnetic encoder. Communication protocol is implemented such that each SGCMG unit has dedicated address and returns angular velocity of reaction wheel, angle and angular velocity of gimbal motor when input desired states are provided. Body states of platform such as attitude quaternions, angular rates are computed from 3 axis IMU with dedicated on board master micro-controller for platform. Entire testbed architecture is divided in following major subsystems:

- Platform Master State Feedback System
- Close Loop SGCMGs
- Electrical Power Systems
- Ground Control Station Server

8.1 Platform Master State Feedback System

Heart of testbench is master micro-controller has primary objective to evaluates platform orientation, body rates from an IMU and communicate in real time with Ground Control Station Server. It can also interact with other SGCMG units if VSCMG control is to be performed on board the platform.

8.1.1 Microcontroller

ESP32 an ultra low power MCU with integrated WiFi by Espressif Systems is used due to it's high performance dual core Tensilica Xtensa LX6 microprocessor running at 160 or 240 MHz, 39 GPIO and supports all standard embedded communication protocols such as 18 Analog-to-Digital Converter (ADC) channels, SPI, UART, I2C PWM output channels, Digital-to-Analog Converters (DAC) I2S interfaces etc, and requires very low power specifically 5V 100mA(Max). [44]

8.1.2 IMU

Bosch Sensortech's BNO055 shown in Figure 8.2 is 9 axis absolute orientation sensor is System in Package includes 3 axis 14-bit accelerometer, 3 axis magnetometer and 3 axis 16-bit gyroscope and 32-bit microcontroller running on board sensor fusion algorithm.[45] A custom PCB is designed in order to make sure proper and rigid placement of IMU and its interface with microcontroller. Schematic and PCB is shown in Figure 8.1 I2C protocol is used to communicate between Microcontroller Unit (MCU) and BNO055. SDA and SCL of BNO is connected to GPIO21 and GPIO22 of MCU. Firmware inside MCU is programmed in order to update and evaluate current angular velocity and orientation quaternions using Sebastian Madgwick's sensor fusion algorithm [46] and send states to Ground station at the speed of 100 Samples per seconds (100Hz).

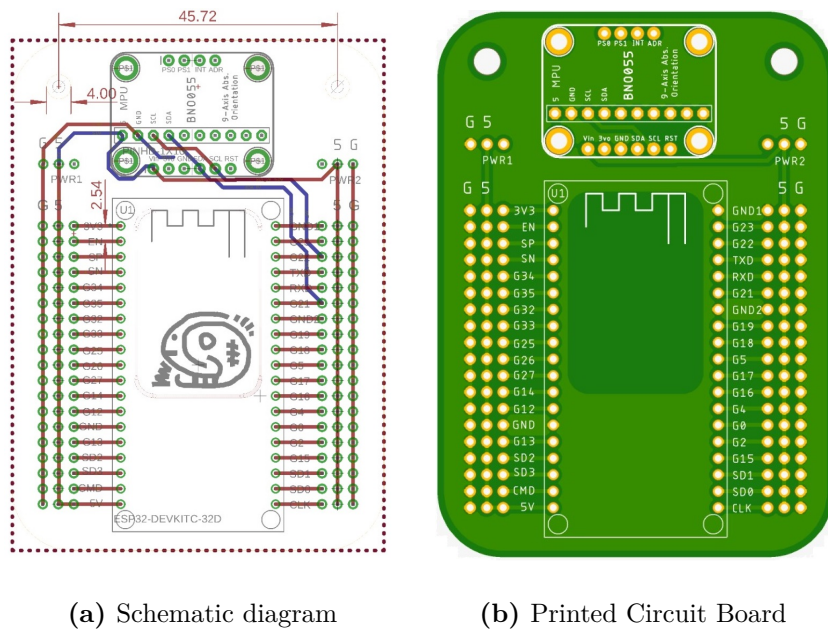


Figure 8.1. IMU interface board customized for BNO055 and ESP32.

8.2 Close Loop SGCMG

Close loop SGCMG module consist of a brushless motor as reaction wheel and stepper motor to drive gimbal. Three phase brushless motor is controlled using commercial of the shelf low cost Electric Speed Controller. ESCs are sensor less speed controllers and use back EMF to estimate rotor position in order to generate step sequence so that proper coils are energised for required angular velocity. Only drawback of sensor less ESC is, it has very high dead band that is due to the fact that at lower speed back EMF is very small hence ESC can not estimate its rotor position. 20A ESC shown in Figure 8.3 is used for this thesis. It has integrated SILABS EFM8BB21F16 MCU running at 48MHz, and N channel MOSFETs. BLHELI S open source firmware inside MCU allows bidirectional rotation of motor. It requires 50Hz



Figure 8.2. BNO055 Absolute orientation sensor consist of triaxial accelerometer, triaxial gyroscope and triaxial magnetometer with on-board 32bit MCU running sensor fusion algorithm

PWM signal with pulse width varying from 1ms to 2ms. Firmware is configured such a way that motor is at rest at 1.5ms pulse width, max angular velocity at 2ms in clockwise direction and max angular velocity in counterclockwise direction at 1ms. It has very small form factor, with particular dimensions of $23.5 \times 12 \times 4\text{mm}^3$ and weighs only 6g.

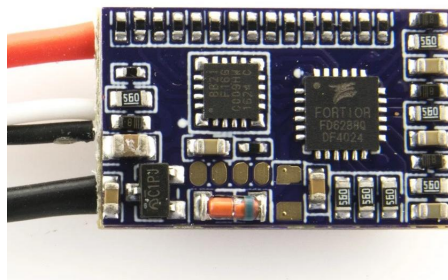


Figure 8.3. 20 A Sensorless Electronic Speed Controller

Gimbal (NEMA17 Stepper) motor should be driven with special sequence of energizing coils to advance step by step in desired direction. Polulu stepper motor shield shown in Figure 8.4 is used to control the gimbal. This shield is based on Texas Instruments DRV8825 microstepping bipolar stepper motor driver it has adjustable current limiting, over-current and over-temperature protection, and six micro stepping resolutions (up to 1/32-step). It operates from 8.2 V to 45 V and current up to 1.5A per phase.

Since stepper motor works in terms of incremental steps, there is possibility that microcontroller may miss few steps, moreover every time MCU is powered on it does not have exact angular position of stepper motor. For this reason and to have estimate of gimbal angle and angular velocity. AS5600 shown in Figure 8.5 is a 12-bit on-axis magnetic rotary position sensor is used. This contact less sensor provides analog, PWM and I2C interface. It measures absolute angle from radially magnetized on-axis magnet placed on shaft.

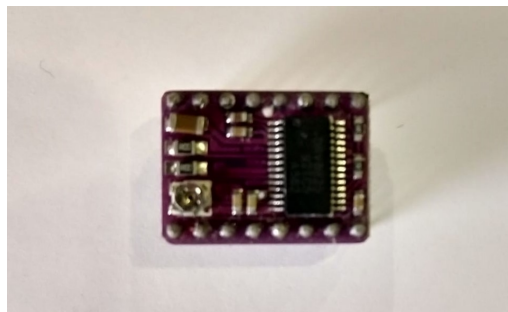


Figure 8.4. Polulu DRV8825 stepper motor driver shield

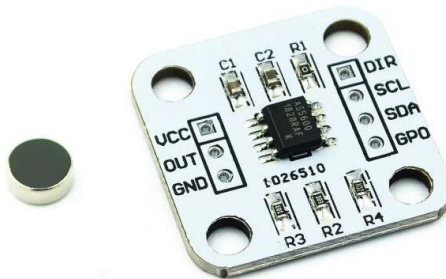


Figure 8.5. AS5600 magnetic encoder with radially magnetized magnet of 5mm diameter

Each SGCMG unit is equipped with a dedicated MCU. ESP8266 D1 Mini is selected for its small form factor precisely $34.2 \times 25.6 \times 7\text{mm}^3$ and weighs only 8.2g is powerful mini WiFi enabled board with 4MB flash based on ESP-8266EX running at 80/160MHz. It has 11 digital IO, interrupt,pwm,I2C,one-wire interface one analog input and a micro USB port to upload firmware. WiFi compatibility allows complete wireless control and monitoring of SGCMG unit in real time. Complete schematic of SGCMG unit is shown in Figure 8.6. Principle function of MCU is as follows:

- Measure angular position of gimbal using AS5600 over I2C.
- Control Gimbal motor to achieve desired angle and angular velocity as commanded.
- Generate appropriate PWM for ESC to accelerate BLDC at desired angular velocity.
- Communicate with server and report current state of gimbal angle, angular velocity and BLDC angular velocity.

8.3 Electrical Power System

Considering power requirement of different components available on platform, pack of Lithium-ion batteries is used as main power source for the complete platform. Samsung's cylindrical Li-ion cell in standard ICR18650-26F form factor has

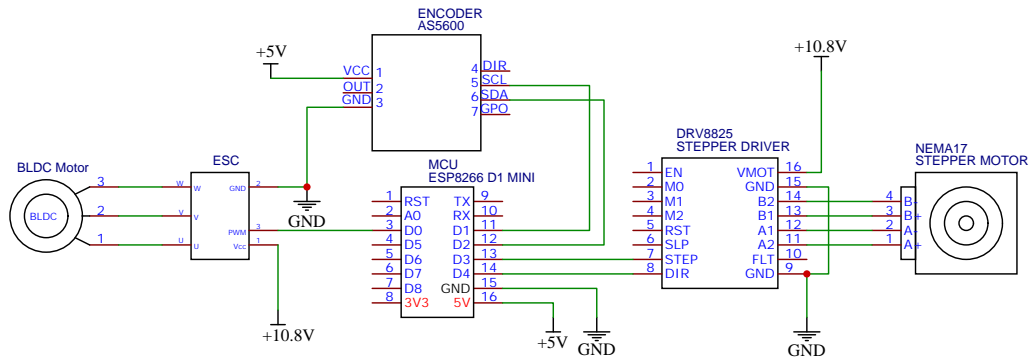


Figure 8.6. Schematic diagram of Close loop SGCMG electronics and wiring

nominal voltage 3.7V with 2.6Ah energy storage capacity moreover it can provide continuous current up to 5A and weighs 47.0 grams. Since we are using 900KV (900 RPM/V) brushless motor, with the intention of achieving required maximum angular velocity three Li-Ion cells are arranged in series accumulating total output of 11.1V. A standard 3 cell case is used to hold pack of 3 Li-ion batteries. A dedicated low cost battery management system is attached the battery pack as per Figure 8.7. Total weight of battery pack including BMS and case shown in Figure 8.8 sums up to 170 grams. Four units of these battery packs are connected in parallel. Along with 20A total output current capacity, reason for selecting four battery packs is to evenly distribute mass about yaw axis and keeping symmetry of design.

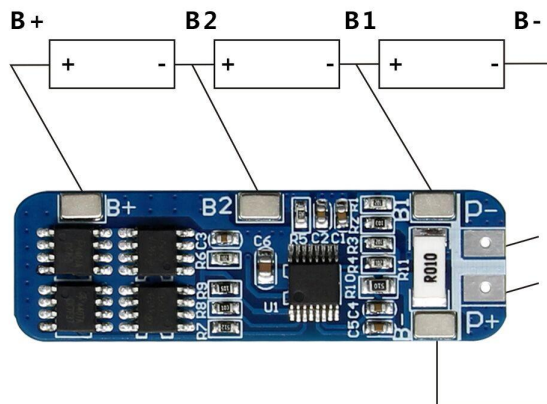


Figure 8.7. Schematic diagram of 11.1V 5A Battery Management System with 18650 Li-Ion batteries in series

3A DC to DC step down converter shown in Figure 8.9 is used to convert 11.1V

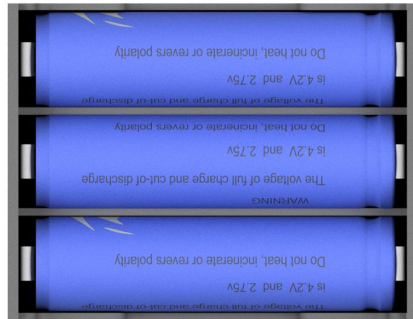


Figure 8.8. Rendered view of Case with three Li-Ion Batteries connected in series to make 3S Li-Ion battery pack

to 5V required by AS5400 and MCU. MP1584EN is a high frequency step-down switching regulator with an integrated internal high-side high voltage power MOSFET. Complete Electrical Power System schematic of VSCMG shown in Figure 8.10 contains 4 battery packs connected in parallel has 11.1V output supplied to all the SGCMG units. 5V required by MCU, sensors and motor drivers is provided through two MP1584EN step down converters. This type of modular design simplified the build process since only one unit is to be made and tested and it is easy to replicate same systems with reduced cost. It also reduced debugging complexity since faulty unit can easily be separated and tested individually.

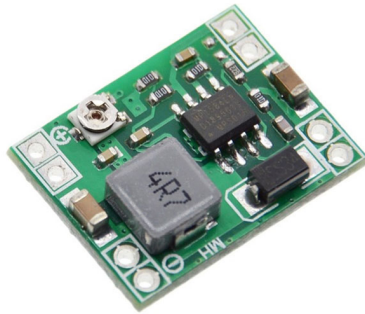


Figure 8.9. MP1584EN 3A DC to DC step down converter configured to convert 11.1V to 5.0V

8.4 Ground Control Station Server

Most important part of VSCMG ACS testbed is its novel ground control station server software. Prime functionalities of VSCMG command, control and telemetry

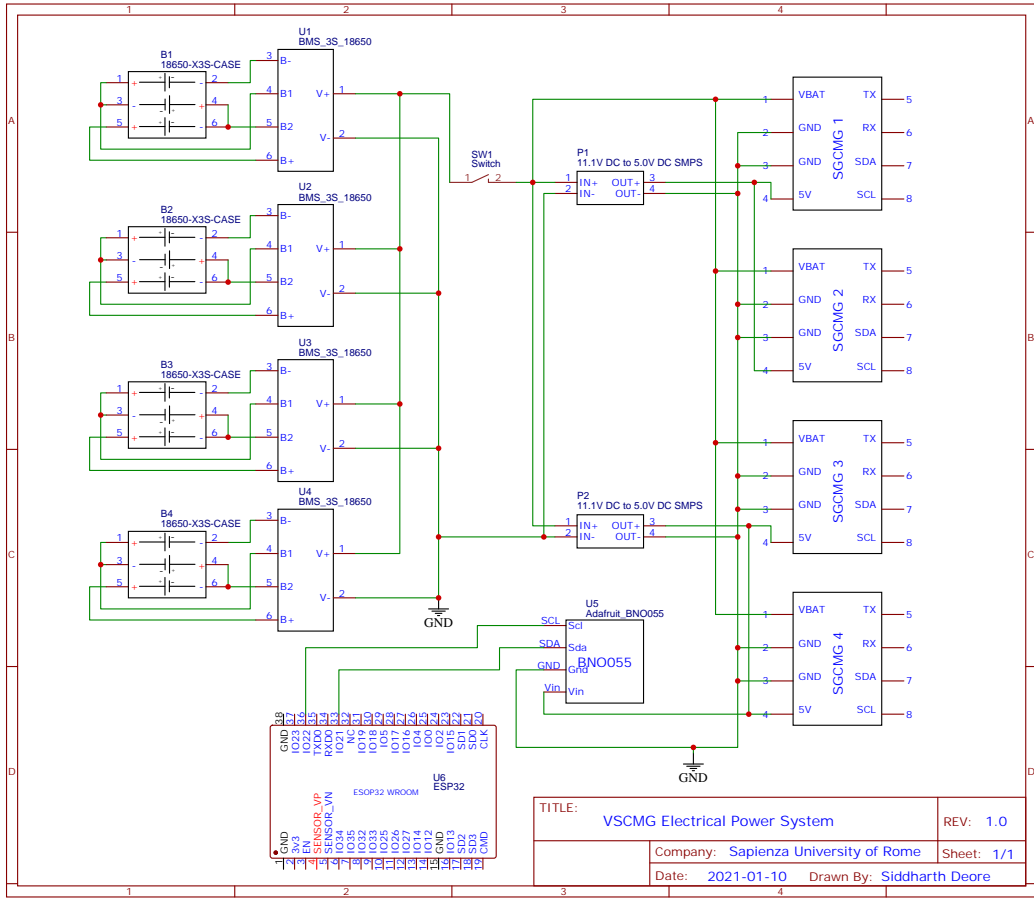


Figure 8.10. Wiring schematic of complete VSCMG test bed Electrical Power System

architecture are receive platform state such as body rate and attitude quaternions as well as state of each individual SGCMG unit which includes angular velocity of reaction wheel, gimbal angle and gimbal angular velocity. Afterwards, compute the signals to be provided to actuators based on selected control and steering algorithm and send command signal to each SGCMG unit simultaneously display all the state variables with 3D visualization of entire system.

8.4.1 Communication

Since each SGCMG unit and master platform has its own WiFi enabled MCU, all the communication requirements are solved using standard network protocol in particular User Datagram Protocol (UDP) due to simplicity of implementation and fast communication speed with least latency. Ground station server listens on port 3333 over UDP protocol. Each MCU on board as soon as powered on connected to same network SSID of server start transmitting their respective states packaged in specific format to server on same port 3333. As soon as server receives the states from all MCUs it updates all the state variables on GUI simultaneously replies with the command signals for particular MCU. Server communication loop is running

at 1000Hz and can easily increased which is far beyond actuator and sensor loop time requirements for this reason even though control and steering law is ported on server computer high speed communication simulates as if control is happening inside on board computer. In this thesis a custom messaging protocol designed on the top of UDP is developed. String of bytes transmitted or received on UDP buffer. There are three different types of message packets. A telemetry payload described in Table 8.1 is 7 byte packet transmitted from SGCMG to server it contains unique 8bit address of MCU, gimbal angle and reaction wheel angular velocity represented in two bytes each. Last two bytes are Cyclic Redundancy Check (CRC) computed with buffer starting from byte 0 to byte 4.

byte	Mnemonic	Description
0	ADDR	Address of MCU
1	GMB_H	Gimbal Angle high byte
2	GMB_L	Gimbal Angle low byte
3	OMG_H	Reaction wheel angular velocity
4	OMG_L	Reaction wheel angular velocity
5	CRC_H	CRC hight byte
6	CRC_L	CRC low byte

Table 8.1. Telemetry packet from SGCMG to Server

An example of SGCMG 1 hexadecimal byte string packet with address gimbal angle 60 deg and reaction wheel angular velocity 50 deg/sec is as follows:

[0x50 0xAA 0xAA 0xBF 0xFF 0x84 0xD5]

here 0x50 is address of MCU, next two bytes 0xAA 0xAA represent gimbal angle and 0xBF 0xFF represent angular velocity of reaction wheel finally last two bytes are computed CRC16 checksum. Gimbal angle -180.0 deg to 180.0 deg is represented in two bytes as per following conversion factor:

$$(\text{word})\text{Angle} = (\text{angle} + 180) \frac{65536}{360} \quad (8.1)$$

Angular velocity range -100.0 deg / sec to 100.0 deg / sec is represented in two bytes as per following conversion factor:

$$(\text{word})\text{Velocity} = (\text{velocity} + 100) \frac{65536}{200} \quad (8.2)$$

Element of quaternion vector ranging from -1.0 to 1.0 is represented in two bytes as per following conversion factor:

$$(\text{word})\text{Quaternion} = (\text{quaternion}_i + 1)32768 \quad (8.3)$$

Decomposition of 2 byte = 1 word (16bit) in to chunks of 8bits is represented as high and low byte as given in Table 8.2

Command packet transmitted to SGCMG shown in Table 8.3 contains address of destination MCU, 2 byte data of magnetic encoder offset correction, command

bit	15	14	13	12	11	10	9	8	7	6	5	4	3	2	1	0
	High Byte								Low Byte							

Table 8.2. Composition of Leftmost and rightmost byte of 16 bit word.

byte	Mnemonic	Description
0	ADDR	Address of MCU
1	OFFSET_H	Magnetic Encoder offset high byte
2	OFFSET_L	Magnetic Encoder offset low byte
3	CMD_GMB_H	Command Gimbal Angular velocity high byte
4	CMD_GMB_L	Command Gimbal Angular velocity low byte
5	CMD_OMG_H	Command RW Angular velocity high byte
6	CMD_OMG_L	Command RW Angular velocity low byte
7	CRC_H	CRC hight byte
8	CRC_L	CRC low byte

Table 8.3. Command packet from Server to SGCMG MCU

gimbal angular velocity, and command reaction wheel angular velocity ended with 2 bytes of CRC.

Similarly, 17 byte packet is transmitted from Master to server contains 8 bit address of master, quaternion vector, and body rate vector having two bytes for each element of vector and at last 2 bytes CRC computed with buffer from byte 0 to byte 14 as given in Table 8.4

This type of coding scheme allows fast data transmission without conflicting any variable, in addition since data is sent in string made up of chunks of 8 bit (byte), same coding scheme can be ported easily to various embedded communication protocols such as UART or I2C making it easy to port control algorithm on board master controller based on users choice. Note that CRC appended at the end of each message is 16 bit error detecting code following IBM CRC-16 also referred as CRC-16-ANSI X3.28 polynomial representations of cyclic redundancy check with polynomial $x^{16} + x^{15} + x^2 + 1$.

byte	Mnemonic	Description
0	ADDR	Address of MCU
1	Q0_H	Quaternion 0 high byte
2	Q0_L	Quaternion 0 low byte
3	Q1_H	Quaternion 1 high byte
4	Q1_L	Quaternion 1 low byte
5	Q2_H	Quaternion 2 high byte
6	Q2_L	Quaternion 2 low byte
7	Q3_H	Quaternion 3 high byte
8	Q3_L	Quaternion 4 low byte
9	omegaX_H	Body rate about x axis high byte
10	omegaX_L	Body rate about x axis low byte
11	omegaY_H	Body rate about y axis high byte
12	omegaY_L	Body rate about y axis low byte
13	omegaZ_H	Body rate about z axis high byte
14	omegaZ_L	Body rate about z axis low byte
15	CRC_H	CRC hight byte
16	CRC_L	CRC low byte

Table 8.4. Telemetry packet from Master MCU to Server

Ground station software responsible for entire control and steering of VSCMG testbed. Core functionalities of the server software is to receive telemetry packets from VSCMG test setup, decode byte stream in to appropriate state variable and transmit command signal in form of byte stream to corresponding actuators. A GUI shown in Figure 8.11 developed in python allows real-time visualization of state variables. Interactive GUI allows user to manually command gimbal angle and reaction wheel angular velocity and update magnetic encoder offsets. Moreover, various control schemes such as Singularity Robust VSCMG steering, Neural Network based steering can be switched as well as controller gains can be updated in real-time. In order to have visual representation of state variables a 3D view of VSCMG satellite implemented using OpenGL. Several steps has been taken to improve performance of software and make it stable. Extensive use of multi-threading includes four diffident threads, one thread dedicated for communication over UDP another thread is responsible for computation of control and steering based on selected algorithm, one thread for GUI and user interaction input and a thread for 3D visualization of Satellite. Although, entry point of software is written in python, all the core components and computationally expensive algorithms are written in C++ wrapped using Boost.Python [41] in order to expose these compiled libraries to python.

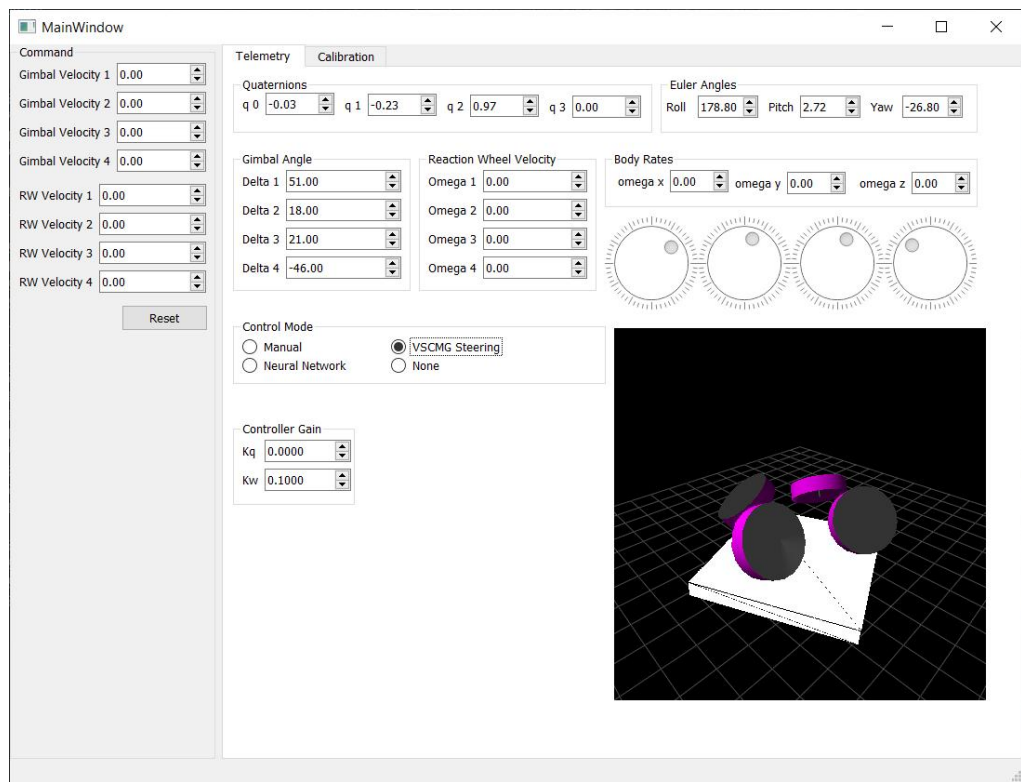


Figure 8.11. Ground command and control server Graphical User Interface

Chapter 9

Hardware in Loop Simulations

Real time simulations of VSCMG testbed are discussed in this chapter. Various investigations are performed on prototype in order to verify control law and tweak the model dynamics, since exact dynamics of commercial off the shelf affordable components used to build the prototype were unknown. However after several experimental tests so that system works properly as per requirements. Test data is recorded in real time and results are exported to Matlab for post processing.

9.1 Free Motion (ACS off)

Platform kept placed on custom made tripod is balancing on sharp tip, this imitates free attitude motion. A theoretical point contact has three degree of freedom in attitude and constrained in translation motion. If point of contact coincides with the center of mass of platform a free attitude simulation can be achieved. Although practically achieving zero friction motion is impossible with this method due to geometrical constraints and difficulty of mass balancing. Considering these problems center of mass is kept below point of contact thus platform imitates as physical pendulum. Behaviour of test-setup with initial disturbance and no active control system is shown in Figure 9.1 and Figure 9.2. Platform is subjected to two conservative disturbances, first near 5 sec and damps after 40 sec. And after second disturbance, amplitude of angular velocity peaks keeps decreasing and completely fade away after 50 seconds mainly due to friction in sharp tip and stand.

9.2 Open Loop Control

In order to test the command response of actuator and weather they are capable of overcoming the friction and are able to move platform is few open loop tests are conducted.

9.2.1 Open Loop CMG

As provision for producing gyroscopic torque, initially all the reaction wheels are accelerated to 3000 RPM with platform at rest and equal angular momentum of all RWs. All gimbal motors are commanded to rotate at 1 RPM angular velocity in

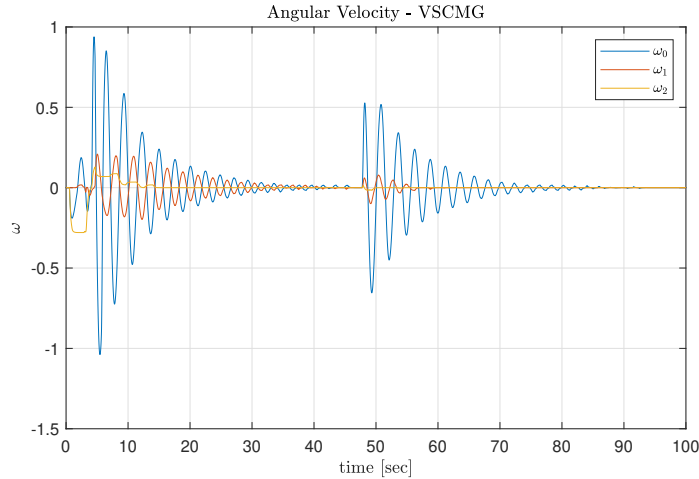


Figure 9.1. ACS off free motion of test bed upon disturbance

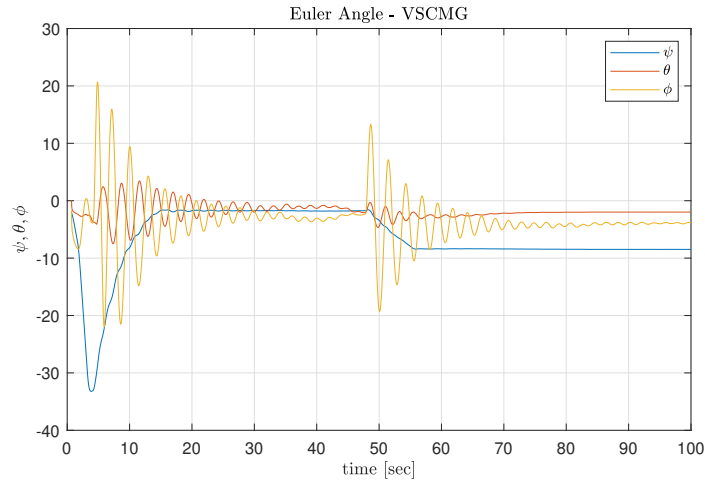
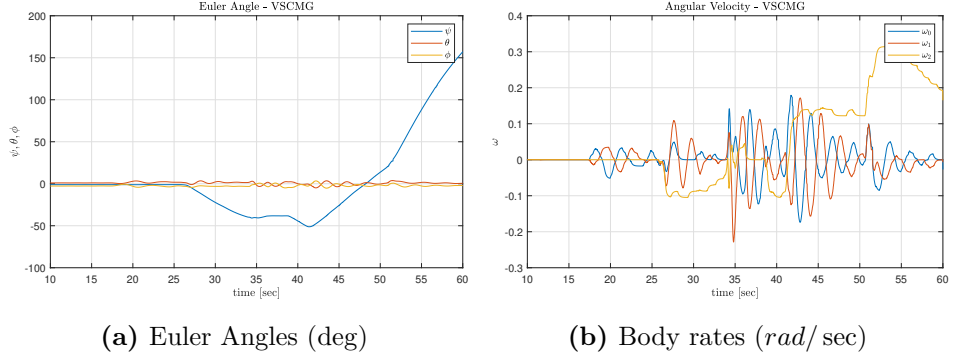


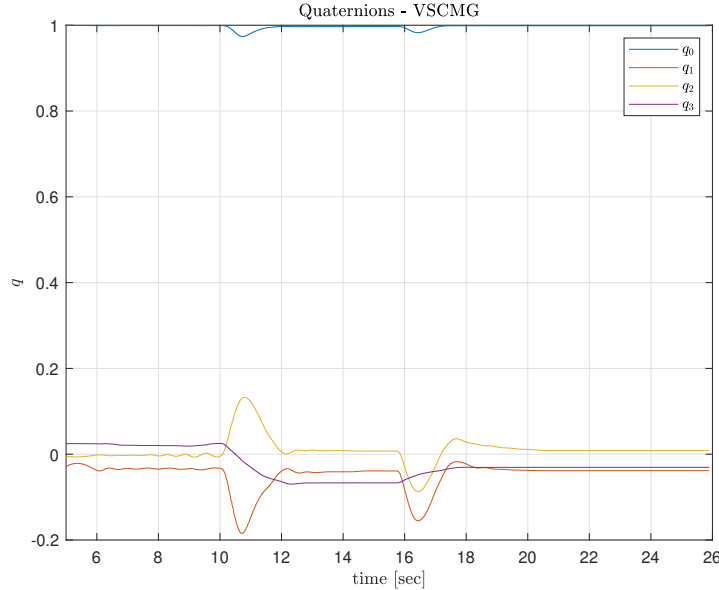
Figure 9.2. Free response of platform subjected to disturbance, Euler angles (deg)

order to produce torque along yaw axis. Initially at rest, platform starts accelerating around yaw axis. As soon as gimbal angle crosses 180 degrees, net torque direction is reversed and platform starts de-accelerating first and later starts rotating in opposite direction. From Figure 9.3a it is clear that maximum variation in attitude only around yaw axis and no significant change in roll and pitch is visible. In Figure 9.3b, angular velocity along roll and pitch axis is oscillating with maximum amplitude of 0.2 rad/sec. Direction of angular velocity about yaw axis (ω_2) does not change as rapidly as compared to roll and pitch axis, consequently making large deviation about yaw.

**Figure 9.3.** Open loop maneuver results of CMG

9.3 Close Loop SR-VSCMG Control

In this section results of VSCMG based steering law are presented considering only derivative feedback. Quaternion feedback gain K_q is set to zero and angular velocity feedback gain $K_w = 0.6$ is selected after several iteration and testing. Initially platform is kept at res. All reaction wheels kept at zero RPM thus it is clear that CMG can not produce required torque. Close loop controller is turned on at 8 seconds and platform is manually disturbed by hand. From Figure 9.5 two disturbance events can be clearly seen at 10 seconds and 15 seconds. For first disturbance, platform is tilted by hand. From first peak it is clear that only platform resist the tilt motion and angular velocities are damped within 3 seconds. Second disturbance seen at 15 seconds is small nudge to platform was compensated within 2 seconds with no steady state error beyond 5 seconds after disturbance event. Only reaction wheel based

**Figure 9.4.** Close loop maneuver using VSCMG steering law with only derivative feedback
- Platform quaternions

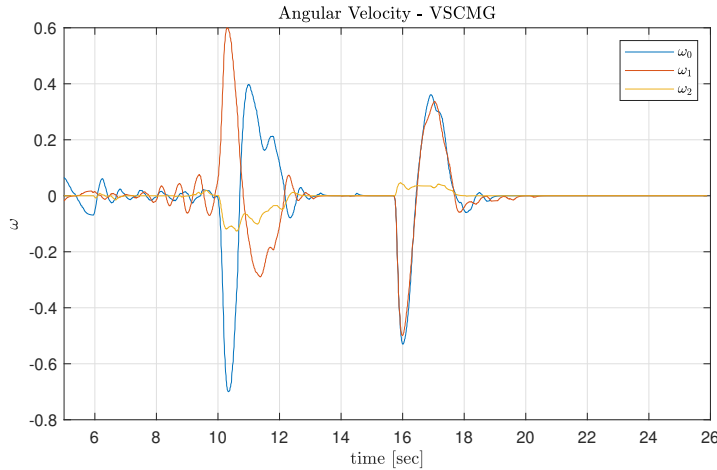


Figure 9.5. Close loop maneuver using VSCMG steering law with only derivative feedback
- Platform angular velocities (rad/ sec)

controller was sufficient to counteract the external disturbances. Euler angles shown in Figure 9.6 are computed from quaternions. It is clear that although platform was balanced to maintained at the level, offset in roll and pitch are visible because of uncertainty in placement of IMU which is at offset from platform which introduce orientation error. Despite these uncertainties due to placement of IMU, controller is able to counteract the disturbance and quickly bring platform to steady state.

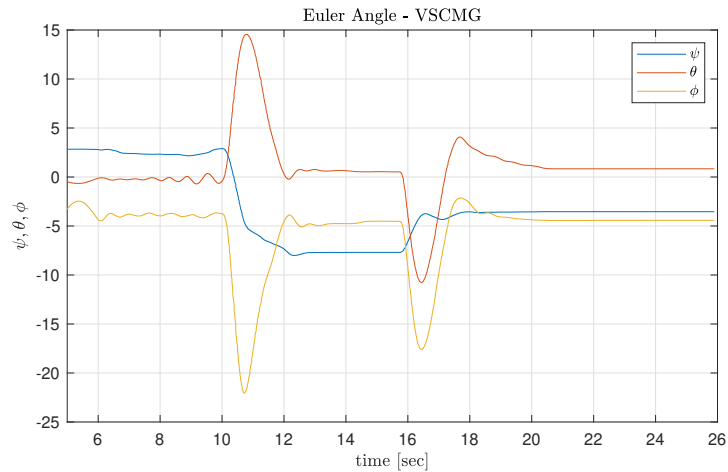


Figure 9.6. Close loop maneuver using VSCMG steering law with only derivative feedback
- Euler angles (deg)

After several iterations of testing, many problems were analyzed of which most important is very small oscillations persist which were not visible in each test with same input parameters. Controller has different steady state performance for and long time is needed to compensate disturbances, this was due to lower battery voltage and can be solved by keeping batteries above minimum threshold or by updating controller gain based on available power. Orientation uncertainties can be removed

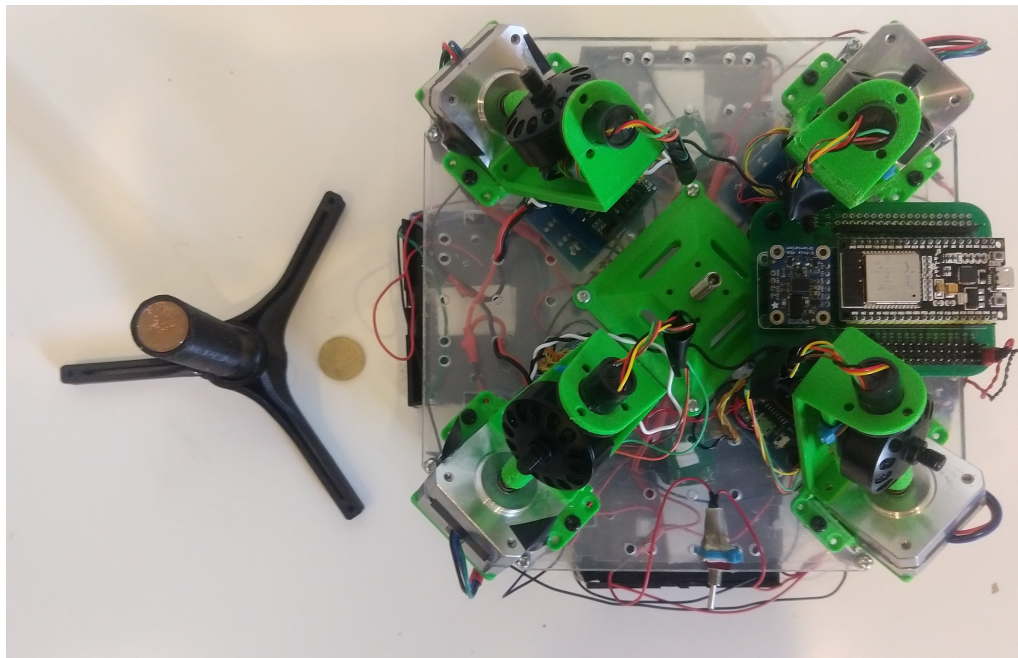


Figure 9.7. Top view of custom-built VSCMG experimental test bed and tripod

by recording IMU offset and introducing offset rotation matrix. Gimbal angle is measured through magnetic encoder which provide absolute angular feedback but are not linear due to offset in sensor and shaft magnet. Since steeper motors are used for gimbal, Encoder error can be compensated by keeping track of motor steps and updating the zero position every time magnet crosses the zero position. Thus magnetic encoders will be only used as reference. Breathless motors used for reaction wheels are driven using back EMF feed back based motor controller. These type of controllers are not capable of running motors at lower speed and significant dead band is present near zero RPM, this is introduces jerks at lower speeds. Hall sensor based controllers can be used to have better control at lower speed. Hall sensor based controllers keeps track of rotor orientation and activate coils in sequence based on pre determined lookup table.

Photos of custom-built test setup for VSCMG is shown in Figure 9.7 to Figure 9.9. Small 3D printed tripod with a metal coin at the top along side complete VSCMG platform is shown in Figure 9.7. Figure 9.8 and Figure 9.9 are top and side view of complete test setup.

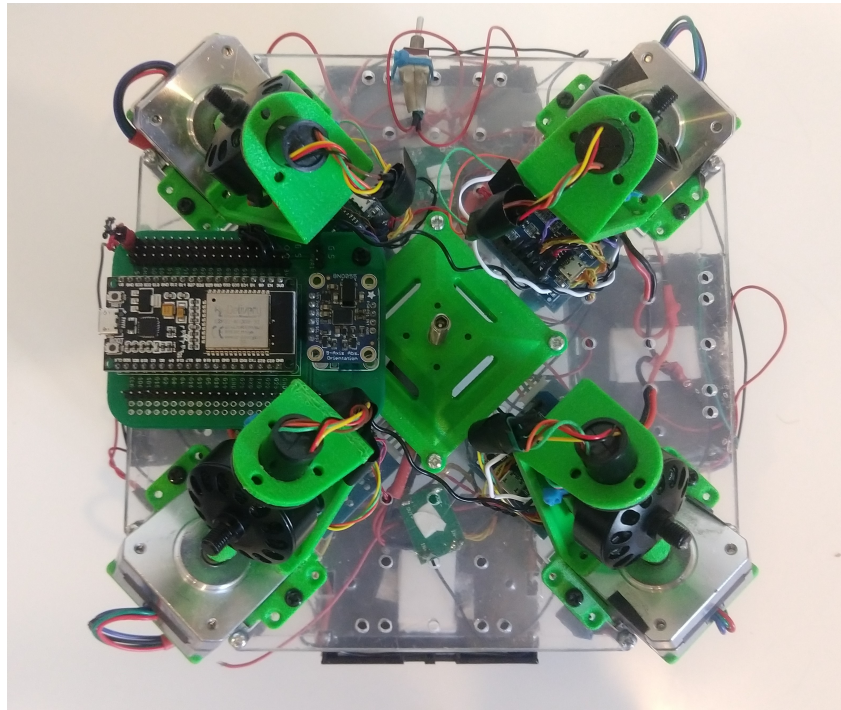


Figure 9.8. Top view of custom-built VSCMG experimental test bed balancing on tripod

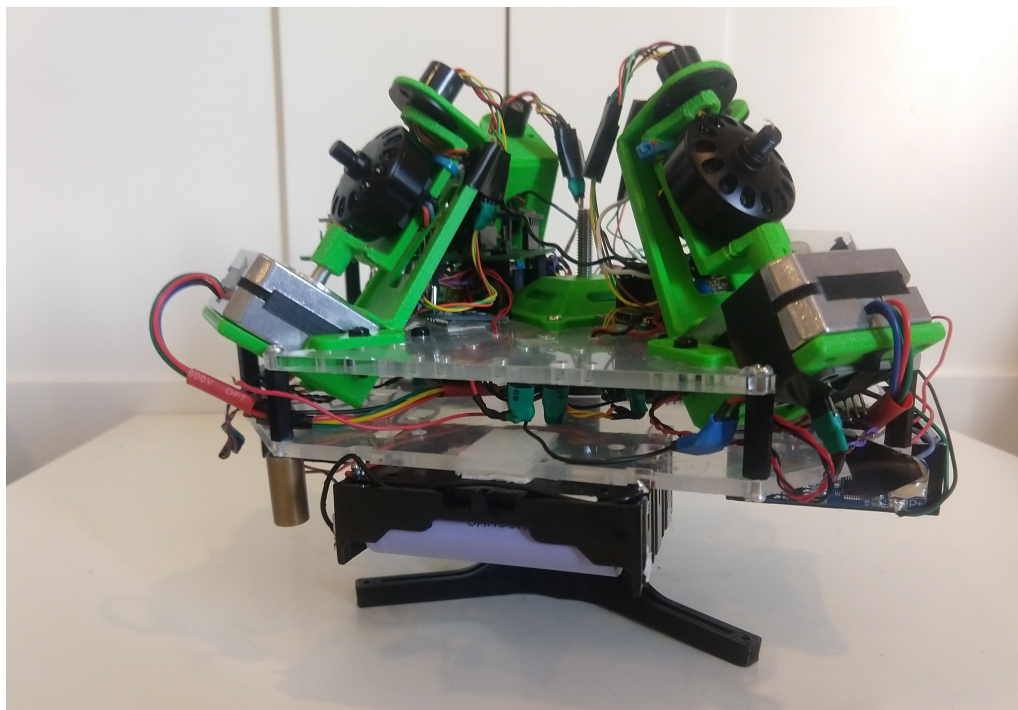


Figure 9.9. Side view of custom-built VSCMG experimental test bed balancing on tripod

Chapter 10

Conclusion

This thesis is aimed to realize Neural Network (NN)-based steering and Hardware in Loop simulation of Variable Speed Control Moment Gyroscope. Equation of motion is derived for spacecraft with generic number of VSCMG. Quaternion feedback-based controller and Singularity Robust (SR-VSCMG) steering is revived.

Ground based verification of attitude control algorithm is difficult due to complexity to imitate dynamics of spacecraft in free falling orbit. An affordable VSCMG platform test bench is developed to perform preliminary testing and hardware in loop simulation of spacecraft with VSCMG. In-house developed platform can simulate various configurations such as MW based, or CMG based control. Furthermore, developed ground control software is capable real-time visualization of state variables. Interactive GUI allows manually providing actuator commands or can select various control schemes such as neural network-based steering or SR-VSCMG steering with ability to update controller gains and other parameters in real-time allowing Hardware in Loop simulation of VSCMG.

A neural network based steering technique is developed by combining supervised learning with reference trajectories generated by Monte-Carlo simulation of Singularity Robust VSCMG steering law. Reinforcement Learning technique is used to further train the neural network in which based on current state controller explore the environment by taking actions for reward, goal is to maximize the delayed reward. Proposed steering algorithm is compared with SR-VSCMG steering via numerical simulations. NN based steering is inversion free technique and does not require to calculate inverse of matrix, hence very large velocities are not present in proximity of singularity i.e., when determinant of matrix is close to zero and also free from high velocity jitters in gimbal angle which are clearly visible in SR-VSCMG steering. Absence of such high frequency dynamics is advantageous for preserving mechanical integrity of spacecraft. Moreover, proposed technique performed faster and showed clear advantage in terms of computation time. It is observed that NN based agent always converges to desired states but may follow trajectories which may not be similar to SR-VSCMG law. NN performance can be improved by more training and selecting better reward function crafted for required performance. A Hybrid of both steering laws can be used, Neural Network based steering for large slew maneuvers when error is large and SR-VSCMG based steering when current state is in proximity of desired state.

Bibliography

- [1] R. S. Sutton and A. G. Barto, *Reinforcement learning: An introduction*. MIT press, 2018.
- [2] J. Schulman, F. Wolski, P. Dhariwal, A. Radford, and O. Klimov, “Proximal policy optimization algorithms,” 2017.
- [3] H.-K. Lim, J.-B. Kim, J.-S. Heo, and Y.-H. Han, “Federated reinforcement learning for training control policies on multiple iot devices,” *Sensors*, vol. 20, p. 1359, 03 2020.
- [4] “OMC Stepper nema17 stepper motor datasheet.” <https://web.archive.org/web/20200929174331/https://www.omc-stepperonline.com/download/17HS08-1004S-.pdf>. Accessed: 2020-09-29.
- [5] F. Santoni and F. Graziani, “Guidance of small launchers using neural networks,” *Space Technology*, vol. 16, no. 5-6, pp. 303–306, 1996.
- [6] D. Silver, A. Huang, C. J. Maddison, A. Guez, L. Sifre, G. van den Driessche, J. Schrittwieser, I. Antonoglou, V. Panneershelvam, M. Lanctot, S. Dieleman, D. Grewe, J. Nham, N. Kalchbrenner, I. Sutskever, T. Lillicrap, M. Leach, K. Kavukcuoglu, T. Graepel, and D. Hassabis, “Mastering the game of Go with deep neural networks and tree search,” *Nature*, vol. 529, no. 7587, pp. 484–489, 2016.
- [7] “SpaceX dragon sending humans and cargo into space.” <https://web.archive.org/web/20201023154402/https://www.spacex.com/vehicles/dragon/>. Accessed: 2020-10-29.
- [8] E. Seedhouse, *SpaceX’s Dragon: America’s Next Generation Spacecraft*. Springer Praxis Books, Springer International Publishing, 1 ed., 2016.
- [9] P. Tsiotras, H. Shen, and C. Hall, “Satellite attitude control and power tracking with energy/momentum wheels,” *Journal of Guidance, Control, and Dynamics*, vol. 24, no. 1, pp. 23–34, 2001.
- [10] F. A. Leve, B. J. Hamilton, and M. A. Peck, *Spacecraft momentum control systems*. 2015.
- [11] F. L. Markley and J. L. Crassidis, *Fundamentals of spacecraft attitude determination and control*. 2014.

- [12] E. Scott, "CONTROL MOMENT GYRO GRAVITY STABILIZATION," in *Guidance and Control*, 1964.
- [13] D. J. Liska, "A two-degree-of-freedom control moment gyro for high-accuracy attitude control," *Journal of Spacecraft and Rockets*, 1968.
- [14] SELTZER SM and CHUBB WB, "Skylab attitude and pointing control system,"
- [15] T. R. Coon and J. E. Irby, "SKYLAB ATTITUDE CONTROL SYSTEM.," *IBM Journal of Research and Development*, 1976.
- [16] V. N. Branets, D. M. Weinberg, V. P. Verestchagin, N. N. Danilov-Nitusov, V. P. Legostayev, V. N. Platonov, Y. P. Semyonov, V. S. Semyachkin, B. E. Chertock, and N. N. Sheremetevsky, "Development experience of the attitude control system using single-axis control moment gyros for long-term orbiting space stations," *Acta Astronautica*, 1988.
- [17] C. Gurrisi, R. Seidel, S. Dickerson, S. Didziulis, P. Frantz, and K. Ferguson, "Space Station Control Moment Gyroscope Lessons Learned," in *Aerospace Mechanisms Symposium*, 2010.
- [18] T. SASAKI and T. SHIMOMURA, "Gain-Scheduled Control/Steering Design for a Spacecraft with Variable-Speed Control Moment Gyros," *SICE Journal of Control, Measurement, and System Integration*, vol. 10, no. 3, pp. 237–242, 2017.
- [19] X. Huang, Y. Jia, S. Xu, and T. Huang, "A new steering approach for VSCMGs with high precision," *Chinese Journal of Aeronautics*, vol. 29, no. 6, pp. 1673–1684, 2016.
- [20] H. Yoon and P. Tsiotras, "Spacecraft adaptive attitude and power tracking with variable speed control moment gyroscopes," *Journal of Guidance, Control, and Dynamics*, vol. 25, no. 6, pp. 1081–1090, 2002.
- [21] S. Krishnan and S. R. Vadali, "An inverse-free technique for attitude control of spacecraft using cmgs," *Acta Astronautica*, vol. 39, no. 6, pp. 431 – 438, 1996.
- [22] Q. Lam, B. Anderson, and M. Xin, "Preserving spacecraft attitude control accuracy using theta-d controller subject to reaction wheel failures," 04 2010.
- [23] A. MELDRUM, S. NONOMURA, K. YAMADA, and Y. SHOJI, "Attitude Control Using Three Control Moment Gyros," *Transactions of the Japan Society for Aeronautical and Space Sciences, Aerospace Technology Japan*, vol. 16, no. 5, pp. 405–411, 2018.
- [24] OpenAI, :, C. Berner, G. Brockman, B. Chan, V. Cheung, P. Dębiak, C. Dennison, D. Farhi, Q. Fischer, S. Hashme, C. Hesse, R. Józefowicz, S. Gray, C. Olsson, J. Pachocki, M. Petrov, H. P. de Oliveira Pinto, J. Raiman, T. Salimans, J. Schlatter, J. Schneider, S. Sidor, I. Sutskever, J. Tang, F. Wolski, and S. Zhang, "Dota 2 with large scale deep reinforcement learning," 2019.

- [25] OpenAI, I. Akkaya, M. Andrychowicz, M. Chociej, M. Litwin, B. McGrew, A. Petron, A. Paino, M. Plappert, G. Powell, R. Ribas, J. Schneider, N. Tezak, J. Tworek, P. Welinder, L. Weng, Q. Yuan, W. Zaremba, and L. Zhang, “Solving rubik’s cube with a robot hand,” 2019.
- [26] G. P. Candinia, F. Piergentilib, and F. Santoni, “Miniaturized attitude control system for nanosatellites,” 2012.
- [27] H. Gui, L. Jin, S. Xu, and J. Zhang, “On the attitude stabilization of a rigid spacecraft using two skew control moment gyros,” *Nonlinear Dynamics*, vol. 79, no. 3, pp. 2079–2097, 2015.
- [28] S. Prabhakaran Viswanathan, A. K. Sanyal, and M. Izadi, “Mechatronics Architecture of Smartphone-Based Spacecraft ADCS using VSCMG Actuators,” *arXiv e-prints*, p. arXiv:1509.03677, Sept. 2015.
- [29] L. Arena, F. Piergentili, and F. Santoni, “Design, manufacturing, and ground testing of a control-moment gyro for agile microsatellites,” *Journal of Aerospace Engineering*, vol. 30, no. 5, p. 04017039, 2017.
- [30] B. Palais and R. Palais, “Euler’s fixed point theorem: The axis of a rotation,” *Journal of Fixed Point Theory and Applications*, vol. 2, pp. 215–220, 01 2007.
- [31] J. S. Ortega, “Quaternion kinematics for the error-state kf,” 2016.
- [32] H. Yoon and P. Tsiotras, “Singularity analysis of variable speed control moment gyros,” *Journal of Guidance Control and Dynamics - J GUID CONTROL DYNAM*, vol. 27, pp. 374–386, 05 2004.
- [33] K. A. Baker, “Control moment gyroscope skew angle variation and singularity penetration,” in *Advances in Spacecraft Attitude Control*, IntechOpen, Jan. 2020.
- [34] R. Reissig, “A. M. Liapunov, Stability of Motion. (Mathematics in Science and Engineering, Volume 30). XI + 203 S. New York/London 1966. Academic Press. Preis geb. \$ 9.75,” *Zeitschrift Angewandte Mathematik und Mechanik*, vol. 48, pp. 140–140, Jan. 1968.
- [35] B. Wie, H. Weiss, and A. Arapostathis, “Quaternion feedback regulator for spacecraft eigenaxis rotation,” *Journal of Guidance Control and Dynamics - J GUID CONTROL DYNAM*, vol. 12, pp. 375–380, 05 1989.
- [36] D. D. R. Williams, “Molniya 1-86 comsat description.” <https://web.archive.org/web/20201118021318/https://nssdc.gsfc.nasa.gov/nmc/spacecraft/display.action?id=1993-035A>, note = Accessed: 2020-11-18.
- [37] S. Russell, S. Russell, P. Norvig, and E. Davis, *Artificial Intelligence: A Modern Approach*. Prentice Hall series in artificial intelligence, Prentice Hall, 2010.

- [38] I. Grondman, L. Busoniu, G. Lopes, and R. Babuska, “A survey of actor-critic reinforcement learning: Standard and natural policy gradients,” *IEEE Transactions on Systems Man and Cybernetics Part B-Cybernetics*, vol. 42, pp. 1291–1307, 11 2012.
- [39] J. Schulman, S. Levine, P. Abbeel, M. Jordan, and P. Moritz, “Trust region policy optimization,” in *International conference on machine learning*, pp. 1889–1897, 2015.
- [40] G. Brockman, V. Cheung, L. Pettersson, J. Schneider, J. Schulman, J. Tang, and W. Zaremba, “Openai gym,” 2016.
- [41] D. Abrahams and R. W. Grosse-Kunstleve, “Building hybrid systems with boost. python,” *C/C++ Users Journal*, vol. 21, no. LBNL-53142, 2003.
- [42] M. Abadi, A. Agarwal, P. Barham, E. Brevdo, Z. Chen, C. Citro, G. S. Corrado, A. Davis, J. Dean, M. Devin, S. Ghemawat, I. Goodfellow, A. Harp, G. Irving, M. Isard, Y. Jia, R. Jozefowicz, L. Kaiser, M. Kudlur, J. Levenberg, D. Mané, R. Monga, S. Moore, D. Murray, C. Olah, M. Schuster, J. Shlens, B. Steiner, I. Sutskever, K. Talwar, P. Tucker, V. Vanhoucke, V. Vasudevan, F. Viégas, O. Vinyals, P. Warden, M. Wattenberg, M. Wicke, Y. Yu, and X. Zheng, “TensorFlow: Large-scale machine learning on heterogeneous systems,” 2015. Software available from tensorflow.org.
- [43] N. Bianchi, S. Bolognani, and F. Luise, “Analysis and design of a brushless motor for high speed operation,” pp. 44 – 51 vol.1, 07 2003.
- [44] “ESP32 technical referece manual.” https://web.archive.org/web/20210102203502/https://www.espressif.com/sites/default/files/documentation/esp32_technical_reference_manual_en.pdf. Accessed: 2020-09-29.
- [45] “BNO055 intelligent 9-axis absolute orientation sensor data sheet.” <https://web.archive.org/web/20201217104844/https://www.bosch-sensortec.com/media/boschsensortec/downloads/datasheets/bst-bno055-ds000.pdf>. Accessed: 2020-09-29.
- [46] S. Madgwick, “An efficient orientation filter for inertial and inertial/magnetic sensor arrays,” 2010.